



Government of **Western Australia**
Department of **Mines, Industry Regulation and Safety**

RECORD 2017/10

ALTERATION ASSOCIATED WITH THE AUSTIN–QUINNS VMS PROSPECTS, NORTHERN YILGARN CRATON

by
LY Hassan



Geological Survey of
Western Australia



Government of **Western Australia**
Department of **Mines, Industry Regulation and Safety**

Record 2017/10

ALTERATION ASSOCIATED WITH THE AUSTIN–QUINNS VMS PROSPECTS, NORTHERN YILGARN CRATON

by
LY Hassan

Perth 2017



**Geological Survey of
Western Australia**

MINISTER FOR MINES AND PETROLEUM
Hon Bill Johnston MLA

ACTING DIRECTOR GENERAL, DEPARTMENT OF MINES, INDUSTRY REGULATION AND SAFETY
David Smith

EXECUTIVE DIRECTOR, GEOLOGICAL SURVEY OF WESTERN AUSTRALIA
Rick Rogerson

REFERENCE

The recommended reference for this publication is:

Hassan, LY 2017, Alteration associated with the Austin–Quinns VMS prospects, northern Yilgarn Craton: Geological Survey of Western Australia, Record 2017/10, 61p.

National Library of Australia Card Number and ISBN 978-1-74168-768-2

Grid references in this publication refer to the Geocentric Datum of Australia 1994 (GDA94). Locations mentioned in the text are referenced using Map Grid Australia (MGA) coordinates, Zone 50. All locations are quoted to at least the nearest 100 m.

Disclaimer

This product was produced using information from various sources. The Department of Mines, Industry Regulation and Safety (DMIRS) and the State cannot guarantee the accuracy, currency or completeness of the information. DMIRS and the State accept no responsibility and disclaim all liability for any loss, damage or costs incurred as a result of any use of or reliance whether wholly or in part upon the information provided in this publication or incorporated into it by reference.

Published 2017 by Geological Survey of Western Australia

This Record is published in digital format (PDF) and is available online at <www.dmp.wa.gov.au/GSWApublications>.

Further details of geological products and maps produced by the Geological Survey of Western Australia are available from:

Information Centre
Department of Mines, Industry Regulation and Safety
100 Plain Street
EAST PERTH WESTERN AUSTRALIA 6004
Telephone: +61 8 9222 3459 Facsimile: +61 8 9222 3444
www.dmp.wa.gov.au/GSWApublications

Cover image: Elongate salt lake on the Yilgarn Craton — part of the Moore–Monger paleovalley — here viewed from the top of Wownaminy Hill, 20 km southeast of Yalgoo, Murchison Goldfields. Photograph taken by I Zibra for the Geological Survey of Western Australia

Contents

Abstract	1
Introduction	1
Geologic setting	4
Method	4
Prospect lithology, mineralization and alteration	7
Austin	7
Lithologies intersected	12
Mineralization	14
Alteration	17
Robert Prospect	26
Lithologies intersected	26
Mineralization	26
Alteration	26
Herbert Prospect	28
Lithologies intersected	28
Mineralization	29
Alteration	29
Franklin	30
Lithologies intersected	30
Alteration and metamorphic minerals	36
Dicksons (Silver Swan) Prospect	42
Lithologies intersected	42
Mineralization	42
Alteration	42
Tasman Prospect	44
Lithologies intersected	46
Mineralization	51
Alteration	51
Discussion	52
Genesis of the alteration assemblages	52
Environment of formation	59
Exploration vectors	59
Conclusions	59
Acknowledgements	60
References	60

Appendices

1. Lithological logs
2. TIR and SWIR allowed minerals

NOTE: The accompanying zip file contains the appendices.

Figures

1. Simplified geological map of the northern Youanmi Terrane showing location of Austin and Quinns and other VMS deposits and prospects	2
2. Geological map of the Austin–Quinns area showing locations of VMS prospects and studied drillholes	3
3. Different interpretations of the geology in the Quinns area	5
4. Interpretations of structure at Austin	6
5. HyLogger, lithology and assay data for drillhole 09ATD019 from Austin	8
6. HyLogger, lithology and assay data for drillhole 09ATD015 from Austin	9
7. HyLogger, lithology and assay data for drillhole 09ATD025 from Austin	10
8. HyLogger, lithology and assay data for drillhole ATD101 from Austin	11
9. Felsic rocks from the Austin drillholes	13
10. BIF from Austin	14
11. Fine-grained mafic rocks from Austin	15
12. Lower zinc-rich horizon at Austin	16

13.	Mineralization at depth at Austin	16
14.	Copper-rich mineralization at Austin	17
15.	Sulfides from breccia	18
16.	Alteration minerals at Austin	21
17.	Distal alteration at Austin	23
18.	Phosphate minerals at Austin	24
19.	Epidote minerals at Austin	24
20.	HyLogger, lithology and assay data for drillhole 09RTD001 from the Robert Prospect	27
21.	Lithic tuff at Robert Prospect	28
22.	Exhalite at Robert Prospect	29
23.	Xenolith of felsic rock in dolerite at the Robert Prospect	30
24.	HyLogger, lithology and assay data for drillhole 09HBRCD001 from the Herbert Prospect	31
25.	Felsic rocks from the Herbert Prospect	32
26.	Basalt from the Herbert Prospect	33
27.	BIF from the Herbert Prospect	33
28.	Sphalerite and chalcopyrite in BIF from the Herbert Prospect	33
29.	HyLogger, lithology and assay data for drillhole 09FKRCD001 from the Franklin Prospect	34
30.	Alteration minerals at the Franklin Prospect	35
31.	Chlorite schist with fine-grained ilmenite from the Franklin Prospect	36
32.	Remnant pyroxene in altered gabbro from the Franklin Prospect	36
33.	Dolerite from the Franklin Prospect	36
34.	Muscovite and paragonitic aluminoceladonite at the Franklin Prospect	37
35.	Phase x at the Franklin Prospect	39
36.	Xenotime replacing zircon along fractures at the Franklin Prospect	41
37.	Magnesiocarpholite at the Franklin Prospect	41
38.	HyLogger, lithology and assay data for drillhole 09DKRCD001 from Silver Swan Group's Dicksons Prospect	43
39.	Rhyolite from Silver Swan Group's Dicksons Prospect	44
40.	Felsic breccia from Silver Swan Group's Dicksons Prospect	45
41.	Schist intercalated with rhyolite and volcanic breccia from Silver Swan Group's Dicksons Prospect	46
42.	Basalt from Silver Swan Group's Dicksons Prospect	46
43.	Quartz vein with alteration halo of amphibole and epidote in rhyolite from Silver Swan Group's Dicksons Prospect	47
44.	White mica replacing Phase x	47
45.	HyLogger, lithology and assay data for drillhole 10TJD001 from the Tasman Prospect	48
46.	Tuff, metasedimentary rocks and schist of uncertain protolith from the Tasman Prospect	49
47.	BIF from the Tasman Prospect	50
48.	Mafic rocks at the Tasman Prospect	52
49.	Mineralization from the Tasman Prospect	53
50.	Garnet partially replaced by chlorite	54
51.	Maximum vent temperatures of modern seafloor hydrothermal systems in different volcanic and tectonic settings	56
52.	Sulfide-rich breccia zone that may have been pathway for hydrothermal fluids	56
53.	Zonation of hydrothermal alteration minerals in the Quinns area	57

Tables

1.	Drillhole locations	4
2.	Significant intersections in studied diamond drillholes from Austin	15
3.	Talc SEM analyses	see zip file
4.	Anthophyllite SEM analyses	see zip file
5.	Cummingtonite SEM and electron microprobe analyses	19
6.	SEM analyses of calcium amphiboles from Austin	22
7.	SEM analyses of chlorite from Austin	see zip file
8.	SEM analyses of white mica from Austin	see zip file
9.	SEM analyses of phosphates from Austin	25
10.	SEM analyses of epidote group minerals from Austin	26
11.	Franklin chlorite SEM analyses	37
12.	Franklin white mica SEM analyses	38
13.	Franklin gedrite SEM analyses	39
14.	Phase x SEM analyses	40
15.	Phase x electron microprobe analyses	40
16.	Franklin aluminium silicate SEM analyses	41
17.	?Magnesiocarpholite SEM analyses	42
18.	SEM analysis of garnet from the Tasman Prospect	54
19.	Summary of alteration minerals and relative timing at the different prospects in the Austin–Quinns area	58

NOTE: The accompanying zip file contains all tables and most tables are included in the text unless specified.

Alteration associated with the Austin–Quinns VMS prospects, northern Yilgarn Craton

by

LY Hassan

Abstract

Zinc and copper-rich volcanogenic massive sulfide (VMS) mineralization at Austin is characterized by the presence of abundant talc alteration which is interpreted to have formed on the seafloor by hydrothermal venting and in the sub-seafloor by the passage of hot fluids. The local presence of anthophyllite and cummingtonite is interpreted to be the result of metasomatism by hot fluids rather than regional metamorphism as the widespread occurrence of chlorite suggests that the rocks were only metamorphosed to greenschist facies. Chlorite and white mica are the main alteration minerals distal to mineralization at Austin. At Quinns, iron-rich chlorite and subordinate talc occur proximal to mineralization. The chlorite–talc alteration zone is surrounded by schist with aluminium silicate \pm garnet alteration. Chlorite and white mica are the main alteration minerals distal to mineralization at Quinns as at Austin. Early alteration assemblages are locally overprinted by later hydrothermal alteration characterized by development of Ca-amphiboles and epidote. Quartz veins and lodes with gold mineralization are also related to late hydrothermal alteration at Quinns.

This study concludes that the VMS mineralization and associated alteration formed during periods of volcanic quiescence within a very deep brine pool in a rifted arc environment. The hydrothermal system was driven by heat from underlying magma, and rifting and fluid flow continued over a prolonged period.

KEYWORDS: alteration (geology), andalusite, anthophyllite, banded iron formation, basalt, copper, cummingtonite, gabbro, gold, intrusive rocks, kyanite, massive sulphide deposits, metasomatism, rhyolite, sillimanite, talc, tellurium minerals, volcanic hosted deposits, zinc

Introduction

The Austin–Quinns volcanogenic massive sulfide (VMS) project forms part of a larger study by the Geological Survey of Western Australia (GSWA) on VMS deposits in the Murchison region and southwest of Western Australia. The aim of the project is to build genetic models for the environments of ore formation, and provide useful vectors for exploring in greenfields areas.

The Austin–Quinns project area is located 55 km south-southeast of Meekatharra in the northern Youanmi Terrane (Fig. 1). Gold was discovered in an ironstone reef at Quinns in 1891 by W Topping. The first lease was known as the Rise and Shine (incorrectly recorded as the Rising Shine in the register of GML 20/14) but the ground was later incorporated in the Lady Quinn lease (GML 51/462). Several other auriferous ironstone reefs and quartz reefs, as well as alluvial gold, were discovered shortly afterwards (Feldtmann, 1921). Recorded gold production from the Quinns mining centre between 1897 and 1988 was 646.77 kg (Department of Mines and Petroleum, Royalties Production cards; yearly production by centre); pre-1897 production figures are not available.

Feldtmann (1921) noted the presence of copper minerals including chalcopyrite, tetrahedrite and chrysocolla in quartz on the dump of a shaft on the Two Jacks Reef near the boundary between the Phoenix and Phoenix Extended leases. In 1975, Newmont discovered massive sulfide gossans (Newmont Pty Ltd, 1977), interpreted to be oxidized exhalites associated with VMS mineralization. These gossans were named Quinns, T and J (also referred to as T&J) and named after the historic Two Jacks gold mine), Dicksons, Murchison Wonder, Nowthanna and Chert Gossan. During 1976 and 1977, Newmont mapped, sampled and drilled these gossans. Newmont obtained the best base metal intersections of 1.3 m at 14.5% Zn and 2 m at 1.85% Cu in diamond drillhole QMV1, 6.0 m at 3.8% Zn in diamond drillhole QMV6 at Murchison Wonder, and 0.64 m at 1.95% Cu and 0.86% Zn at the T and J Gossan. Newmont also intersected 0.57 m at 1.1% Mo in diamond drillhole QMV6 at Murchison Wonder (Newmont Pty Ltd, 1977, 1978). Aberfoyle Exploration Pty Ltd, Esso Exploration and Production Ltd and CRA Exploration Pty Ltd subsequently explored for base metals in the gossans. Aberfoyle Exploration Pty Ltd intersected 8 m at 2.43% Zn at Dicksons (1980 report by EH Skey for Aberfoyle Exploration Pty Ltd, quoted

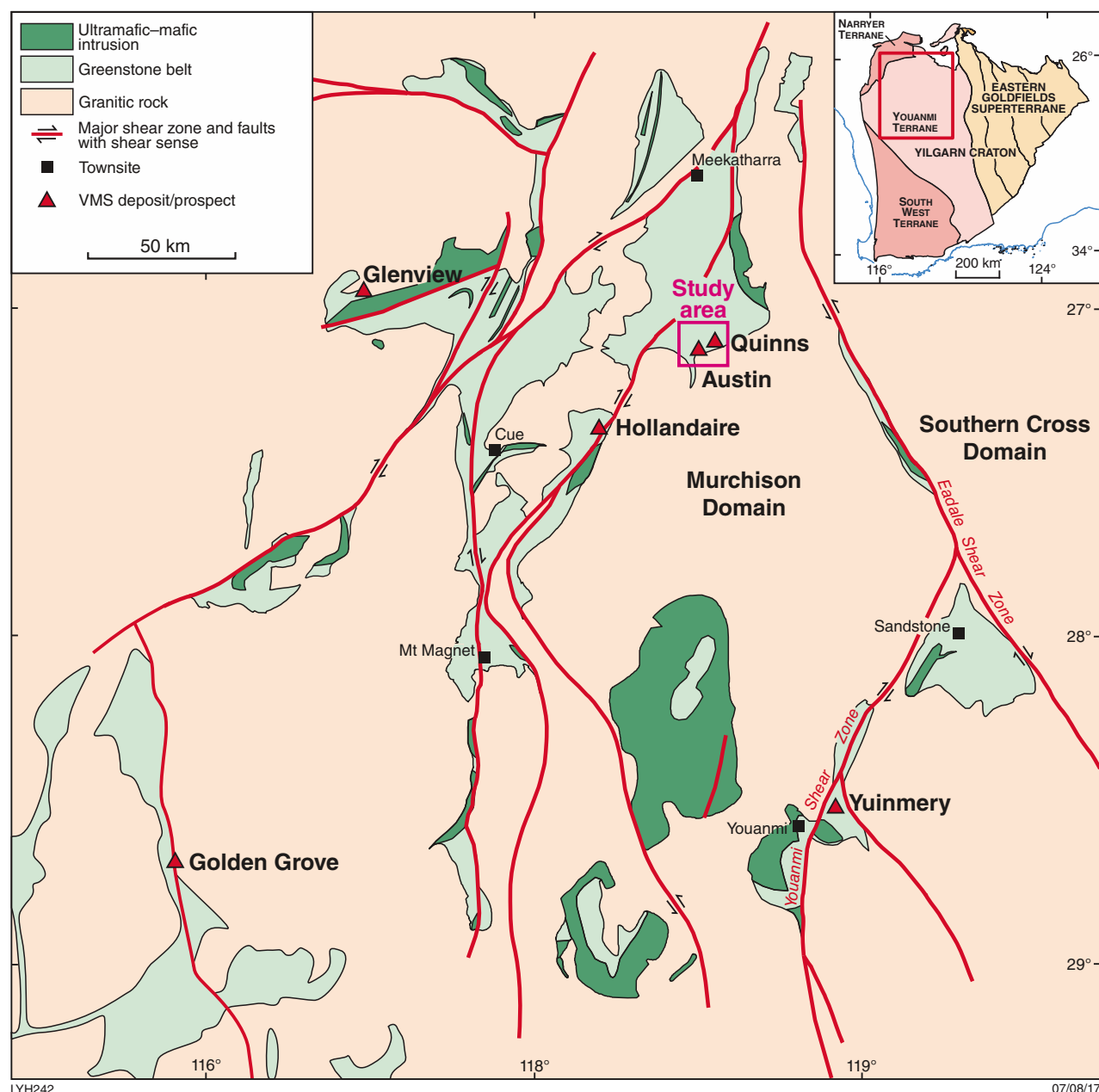


Figure 1. Simplified geological map of the northern Youanmi Terrane showing location of Austin–Quinns and other VMS deposits and prospects (adapted from Guilliamse, 2014)

in Maniw and Fitton [1987]). CRA Exploration Pty Ltd intersected massive to semimassive sulfide mineralization over a strike length of 700 m at their Dalmation Prospect, which was interpreted to be an extension of the Quinns gossan; intersections included 1 m at 24.3% Zn, 1.1% Pb and 10.5 g/t Ag in 90QND006; 2.3 m at 8.5% Zn and 1.6 m at 4.7% Zn in 90QND012; and 3.6 m at 3.0% Zn, 0.62% Cu, 0.29% Pb and 11.4 g/t Ag in 90QND007 (Bishop, 1991, 1992a).

CRA Exploration Pty Ltd also explored to the southwest of Quinns. The company drilled a combined bipolar magnetic anomaly associated with a transient electromagnetic

conductor (SIROTEM) and gravity anomaly, which they named the Ridgeback Prospect, and obtained intersections up to 48.3 m at 0.83% Cu, 0.46% Zn, 0.7 g/t Ag and 0.25 g/t Au (Bishop, 1992b). Silver Swan Group carried out further drilling at this prospect in 2008, which they renamed Austin. Their first diamond drillhole intersected significant mineralization including 25.2 m at 13.7% Zn, 33.55 m at 1.7% Cu, 7 m at 1.3 g/t Au and 18.6 g/t Ag (Silver Swan Group Limited, 2008). Silver Swan Group announced a maiden resource of 1.48 Mt at 1.02% copper, 1.39% zinc, 3.51 g/t silver and 0.24 g/t gold at Austin in 2010 (Silver Swan Group Limited, 2010a).

Core from five diamond drillholes drilled by Silver Swan Group under the Exploration Incentive Scheme (EIS) was included in this study. This included core from ATD101 drilled to test the Austin mineralization at depth, 10TJD001 drilled at the T&J Prospect (renamed the Tasman Prospect by Silver Swan in 2011), 09DKRCD001A drilled 2.7 km southwest of Newmont's Dicksons Prospect (and referred to as 'Dicksons (Silver Swan)' in this Record), 09FKRCD001 drilled to test a magnetic anomaly called the Franklin Prospect, and 09HBRCD001 drilled to test a magnetic anomaly at the Herbert Prospect, 2.5 km north of Austin. In addition, core from three drillholes through the Austin deposit (09ATD015, 09ATD019 and ATD025), and one drillhole from the Robert Prospect immediately north of Austin (09RTD001) was loaned to the GSWA for the purpose

of the study. The position of all prospects and studied drillholes is shown on Figure 2. Drillhole collars are given in Table 1.

One of the conditions of the loan of the core was that no geochemistry was to be performed as Silver Swan Group Limited was planning a separate study on the geochemistry. Some of the geochemistry was carried out by the late Rob Kerrich and some by Paul Duuring at The University of Western Australia. Subsequently, the author collaborated with Paul Duuring to write a more inclusive paper on the mineralization in the Quinns district combining his geochemical work with the author's study of alteration (Duuring et al., 2016). The purpose of this Record is to give a more detailed account of the mineralization, lithology and alteration in the studied drillholes.

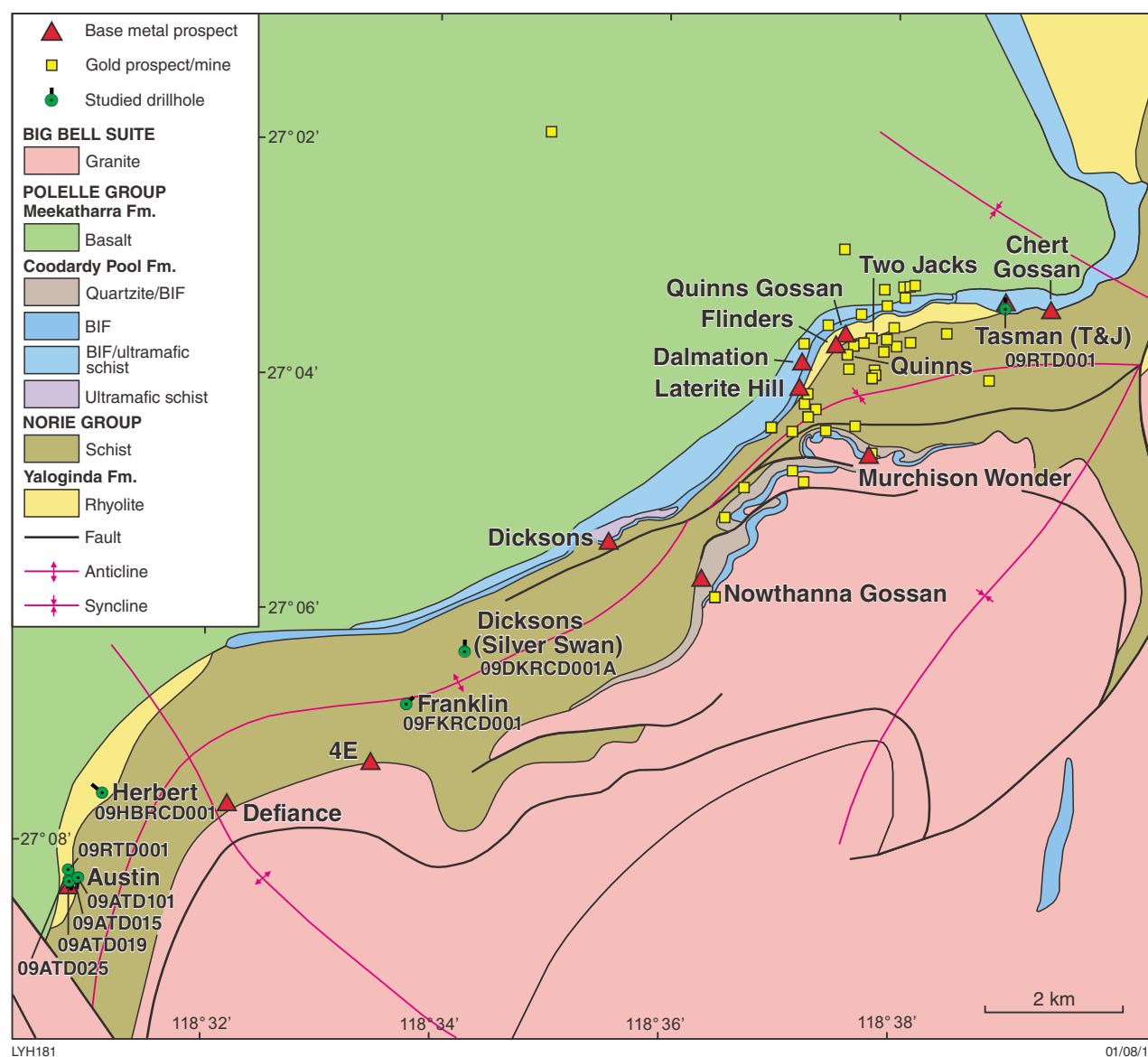


Figure 2. Geological map of the Austin–Quinns area showing locations of VMS prospects and studied drillholes (based on Van Kranendonk [2011] and revised by Geological Survey of Western Australia [2017])

Table 1. Drillhole locations for studied diamond drillholes in the Austin–Quinns area

<i>Prospect</i>	<i>Drillhole</i>	<i>Collar easting</i>	<i>Collar northing</i>	<i>Zone</i>	<i>Azimuth</i>	<i>Dip</i>	<i>Depth</i>
Austin	09ATD015	650085	6997272	50	190	–60	369.40
Austin	09ATD019	650028	6997228	50	190	–60	233.30
Austin	09ATD025	650028	6997270	50	190	–60	261.20
Austin	10ATD101	650152	6997430	50	184	–60	555.85
Robert	09RTD001	650016	6997416	50	190	–60	305.20
Herbert	09HBRCD001	650505	6998630	50	310	–60	408.85
Franklin	09FKRCD001	654900	7000025	50	40	–60	306.00
Dicksons	09DKRCD001A	655682	7001036	50	360	–60	360.20
Tasman	10TJD001	663560	7006250	50	360	–60	340.00

Geologic setting

The Austin–Quinns deposits and prospects are located in the southern part of the Meekatharra greenstone belt in the Youanmi Terrane. The Quinns area was first mapped in detail (1 inch = 10 chains or 1:7920) by Feldtmann (1921), who showed two areas of quartz–chlorite, quartz–andalusite, and chlorite–talc schist surrounded by mafic igneous rock with included conformable to semiconformable ferruginous jasper (Fig. 3a). Feldtmann (1921) interpreted the schists to be metamorphosed sedimentary rocks. Newmont Pty Ltd mapped the Quinns area at 1:10 000 in 1976 and, on the basis of rhyolitic agglomerates to the south of the Quinns and Dixons gossans, concluded that the schists were derived from acid volcanic rocks that had been exposed in the cores of two anticlinal structures, and which were separated from the overlying basic volcanic rocks by banded iron-formation (BIF) or exhalite (Newmont Pty Ltd, 1977, 1978). A similar interpretation was shown in the map of Maniw and Fitto (1987) for CRA Exploration Pty Limited (Fig. 3b).

The Quinns–Austin area was mapped at 1:250 000 by Tingey (1985) and, more recently, at 1:100 000 as part of the Geological Survey of Western Australia's (GSWA) regional mapping program (Van Kranendonk, 2011; GSWA 2017). Van Kranendonk (2011) correlated mapped areas of felsic volcanic rocks and interbedded BIF with the 2815–2800 Ma Yaloginda Formation of the Norie Group. He also assigned the andalusite–chlorite (–kyanite–muscovite) schist he mapped along the anticlinal axis to the Norie Group. Van Kranendonk (2011) correlated the basalt to the 2800–2760 Ma Meekatharra Formation of the Polelle Group, and named the interlayered BIF, quartzite and ultramafic schist at the base of the basalt the Coodardy Poole Formation which he assigned to the Polelle Group. The felsic volcanic rocks and schists are intruded to the east by monzogranite that Van Kranendonk (2011) correlated with the 2735–2690 Ma Big Bell Suite of the Austin Downs Supersuite (Figs 2, 3c). Zelic et al. (2012) also mapped ?intrusive feldspar porphyry in structural highs (Fig. 3d).

Newmont Pty Ltd (1977, 1978), Maniw and Fitton (1987), Tingey (1985), Vearncombe (2010) and Van Kranendonk (2011) all showed a northeast–southwesterly trending

anticlinal axis through the Quinns area. On the basis of aeromagnetic data, Van Kranendonk (2011) showed this anticline extending westwards and then southwestwards to Austin (Figs 2, 3c) in accordance with the interpretation of Vearncombe (2010). However, Vearncombe (2010) and Silver Swan Group (2010b) interpreted complex refolding at Austin as shown schematically in Figure 4a. An alternative interpretation of structure at Austin is given in Figure 4b after Duuring et al. (2016). Zelic et al. (2012) interpreted very complex large sheath-fold geometries in the Quinns area (Fig. 3d), which they interpreted to have developed during a single-stage tectonic event by progressive, non-coaxial, heterogeneous deformation. In the model of Zelik et al. (2012), a single BIF unit is structurally repeated by complex folding together with structural repetition of the basalt and schist after felsic volcanic rocks (Fig. 3d). A simpler explanation is that there are three (or more) BIF units interbedded with basalt as mapped by Feldtmann (1921; Fig. 3a), Newmont Pty Ltd (1977, 1978), Maniw and Fitton (1987; Fig. 3b) and Silver Swan Group Limited (2011). This explanation is more consistent with the mapping of Van Kranendonk (2011) who showed interlayered BIF and ultramafic schist, interlayered BIF and amphibolite schist, and quartzite of the Coodardy Poole Formation at the base of the Polelle Group (Figs 2, 3c). The deformation makes interpretation of facing directions at Austin difficult but there is no evidence for physical mobilization of sulfides (Duuring et al., 2016).

Method

HyLogger data were used in conjunction with conventional logging, petrography and scanning electron microscope (SEM) analysis to study the alteration and mineralization at Austin–Quinns. Logs of all studied drillholes are given in Appendix 1 (on zip file). The logs include the sample numbers of those samples examined petrographically. A total of 79 thin sections and 191 polished thin sections was examined using reflected and transmitted light microscopy to gain an understanding of the host rocks and the nature of the mineralization and alteration, as well as the effects of deformation and metamorphism.

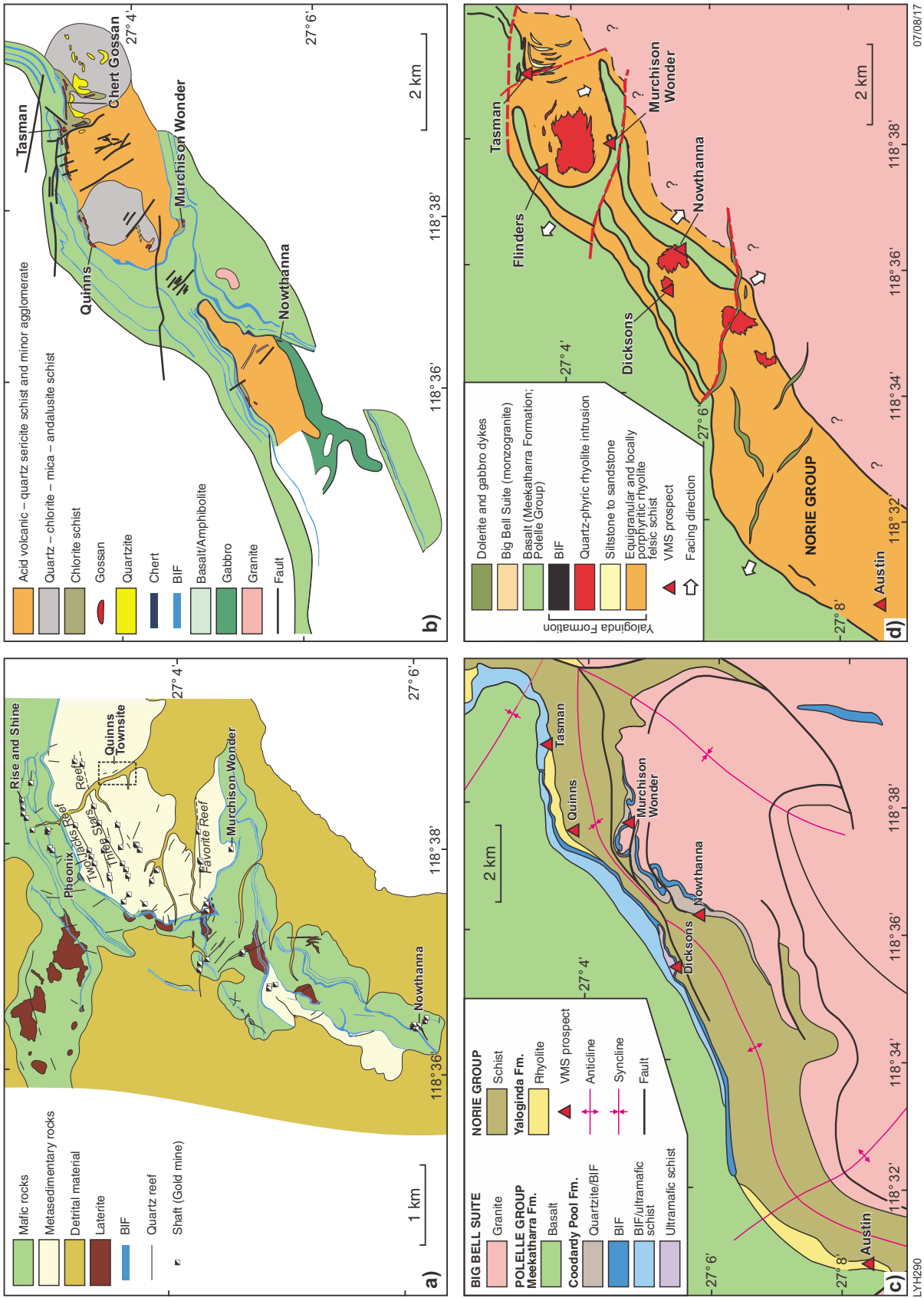


Figure 3. Different interpretations of the geology in the Quinns area: a) Feldmann (1921); b) Maniwi and Fitton (1987); c) based on Van Kranendonk (2011) and revised by Geological Survey of Western Australia (2017); d) Zelic et al. (2012)

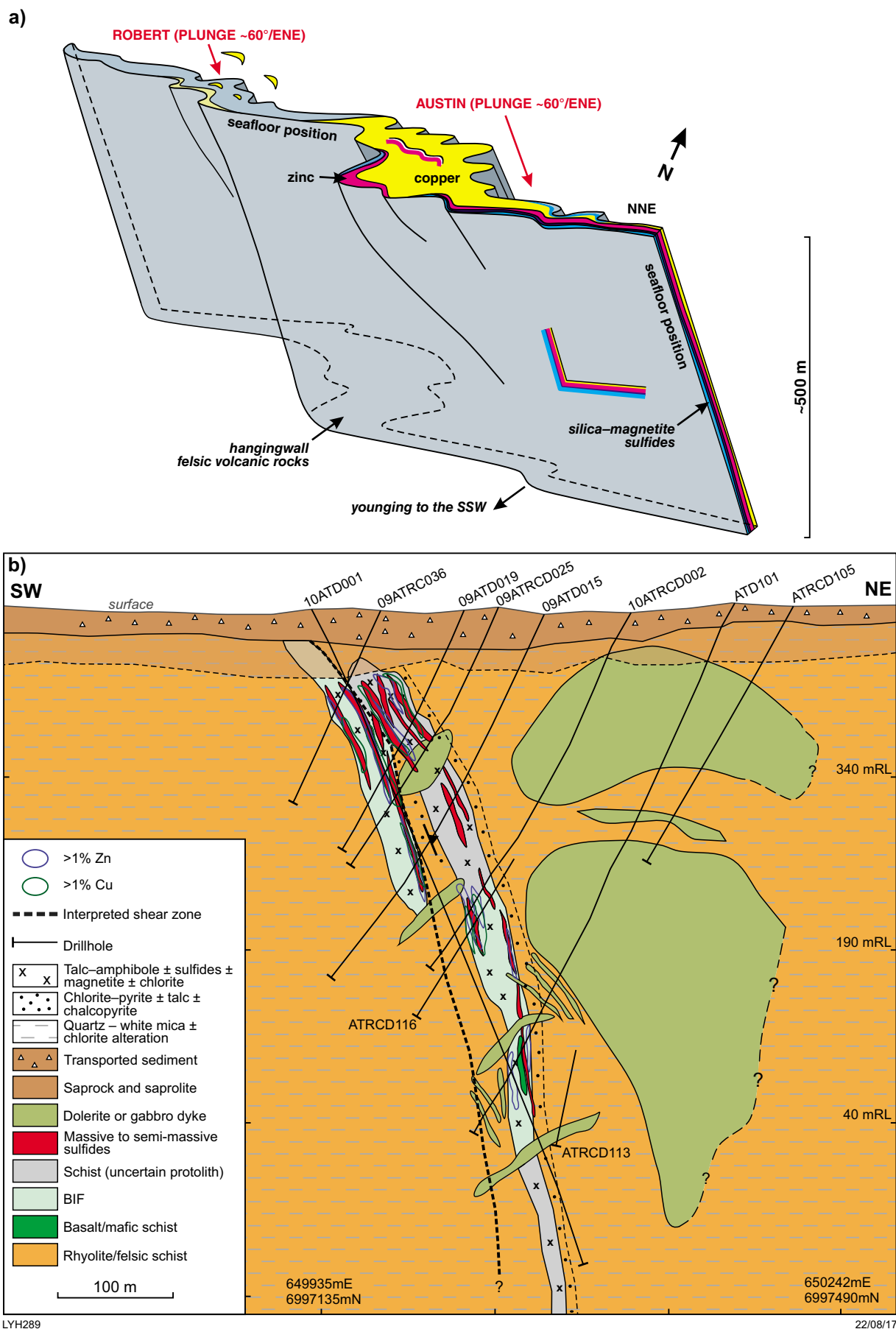


Figure 4. Interpretation of structure at Austin: a) after Vearcombe (2010) and Silver Swan Group (2010b); b) after Duuring et al. (2016)

All diamond drillholes were scanned using the HyLogger at GSWA's Perth Core Library in Carlisle. Drillcore from ATD101, 09ATD019, 09ATD015, 09ATD025, 09RTD001, 09DKRCD001A and 10TJD001 was scanned using the short wave infrared (SWIR) and visible near infrared (VNIR) spectrometers only. Following the addition of a thermal infrared (TIR) spectrometer to the HyLogger, core from 09HBRCD001, 09FKRCD001, 09DKRCD001A and 10TJD001 was scanned using this extended spectral range. The HyLogger data were analysed using The Spectral Geologist (TSG), a program developed by CSIRO Earth Science and Resource Engineering and marketed by Aussec International Pty Ltd. This program compares the acquired spectra with representative spectra of known minerals and provides a system-generated interpretation of the minerals for each interval analysed (Pontual, 2008; Hancock et al., 2013). The three main minerals contributing to the spectra are calculated for each interval (approximately 8 mm) for TIR, and the two main minerals are calculated for SWIR. A summary plot is calculated by averaging these over a larger chosen interval (1–3 m depending on length of drillhole). SWIR is best for identifying micas, chlorite and clay minerals, whereas TIR is best at identifying quartz, feldspars, pyroxenes, garnet and phosphates. Both can identify Ca-amphiboles, talc and carbonates (Hancock et al., 2013). VNIR is good for identifying iron oxides (Hancock and Huntington, 2010) and rare earth elements (Morin-Ka, 2012).

Given the large numbers of possible overlaps of absorption features from different minerals, particularly for TIR, it is not surprising that the system-generated interpretation of minerals is commonly incorrect. Fortunately, TSG has the ability to modify the list of searchable minerals. Appendix 2 gives the list of allowed and not allowed minerals used for the Austin–Quinns core determined by trial and error and utilizing petrological observations from thin sections as a guide.

The scatter plot option in TSG allows individual minerals to be plotted downhole using either the first or second (or third in the case of TIR) most abundant mineral identified in each 8 mm interval. It was more useful to get TSG to calculate a combined weighted average for the mineral regardless of whether it is the first, second or third mineral. Where a particular mineral is not in the TSG library, spectral matching with another spectral library can be carried out and the results plotted downhole as described above. The wavelength of the absorption features of some minerals such as chlorite and white mica varies with the composition of the mineral as described by McLeod et al. (1987), Herrmann et al. (2001) and Pontual (2008). For this study, TSG was used to calculate a polyfit scalar (PFIT) for the c. 2254 nanometre wavelength absorption feature for chlorite and the c. 2200 nanometre wavelength absorption feature for white mica. To ensure that no data from minerals with absorption features at a similar wavelength were included (e.g. prehnite can give false white mica results), a class extract was made of just the chlorite group and the white mica group, respectively. These values were then plotted downhole. The scatter plots show both the range in wavelength at a given depth which is dependent both on the variation in the mineral composition and a reflection of interference from nearby

minerals and the variations with depth. The PFIT scalar was also used to determine the downhole abundance of Ca-poor amphiboles using the method of Hassan (2014) which in turn was based on an observation (J Huntington, 2013, written comm., 28 August) that these amphiboles showed an absorption feature at about 980 nanometres.

Assay and simplified geological drillhole logs were imported into TSG and displayed along with the other scatter plots.

An FEI XL40 SEM fitted with a Bruker X-flash 5030 energy dispersive x-ray detector (EDS) at the Earth Science and Resource Engineering division of CSIRO at Kensington, Western Australia was used to assist with identification of minerals and to confirm the variation in composition of alteration minerals suggested by the HyLogger. Results were recalculated to 100% using the Quantax Esprit EDS program of Bruker Nano GmbH, Germany. As no standards were incorporated, this method is semiquantitative and does not take into account the amount of water in minerals such as chlorite. However, the method is useful for monitoring variations in the ratio of Mg to Fe in various silicates to compare with the HyLogger results. In the case of very small grains, backscatter of electrons from adjacent grains led to inaccurate results. The SEM was also unable to accurately measure the amount of sulfur in telluride grains due to overlapping peaks.

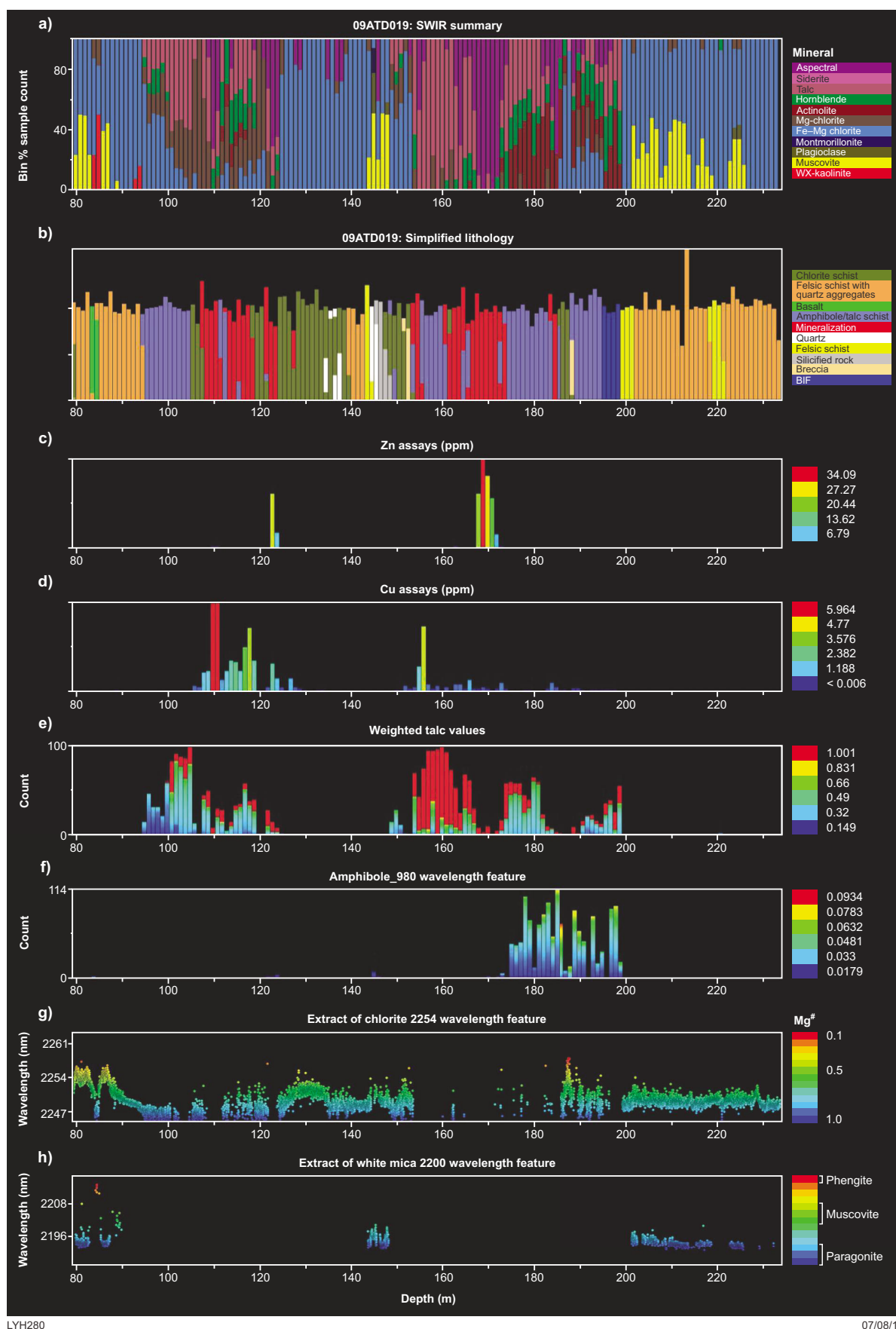
For those minerals where the SEM results were not sufficiently accurate, the JEOL 8530F microprobe at the Centre for Microscopy, Characterisation and Analysis at The University of Western Australia was used for analysis. This microprobe is equipped with five wavelength-dispersive crystal spectrometers, one JEOL silicon-drift energy-dispersive spectrometer and an optical microscope for focusing.

Prospect lithology, mineralization and alteration

As there is significant uncertainty about the stratigraphic relationship of the different prospects, they are considered separately below.

Austin

Austin is the only prospect with a defined resource. Diamond drillhole 09ATD019 intersected two zones of zinc and copper mineralization including some very high-grade zinc mineralization in the lower zone. Two zones of lower grade mineralization were also intersected in 09ATD015. Low-grade mineralization was also intersected in 09ATD025 but this was disrupted by a dolerite intrusion. Diamond drillhole 10ATD101 (also referred to as ATD101), was drilled to test the Austin mineralization at depth. Logs for drillholes 09ATD019, 09ATD015, 09ATD025 and ATD101 are given in Appendix 1a–d (on zip file); they are included pictorially in Figures 5–8.



LYH280

07/08/17

Figure 5. HyLogger, lithology and assay data for drillhole 09ATD019 from Austin: a) SWIR summary plot; b) simplified lithology; c) Zn assays; d) Cu assays; e) weighted talc values; f) distribution of Ca-poor amphiboles on basis of the 980 absorption feature; g) chlorite wavelength; h) white mica wavelength

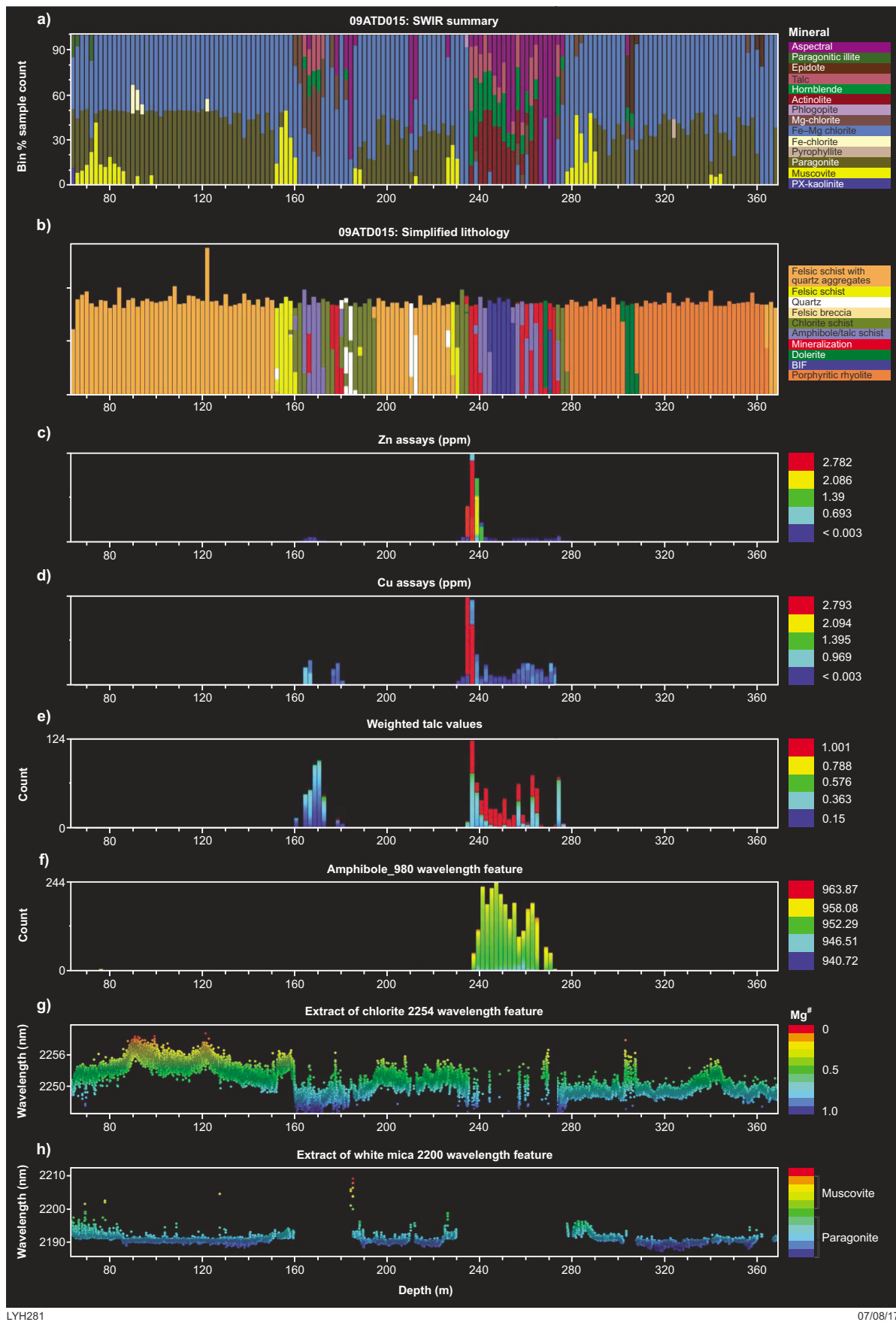
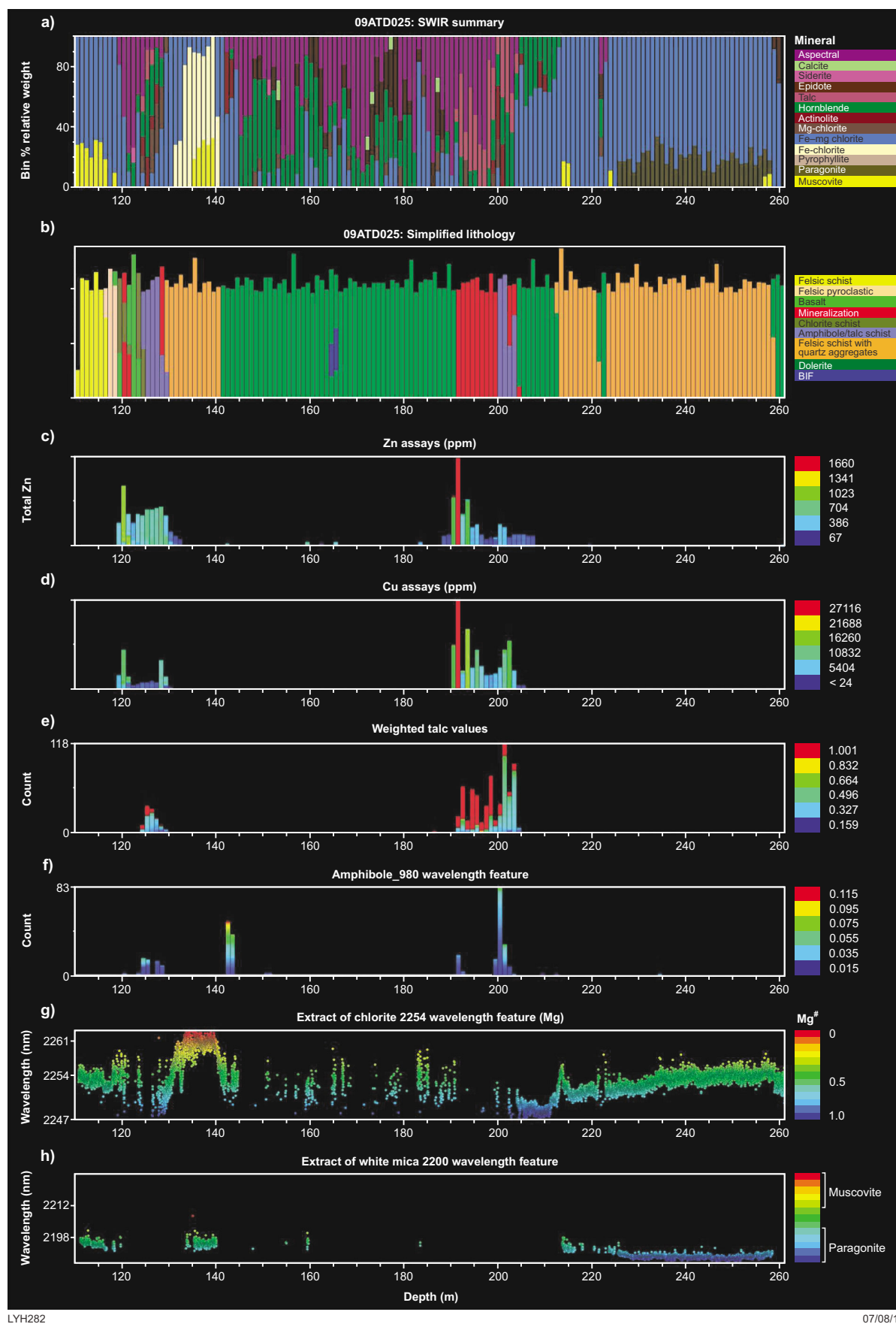


Figure 6. HyLogger, lithology and assay data for drillhole 09ATD015 from Austin: a) SWIR summary plot; b) simplified lithology; c) Zn assays; d) Cu assays; e) weighted talc values; f) distribution of Ca-poor amphiboles on basis of the 980 absorption feature; g) chlorite wavelength; h) white mica wavelength



LYH282

07/08/17

Figure 7. HyLogger, lithology and assay data for drillhole 09ATD025 from Austin: a) SWIR summary plot; b) simplified lithology; c) Zn assays; d) Cu assays; e) weighted talc values; f) distribution of Ca-poor amphiboles on basis of the 980 absorption feature; g) chlorite wavelength; h) white mica wavelength



LYH283

07/08/17

Figure 8. HyLogger, lithology and assay data for drillhole ATD101 from Austin: a) SWIR summary plot; b) simplified lithology; c) Zn assays; d) Cu assays; e) weighted talc values; f) distribution of Ca-poor amphiboles on basis of the 980 absorption feature; g) chlorite wavelength; h) white mica wavelength

Lithologies intersected

All of the rocks described below have been metamorphosed to at least greenschist facies, but the term 'meta' has been omitted for the sake of brevity. Many of the rocks have also been sheared or are highly altered and their protoliths are uncertain.

Felsic rocks

Abundant rocks of felsic composition were intersected above and below mineralization in all of the drillholes from Austin.

Porphyritic rhyolite

Rhyolite with phenocrysts of plagioclase and quartz in a fine-grained matrix of quartz, feldspar, white mica and chlorite was intersected in the interval 483.1 – 544.8 m in diamond drillhole ATD101 (Fig. 9a). Feldspar phenocrysts were not observed in any of the other Austin drillcore and have probably been completely altered. However, many samples contain remnant quartz phenocrysts (Fig. 9b) suggesting that the rock was originally a porphyritic rhyolite. Duuring et al. (2016) found that these rocks fall in the rhyolite field when plotted on the log Zr/TiO₂ vs log Nb/Y discrimination diagram of Winchester and Floyd (1977).

Felsic pyroclastic rocks

Very few rocks with definite pyroclastic textures were observed. One example from ATD101 that is interpreted to be of pyroclastic origin contains clasts of porphyritic rhyolite (Fig. 9c) and irregular fragments that may have been pumice or volcanic glass (Fig. 9d). Some compositionally layered fine-grained rocks are possibly also felsic tuffs.

Felsic schist with quartz aggregates

Schist with irregular to oval-shaped aggregates of quartz in a schistose matrix of quartz, chlorite and white mica (Fig. 9e) is interpreted to be derived from sheared porphyritic rhyolite although it could also be after quartz crystal tuff.

Recrystallized felsic rock

Light-grey massive rock composed of a mosaic of fine-grained quartz, white mica and chlorite with no obvious phenocrysts (Fig. 9f) is interpreted to be recrystallized nonporphyritic rhyolite or felsic tuff but a metasedimentary origin cannot be ruled out.

Felsic schist

Quartz–chlorite–white mica and quartz–chlorite schists probably originated as rhyolite or felsic tuff as they have trace element geochemistry consistent with derivation from rhyolite (Duuring et al., 2016).

Felsic intrusions

A narrow, light-pink feldspar porphyry intrusion was intersected at 231.7 m in ATD101.

Banded iron-formation (BIF)

Recognizable BIF has a close spatial relationship with the lowermost mineralized zone in 09ATD019 and 09ATD015 and also with mineralization in ATD101. Magnetite-rich laminae alternate with silicate-rich laminae composed of anthophyllite, talc, quartz and minor chlorite (Fig. 10a,b). In places, there is minor sphalerite included in the silicate-rich layers (Fig. 10c) and minor pyrite is also commonly associated with BIF.

Basalt

Thin zones of fine-grained mafic rocks interpreted as basalt, or possibly pre-deformation dolerite, were intersected in close proximity to BIF in ATD101 (Fig. 11a) and within rhyolite in the upper part of 09ATD019 (Fig. 11b). Trace element geochemistry of these (using the discrimination plot of Winchester and Floyd, 1977) was consistent with basalt (Duuring et al., 2016).

Mafic tuff

Layered rocks composed dominantly of chlorite and hornblende with abundant disseminated ilmenite and thin layers of quartz and plagioclase (Fig. 11c) intersected in ATD101 are interpreted as being after mafic tuff. Alternatively, these rocks could be sheared basalt.

Mafic intrusions

At least two generations of dolerite are present in ATD101. Massive medium-grained dolerite with fine-grained chilled margins intruded the felsic rocks. In places, massive dolerite was intruded by smaller bodies of later fine-grained dolerite. Massive dolerite also intrudes the sequence including mineralization in 09ATD025. A fine-grained dolerite dyke stopes out mineralization in 09ATD015.

Amphibole–talc schist and chlorite schist

Schist composed of talc and variable amounts of cummingtonite, anthophyllite and in places, hornblende is interlayered with mineralization and BIF. Schist composed dominantly of chlorite is more distal to mineralization. The protolith of these schists is highly uncertain. They could represent highly altered felsic volcanic rocks, silicate-facies BIF, or have a more mafic protolith such as basalt or mafic tuff. One example, composed of chlorite with minor talc, phlogopite, apatite, quartz, ilmenite and sulfides (Fig. 11d) from the interval 150.5 – 153.5 m in drillhole 09ATD019, has trace element geochemistry consistent with basalt (Duuring et al., 2016). However, many other samples of chlorite and amphibole–talc schist analysed by Duuring et al. (2016) have trace element geochemistry consistent with rhyolite when plotted on the log Zr/TiO₂ vs log Nb/Y discrimination diagram of Winchester and Floyd (1977). It should be noted that these samples were analysed using the four-acid digest method, and there may have been incomplete digestion of the incompatible elements.

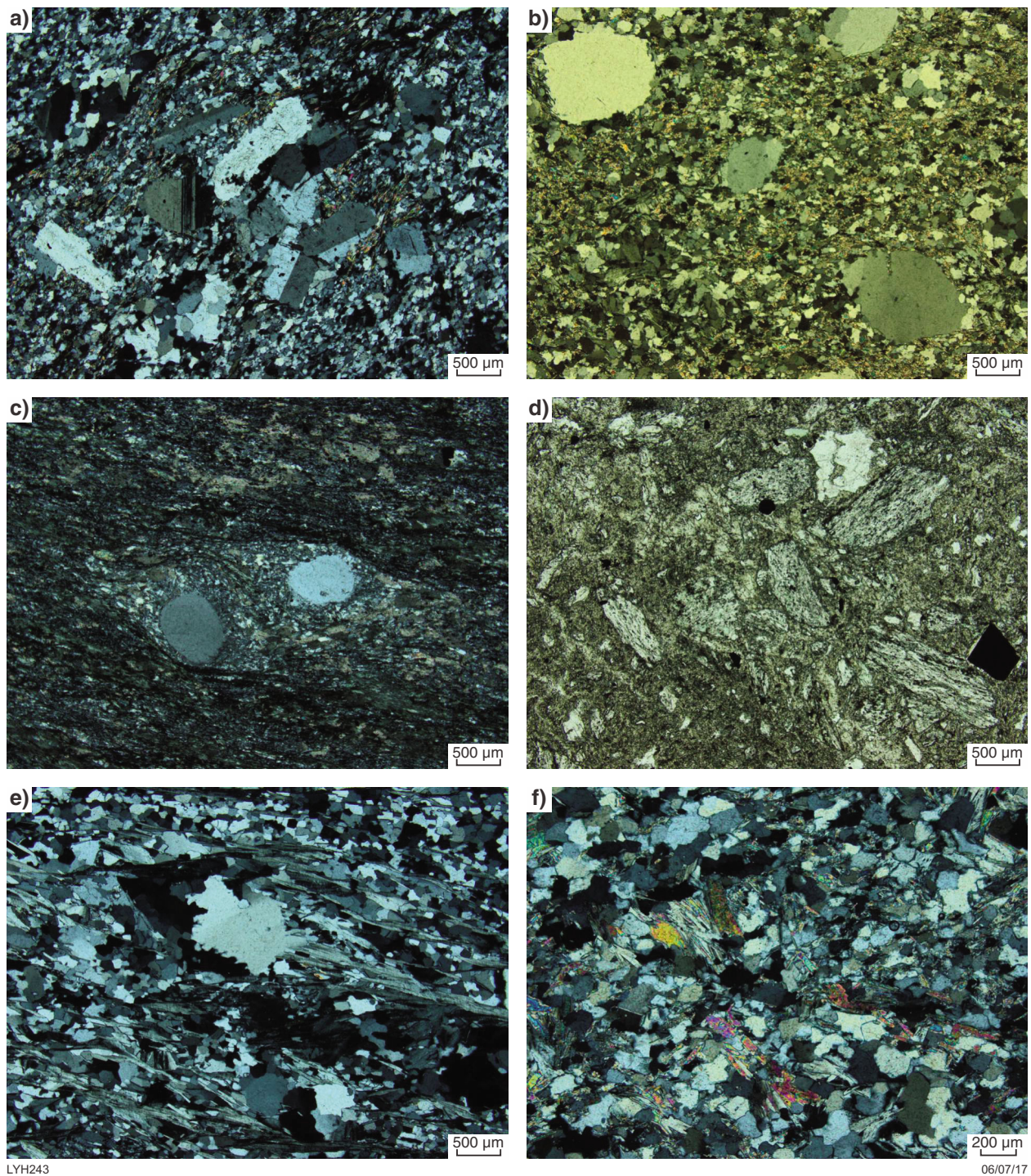


Figure 9. Felsic rocks from the Austin drillholes: a) rhyolite with plagioclase phenocrysts (GSWA 208152 from 498.2 m in ATD101), crossed polars; b) rhyolite with quartz phenocrysts (GSWA 204760 from 336.4 m in 09ATD15), crossed polars; c) tuff with clast of porphyritic rhyolite (GSWA 116782 from 215.5 m in ATD101), crossed polars; d) tuff with possible pumice fragments (same sample as c), plane-polarized light; e) felsic schist with quartz aggregates interpreted to be after porphyritic rhyolite (GSWA 204193 from 232.2 m in 09ATD15), crossed polars; f) recrystallized non-porphyritic rhyolite (GSWA 116776 from 174.5 m in ATD101)

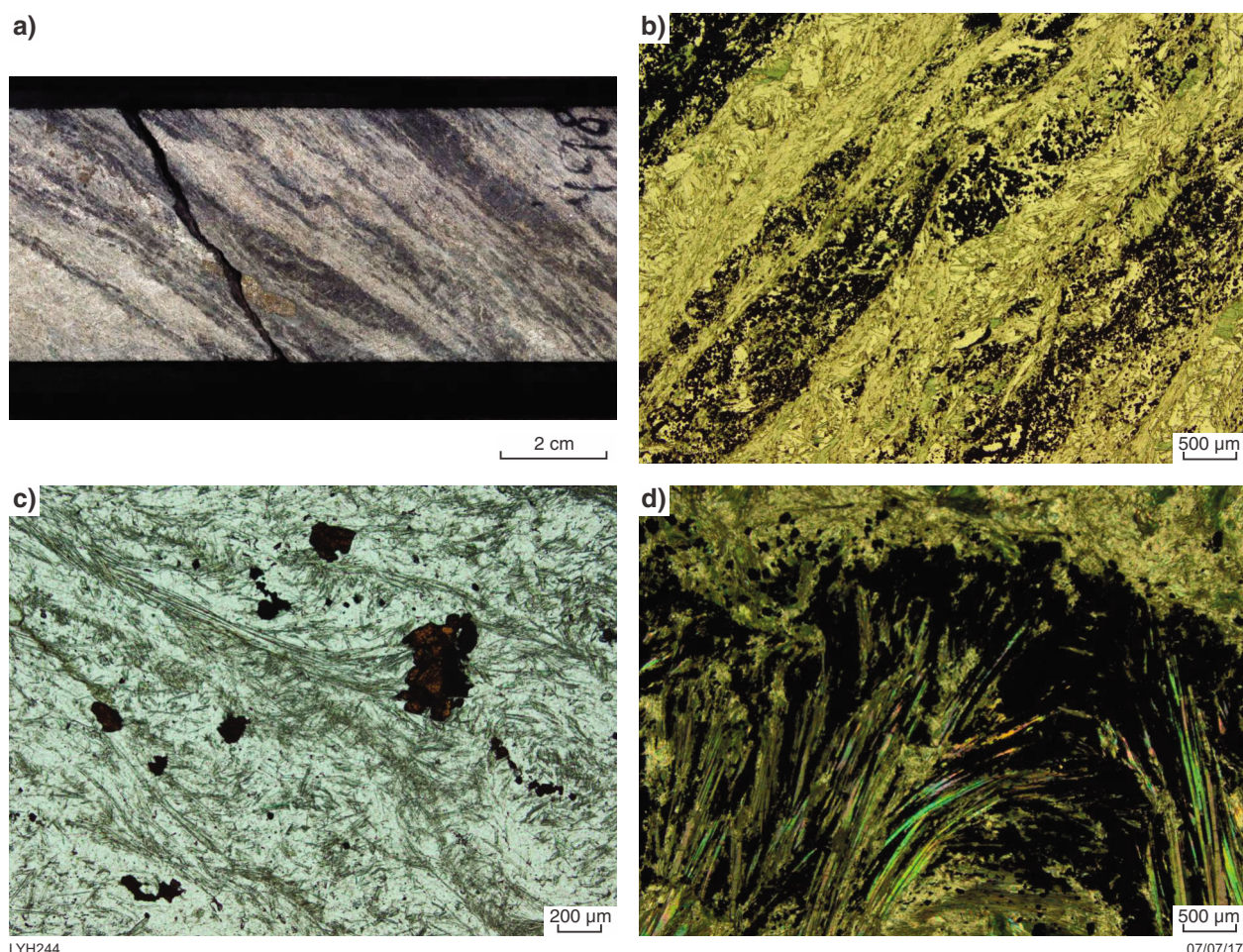


Figure 10. BIF from Austin: a) core from 198.0 m in 09ATD019; b) BIF with layers of magnetite alternating with silicate-rich laminae composed of anthophyllite, talc, quartz and minor chlorite (GSWA 204912 from 198.0 m in 09ATD019, same sample as a), plane-polarized light; c) anthophyllite-rich layer in BIF with included sphalerite (reddish brown) (GSWA 208149 from 451.8 m in ATD101), plane-polarized light; d) anthophyllite growing across magnetite-rich layers (GSWA 204748 from 240.0 m in 09ATD15), crossed polars

Mineralization

Two broad highly altered and mineralized zones were intersected by drillholes 09ATD019 and 09ATD015. These zones are composed of talc schist, talc–amphibole schist and minor chlorite schist with disseminated sulfides, and have intercalated zones of massive to semimassive sulfides. It is possible that these zones are the same horizon that has been repeated by folding or faulting, but there are some differences in the composition of the chlorites and amphiboles in these zones as discussed in the alteration section. Also, only the lowermost zone in each of these two diamond drillholes includes recognizable oxide-facies BIF although the amphibole–talc schist could have originated as silicate-facies BIF. Mineralization is also associated with a zone of alteration in 09ATD025, but this zone has been intruded by dolerite making correlations with the other drillholes difficult. Zinc mineralization occurs in the lowermost zone in both 09ATD019 and 09ATD015 and is also present in the upper mineralized zone in 09ATD019. Low-grade

zinc mineralization was also intersected at depth in 09ATD101. Copper mineralization was intersected above the zinc mineralization in the upper and lower altered zone in 09ATD019 and above the Zn mineralization in the lower altered zone in 09ATD015. Low-grade copper mineralization is associated with the zone of alteration in 09ATD025. Reported significant base metal intersections from these drillholes are given in Table 2, and the Cu and Zn grades downhole are shown in Figures 5–8.

The highest grade zinc ore intersected in the studied drillcore was in 09ATD019 where the 5 m interval 167–172 m assayed 21.4% Zn, 0.2% Cu and 1.2g/t Ag (Silver Swan Group Limited, 2009). In this interval, layers composed mainly of sphalerite alternate with pyrite-rich layers and talc (Fig. 12a). The sphalerite is a dark reddish brown (iron rich) and typically contains numerous micron-sized inclusions of chalcopyrite and pyrrhotite. The pyrite is euhedral to subhedral and, where completely enclosed in sphalerite, sometimes appears to be embayed by the sphalerite (Fig. 12b). In places, tellurides are included in the pyrite or moulded onto the edges of the crystals (Fig. 12b).

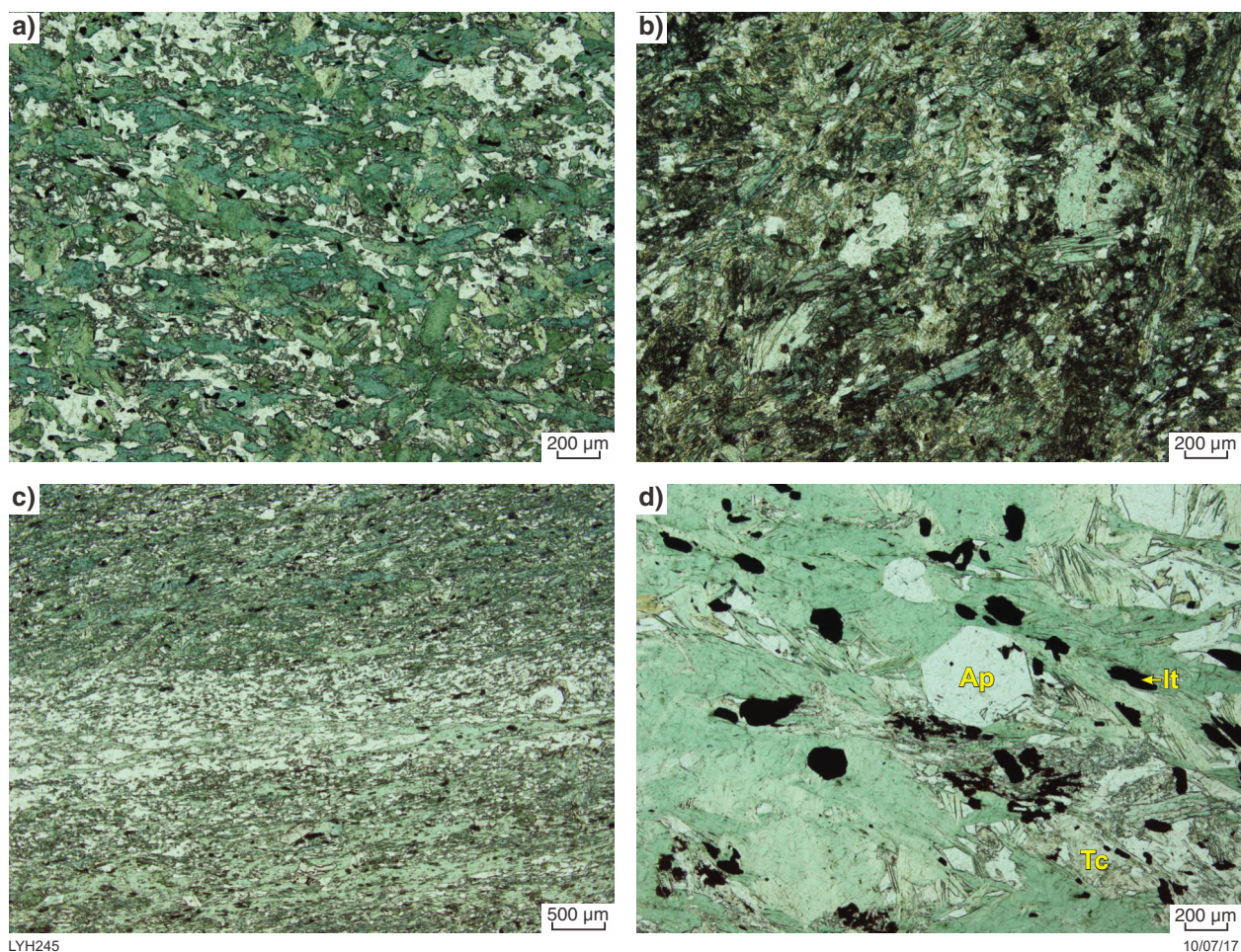


Figure 11. Plane-polarized light micrographs of fine-grained mafic rocks from Austin: a) basalt adjacent to BIF (GSWA 116799 from 447.5 m in ATD101); b) basalt interlayered with rhyolite (GSWA 204784 from 83.9 m in 09ATD19); c) mafic tuff or sheared basalt (GSWA 208139 from 364.2 m in ATD101); d) chlorite schist with minor talc (Tc), euhedral crystal of apatite (Ap) and scattered fine-grained ilmenite (It) (GSWA 204800 from 150.9 m in 09ATD019)

Table 2. Significant intersections in studied diamond drillholes from Austin

Drillhole ID	From	To	Width	Cu %	Zn %	Ag ppm	Au ppm	Source
09ATD015	235	240	5	0.8	1.9	–	–	Silver Swan _ASX 31_7_2009
including	235	236	1	2.8	–	–	–	
09ATD19	107	119	12	2.6	–	8.9	0.73	Silver Swan _ASX 31_7_2009
including	109	111	2	5.9	–	–	–	
	122	124	2	1.6	15.3	5.5	0.40	Silver Swan _ASX 31_7_2009
	151	174	23	0.5	–	3.0	0.16	Silver Swan _ASX 31_7_2009
including	154	156	2	2.8	–	13.2	0.72	
and	167	172	5	0.2	21.0	1.2	0.05	
09ATD025	49	64	15	0.3	–	–	–	Silver Swan _ASX 16_12_2009
	190	203	13	1.0	–	–	–	Silver Swan _ASX 16_12_2009
10ATD101	443	444	1	–	1.4	–	–	Silver Swan _EIS report_April 2011
	451	452	1	–	1.2	–	–	Silver Swan _EIS report_April 2011
	453	454	1	–	4.6	–	–	Silver Swan _EIS report_April 2011

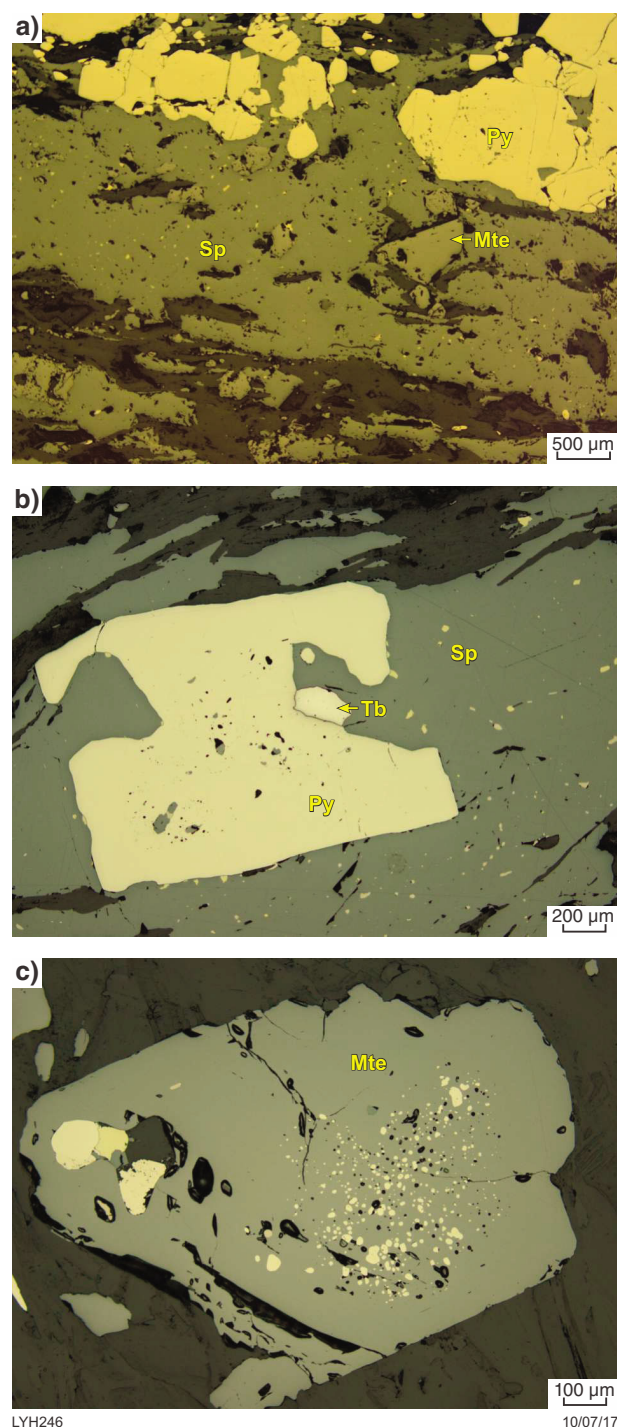


Figure 12. Reflected light photomicrographs of lower zinc-rich horizon at Austin: a) massive ore composed of layers of sphalerite (Sp) and pyrite (Py) with minor magnetite (Mte) (GWSA 204905 from 169.9 m in 09ATD019); b) sphalerite with pyrite and tellurobismuthite (Tb), same sample as a); c) magnetite with central zone containing numerous blebs of pyrite (GWSA 204912 from 198.0 m in 09ATD019)

Magnetite occurs as scattered subhedral to anhedral crystals within the sphalerite (Fig. 12a) and within the silicate layers. Some of the magnetite contains rounded blebs of sulfides (mostly pyrite but less commonly pyrrhotite and chalcopyrite are also present). Some grains show a rim of inclusion-free magnetite (Fig. 12c) suggesting more than one growth phase.

In the deep drillhole ATD101, sphalerite is most abundant in the interval 453.3 – 453.7 m in a fragmental textured rock between BIF and felsic schist after porphyritic ?rhyolite. In this interval, the sphalerite is interstitial to anhedral pyrite and magnetite. Both sphalerite and pyrite are fractured and filled with colloidal silica (Fig. 13a). Low-grade Zn mineralization is also present in BIF between 451 and 452 m in ATD101. Sphalerite was also observed interstitial to silicates and pyrite in basalt or fine-grained dolerite at 448.6 m in ATD101. The sphalerite is yellowish brown and has disrupted and fractured amphibole crystals (Fig. 13b).

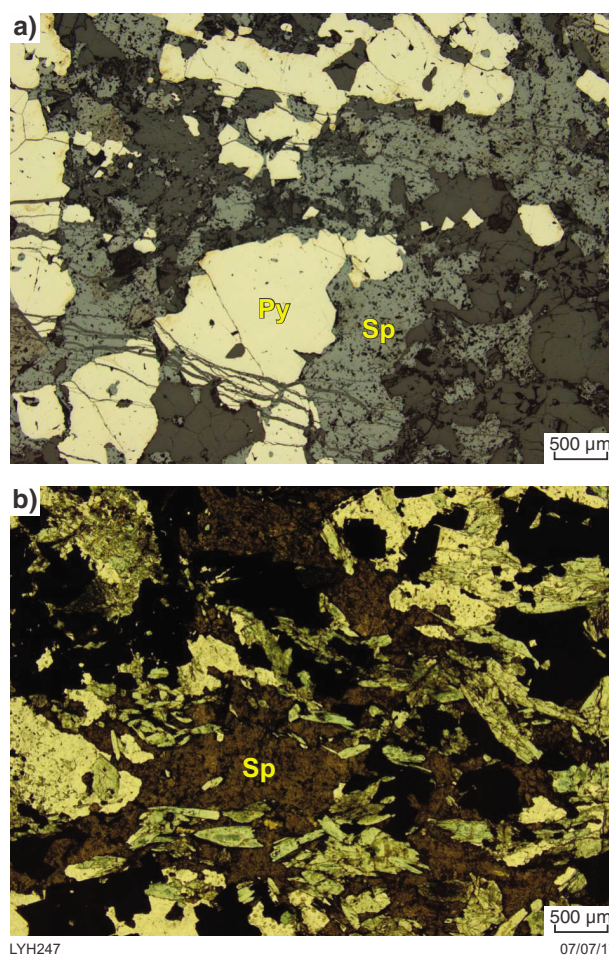


Figure 13. Mineralization at depth at Austin: a) sphalerite (Sp) and pyrite (Py) in mineralized zone from ATD101; both pyrite and sphalerite have been fractured and the fractures infilled with silica (GWSA 208150 from 453.6 m in ATD001), reflected light; b) sphalerite surrounding and disrupting amphiboles in fine-grained mafic rock (GWSA 116800 from 448.6 m in ATD001)

The highest copper grade in the studied drillholes was 2 m at 5.9% Cu from 109–111 m in the upper mineralized zone in 09ATD019. In this interval, chalcopyrite replaces cloudy, inclusion-filled melnikovite pyrite and infills fractures in later clear pyrite (Fig. 14a). Minor sphalerite and tellurides also infill fractures in the clear pyrite (Fig. 14b). The upper part of the lower mineralized zone between 154 and 156 m in 09ATD019 also contains moderate copper mineralization with chalcopyrite and melnikovite pyrite interstitial to subhedral clear pyrite (Fig. 14c).

Massive pyrite with minor chalcopyrite and/or sphalerite was also frequently observed in the Austin drillcore. In places, fragments of massive pyrite were observed in a breccia (Fig. 15a). Within these sulfide fragments, melnikovite pyrite has been partially replaced by clear pyrite (Fig. 15b). The clear pyrite has in turn been replaced by chalcopyrite, pyrrhotite, tellurides and silicates along fractures (Fig. 15c).

In places, pyrite in the fragment shown in Figure 15a is in contact with wisps of molybdenite which have been partially replaced by chalcopyrite and silicates (Fig. 15d). Molybdenite was also observed as a minor phase at 127.8 m, 153.2 m and 179.3 m in 09ATD019. It is hosted by silicates adjacent to pyrite, magnetite and chalcopyrite. Other sulfides observed in the Austin core include very minor galena and aikinite (PbCuBiS_3).

Tellurides identified in the Austin drillcore using electron microprobe analysis include: tellurobismuthite (Bi_2Te_3), tetradyomite ($\text{Bi}_2\text{Te}_2\text{S}$), tsumoite (BiTe), rucklidgeite ($[\text{Bi,Pb}]_3\text{Te}_4$), stützite (Ag_5Te_3), altaite (PbTe), volynskite (AgBiTe_2) and possible poubaite ($[\text{Bi, Pb}]_3[\text{Te, Se, S}]_4$) (Hassan and Roberts, 2017).

Alteration

Intense alteration is a characteristic of all VMS deposits. Summary plots of SWIR data for drillholes 09ATD019, 09ATD015, 09ATD025 and ATD101 are given in Figures 5a, 6a, 7a and 8a, respectively, where they can be compared with simplified lithology (Figs 5b, 6b, 7b and 8b), Zn values (Figs 5c, 6c, 7c and 8c), Cu values (Figs 5d, 6d, 7d and 8d), weighted talc values (Figs 5e, 6e, 7e and 8e), calcium-poor amphiboles as measured by the depth of the 980 nanometre wavelength feature (Figs 5f, 6f, 7f and 8f), chlorite wavelength (Figs 5g, 6g, 7g and 8g), and white mica wavelength (Figs 5h, 6h, 7h and 8h).

Talc

Talc is the dominant silicate in the vicinity of mineralization. In high-grade zinc ore, talc is interlayered with sulfides (Fig. 16a). In lower-grade zones, talc also dominates but shows evidence of replacing other silicates including chlorite, anthophyllite and cummingtonite (Fig. 16b). Both the SWIR summary plots and the weighted talc plots clearly show a broad zone of talc alteration surrounding the mineralized zones. This talc alteration is most intense in the most highly mineralized hole, 09ATD019 (Fig. 5a,e) but talc alteration is evident in association with mineralization in all of the studied drillholes from Austin, including the deep drillhole ATD101 (Fig. 8b,e).

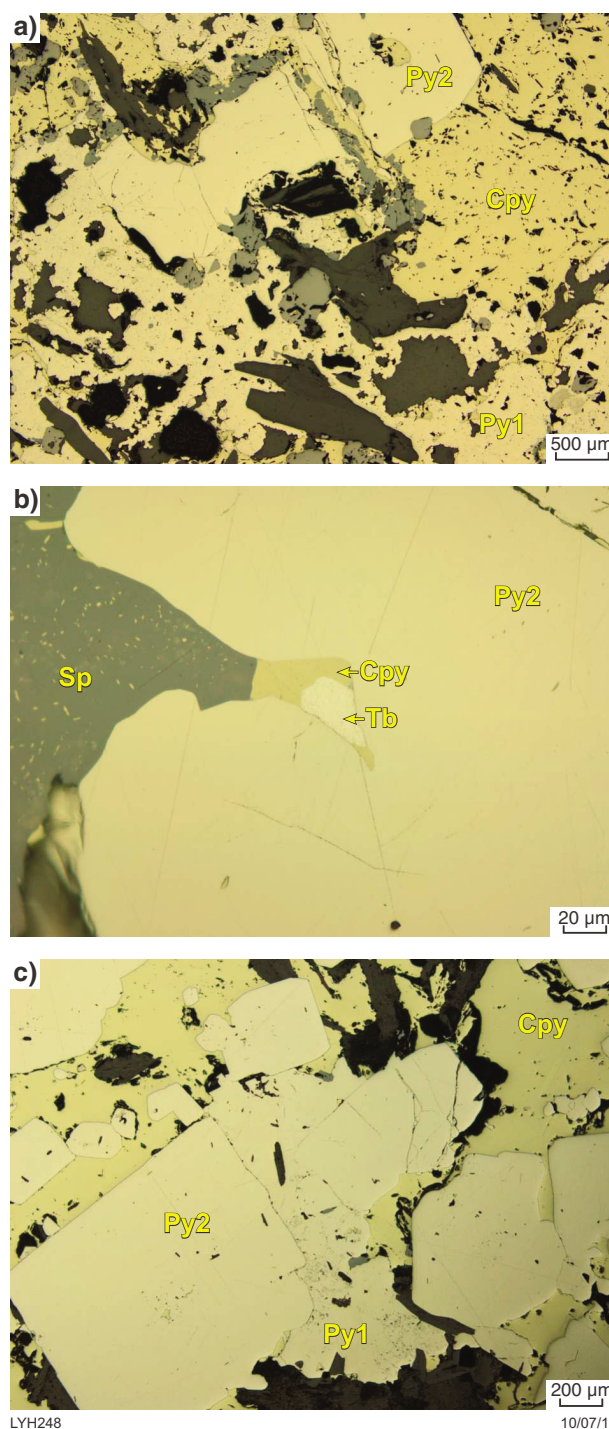


Figure 14. Reflected light photomicrographs of copper-rich mineralization at Austin: a) chalcopyrite (Cpy) replacing cloudy, inclusion-filled melnikovite pyrite (Py1) and infilling fractures in later clear pyrite (Py2) from upper mineralized horizon (GSWA 204790 from 109.8 m in 09ATD019); b) tellurobismuthite (Tb), chalcopyrite and sphalerite (Sp) in clear pyrite, same sample as a); c) chalcopyrite and melnikovite pyrite interstitial to subhedral clear pyrite from upper part of the lower mineralized zone, (GSWA 204790 from 109.8 m in 09ATD019)

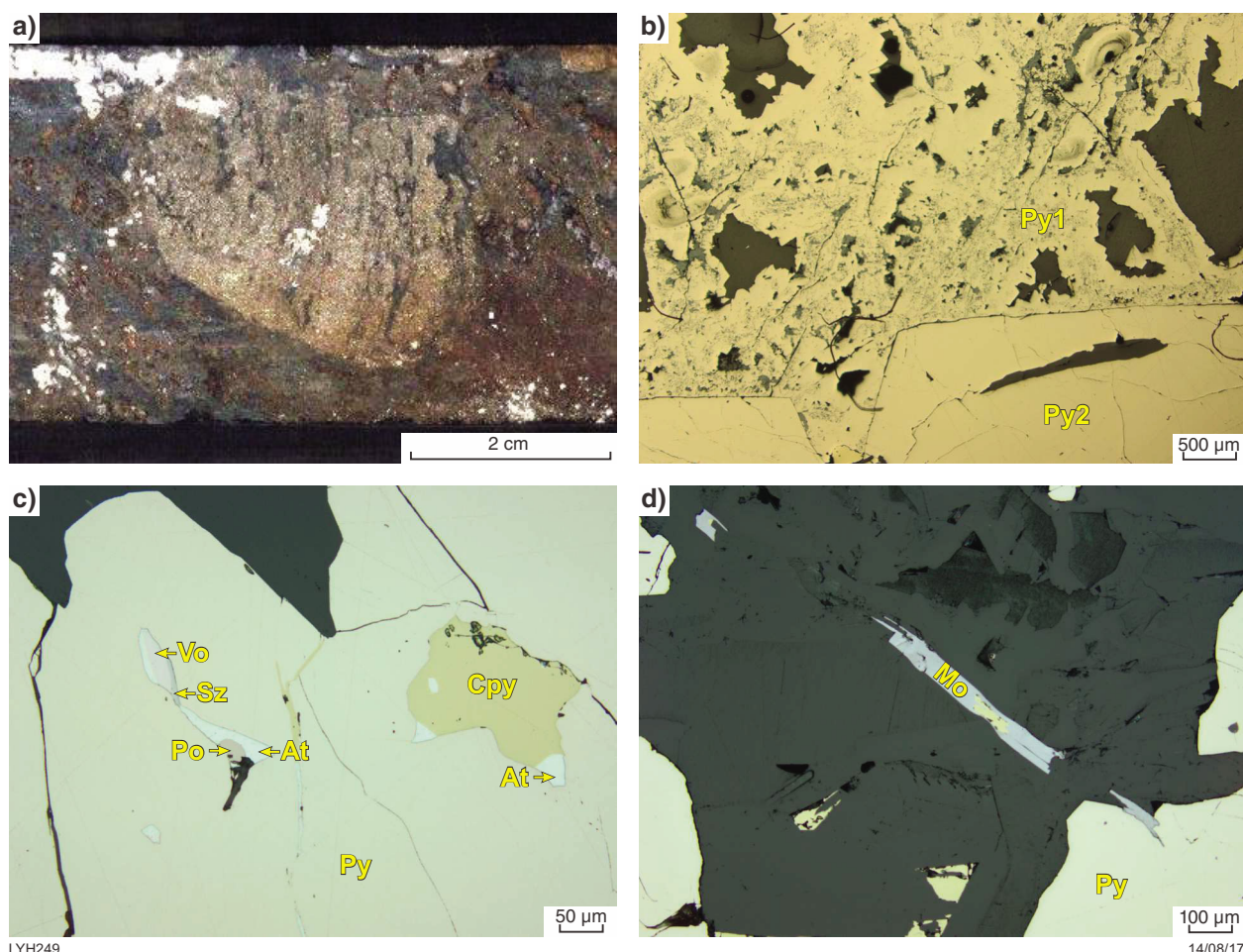


Figure 15. Sulfides from breccia: a) fragment of massive pyrite in breccia (GSWA 204797 from 127.8 m in 09ATD019); b) melnikovite pyrite (Py1) partially replaced by clear subhedral pyrite (Py2) from breccia in a), reflected light; c) inclusions of chalcopyrite (Cpy), pyrrhotite (Po) and tellurides including altaite (At) volynskite (Vo) and stützite (Sz) in clear pyrite (Py), from breccia in a), reflected light; d) flake of molybdenite (Mo) associated with pyrite, from breccia in a), reflected light

Semiquantitative SEM analyses of the talc (Table 3 – see zip file) indicate that the talc contains significant but variable amounts of FeO (3.7 – 13.0%) with the highest FeO value in the footwall schist of the high-grade zinc mineralization in 09ATD019 (Analysis 18, Table 3).

Ca-poor amphiboles

Anthophyllite is abundant in the footwall of the lowermost mineralized zones in 09ATD019 and 09ATD15 and is also associated with BIF adjacent to the mineralized zone in ATD101. The anthophyllite occurs as fine-grained acicular needles in BIF, generally parallel to bedding (Fig. 10b,c) but sometimes crosscutting it (Fig. 10d) and as coarser acicular crystals in intensely altered rock (Fig. 16b). In places, anthophyllite replaces earlier cummingtonite (Fig. 16b,c). The anthophyllite is distinguished from the cummingtonite by the straight extinction and lack of twinning in the anthophyllite and the inclined extinction and lamellar twinning in the cummingtonite. Both cummingtonite and anthophyllite are replaced by talc (Fig. 16b,c).

A spectral match on an absorption feature at 980 nm in the HyLogger data using the 'PFIT' feature of TSG was previously found to give a good indication of the presence of Ca-poor amphiboles at the Yuinmery VMS Prospects (Hassan, 2014). The spectral match was found to also give a good indication of the distribution of Ca-poor amphiboles at Austin in 09ATD019 (Fig. 5f), 09ATD15 (Fig. 6f) and ATD101 (Fig. 8f). In this latter drillhole, there is also an absorption feature at 980 nm in the weathered rock at the start of the drillhole which is probably related to iron oxides. In 09ATD025, there is an absorption feature at 980 nm associated with the mineralization and BIF but there is also an anomalous result in the upper part of the gabbro.

Semiquantitative SEM analyses of anthophyllite are given in Table 4 (see zip file). The Mg# varies from 0.50 to 0.75 with the samples from 09ATD015 having a higher Mg# and more Al_2O_3 than those from 09ATD019 and ATD101. Cummingtonite from two samples was analysed by SEM and one of the samples was also analysed by electron microprobe analysis. Results are given in Table 5.

Table 5. SEM and electron microprobe (Probe) analyses of Cumingtonite from Austin

Analysis	1	2	3	4	5	6	7	8	9	10	11	12	13	14	15	16
Sample	208150	208150	208150	208150	208150	208150	204753	204753	204753	204753	204753	204753	204753	204753	204753	204753
Method	SEM	SEM	SEM	SEM	SEM	SEM	SEM	SEM	SEM	SEM	SEM	Probe	Probe	Probe	Probe	Probe
Drillhole	ATD101	ATD101	ATD101	ATD101	ATD101	ATD101	09ATD015	09ATD015	09ATD015	09ATD015	09ATD015	09ATD015	09ATD015	09ATD015	09ATD015	09ATD015
Depth	453.6	453.6	453.6	453.6	453.6	453.6	262.3	262.3	262.3	262.3	262.3	262.3	262.3	262.3	262.3	262.3
SiO ₂	52.96	53.66	54.06	57.12	58.72	55.41	56.59	57.75	57.05	56.14	55.63	54.41	54.24	54.07	55.97	55.75
MgO	18.33	18.83	16.04	19.66	22.48	19.11	20.18	22.09	20.78	20.99	19.67	19.39	19.30	18.96	20.87	20.55
FeO	25.31	24.08	29.15	22.49	17.37	25.47	21.92	18.60	21.18	21.29	23.72	21.14	20.51	21.27	16.87	18.22
Al ₂ O ₃	0.76	1.00	–	–	1.42	–	1.32	1.56	0.99	1.58	0.98	1.13	1.32	1.27	1.29	1.20
CaO	0.75	0.57	0.75	0.73	–	–	–	–	–	–	–	0.09	0.04	0.12	0.05	0.07
TiO ₂	0.08	0.05	–	–	–	–	–	–	–	–	–	0.01	<0.01	0.02	0.03	0.02
MnO	0.26	0.08	–	–	–	–	–	–	–	–	–	0.15	0.11	0.10	0.11	0.06
K ₂ O	<0.01	<0.01	–	–	–	–	–	–	–	–	–	<0.01	<0.01	0.01	0.01	<0.01
Na ₂ O	0.31	0.41	–	–	–	–	–	–	–	–	–	0.14	0.16	0.16	0.22	0.20
P ₂ O ₅	<0.01	0.01	–	–	–	–	–	–	–	–	–	–	–	–	–	–
V	<0.01	0.01	–	–	–	–	–	–	–	–	–	–	–	–	–	–
SO ₃	0.11	0.26	–	–	–	–	–	–	–	–	–	–	–	–	–	–
Co	0.33	0.41	–	–	–	–	–	–	–	–	–	–	–	–	–	–
Cu	0.19	0.15	–	–	–	–	–	–	–	–	–	–	–	–	–	–
Cr ₂ O ₃	0.06	0.03	–	–	–	–	–	–	–	–	–	<0.01	<0.01	<0.01	<0.01	<0.01
NiO	0.13	0.08	–	–	–	–	–	–	–	–	–	–	–	–	–	–
ZnO	0.40	0.36	–	–	–	–	–	–	–	–	–	–	–	–	–	–
Total	100.00	100.00	100.00	100.00	100.00	100.00	100.00	100.00	100.00	100.00	100.00	96.45	95.68	95.98	95.42	96.06
Mg#	0.56	0.58	0.50	0.61	0.70	0.57	0.62	0.68	0.64	0.64	0.60	0.62	0.63	0.61	0.69	0.67

NOTE: – not analysed or below detection

The Mg# varies from 0.50 to 0.73, similar to the range obtained for the anthophyllite, and there is good agreement between the SEM and electron microprobe analyses.

Ca-rich amphiboles

According to the SWIR summary plots for 09ATD019, 09ATD15, 09ATD25 and ATD101 hornblende and actinolite are associated with mineralization (Figs 5a, 6a, 7a, and 8a) as well as with mafic intrusions or basalt. In the upper, copper-bearing zone in 09ATD19, hornblende replaces talc and chlorite and also crosscuts these minerals (Fig. 16d). Despite the fact that the HyLogger shows significant hornblende and actinolite beneath the lower, high-grade zinc mineralization in 09ATD019 (Fig. 5a), petrographic examination indicated that anthophyllite and cummingtonite were the dominant amphiboles, and no hornblende was observed in the sections taken within 10 m of mineralization. However, in a section from 16 m below mineralization, scattered zoned actinolite crystals were observed crosscutting foliation defined by chlorite and anthophyllite (Fig. 16e). Minor hornblende is associated with the lower-grade zinc mineralization in 09ATD015 and appears to have been partially replaced by sulfides (Fig. 16f).

Semiquantitative SEM analyses of the hornblende and actinolite are given in Table 6 and these confirm their identity.

Chlorite

Chlorite is the main alteration mineral distal to mineralization at Austin. Some schists are composed almost entirely of chlorite (Fig. 17a), whereas others consist of a mix of chlorite, white mica and quartz (Fig. 17b), or in places contain large crystals of plagioclase (Fig. 17c). Chlorite remains the dominant alteration mineral in the felsic schist 60 m below mineralization in WPD019 (Fig. 9e). Chlorite tends to be replaced by talc closer to mineralization (Fig. 16d) but rare remnant chlorite remains within the mineralized zone (Fig. 16b).

For 09ATD019, the plot of the wavelength of the chlorite 2250 absorption feature vs depth (Fig. 5g) suggests significant variation in the composition of the chlorite from Mg rich to Fe rich. The most Mg-rich chlorite is in the amphibole–talc schist and chlorite schist in the hangingwall of the upper mineralized zone and the most Fe-rich chlorite is in the footwall of the lowermost mineralization intersected. Chlorite is very sparse in the lower mineralized zone but more abundant in the upper mineralized zone where the HyLogger data suggest that the chlorite varies from Mg rich to moderately Fe rich. The HyLogger data also suggest that the felsic schist in the upper part of the drillhole is significantly more iron rich than that in the lower part of the drillhole, and that the rocks logged as basalt in the upper part of the hole have relatively Mg-rich chlorite.

The plot of the chlorite 2250 absorption feature vs depth for 09ATD015 (Fig. 6g) generally shows the same patterns as those for 09ATD019, with more Mg-rich chlorite in

amphibole–talc schist in the hangingwall of the upper mineralized zone, variable values in the mineralized zone, and felsic rock in the upper part of the hole that is more Fe rich than that in the lower part of the hole. However, the HyLogger data suggest that there are zones of different chlorite composition within the felsic rock beneath the mineralized zone. The dolerite intersected in 09ATD015 appears to have relatively Fe-rich chlorite.

In 09ATD025, mafic intrusions significantly disrupt the stratigraphy. The chlorite in the mafic intrusions appears to vary from Mg rich in the gabbro beneath mineralization to more Fe rich elsewhere in the drillhole (Fig. 7g). The chlorite in the felsic rock between the uppermost mineralization and the gabbro is very Fe rich as indicated by its anomalous blue interference colours (Fig. 17b), the plot of chlorite wavelength vs depth (Fig. 7g), and the summary SWIR plot (Fig. 7a).

For ATD101, the plot of the wavelength of the chlorite 2250 absorption feature vs depth (Fig. 8g) suggests a trend from chlorite with moderate Mg levels in the felsic schist beneath mineralization to Fe-rich chlorite in the porphyritic rhyolite near the end of the drillhole. The felsic schist above the BIF also appears to be Fe rich, whereas the chlorite in the amphibole–talc schist appears to be more Mg rich.

SEM analyses of the chlorite were carried out to verify the trends in composition suggested by the HyLogger. Results are given in Table 7 (see zip file). The variation in composition is less than that suggested by the HyLogger with most chlorites having a Mg# between 0.4 and 0.7. However, the general trends are similar and the most Mg-rich chlorite with a Mg# of 0.82 (analyses 1 and 2, Table 7) was where the HyLogger showed Mg-rich chlorite in the hangingwall of the uppermost zone of mineralization at 104.0 m in 09ATD019.

White mica

White mica is common in the felsic rocks distal to mineralization (Fig. 9f) but was almost totally absent in proximity to mineralization (Figs 5h, 6h, 7h, 8h) with the exception being a zone of later silicification and quartz veining between 144.1 and 147.6 m in 09ATD019 (Fig. 5h).

The plots of the wavelength of the white mica 2200 absorption feature vs depth (Figs 5g, 6g, 7g, 8g), suggest that the white mica is mainly paragonite to muscovite in composition, although in ATD101 white mica in a quartz vein at 394 m approaches phengite in composition (Fig. 8h) as does mica associated with thin veinlets in basalt at 84.1 m in 09ATD019 (Fig. 5h). In ATD101, there appears to be a trend from paragonitic mica in the felsic schist beneath the mineralization to muscovite in the rhyolite deeper in the drillcore, but this trend is not obvious in the other drillholes.

Semiquantitative SEM analyses of white mica from felsic rocks above and below mineralization in ATD101 (Table 8 – see zip file) indicated that the micas analysed were all muscovite, but there was some replacement of K by Na (i.e. a tendency towards paragonite) and possibly

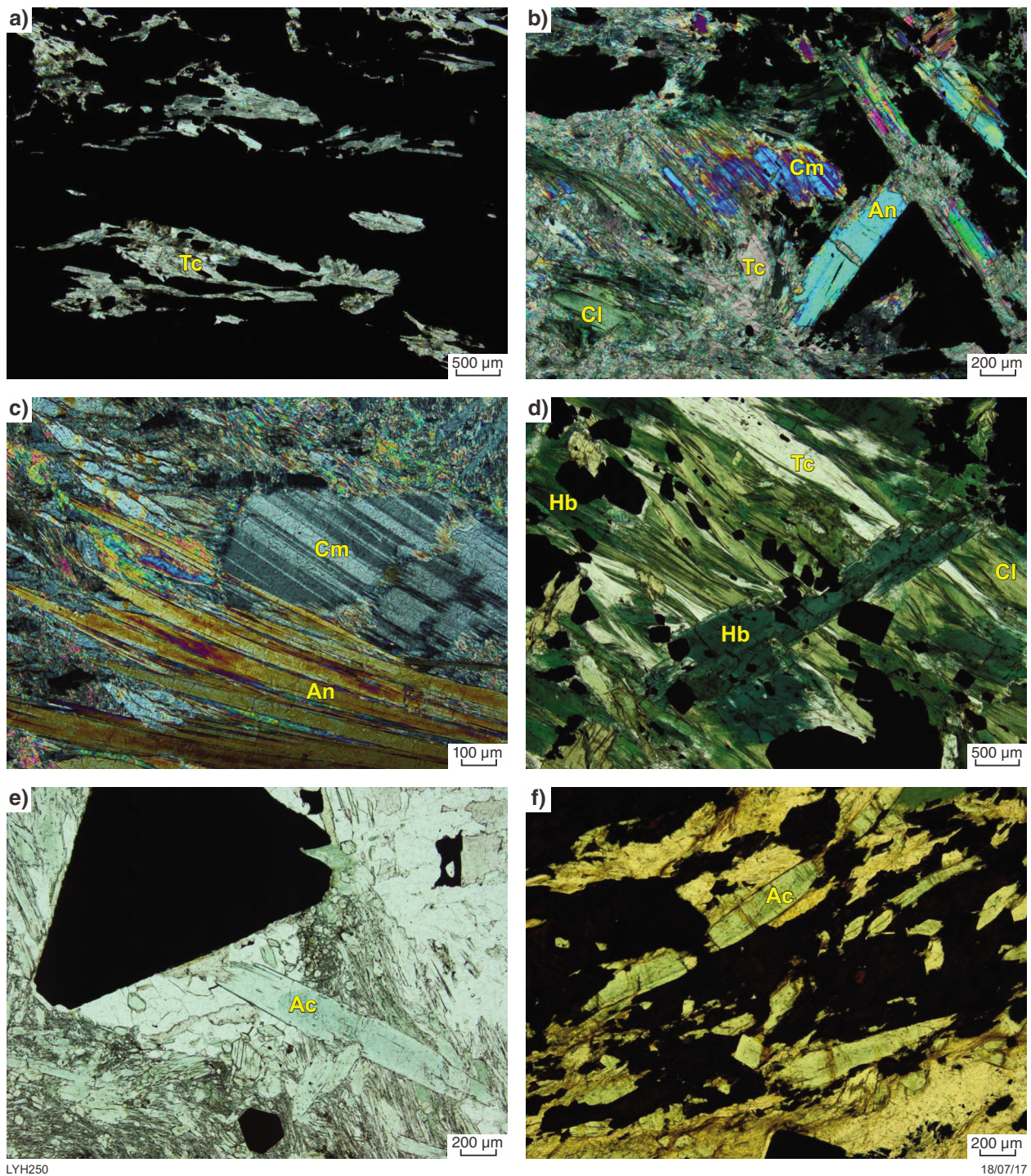
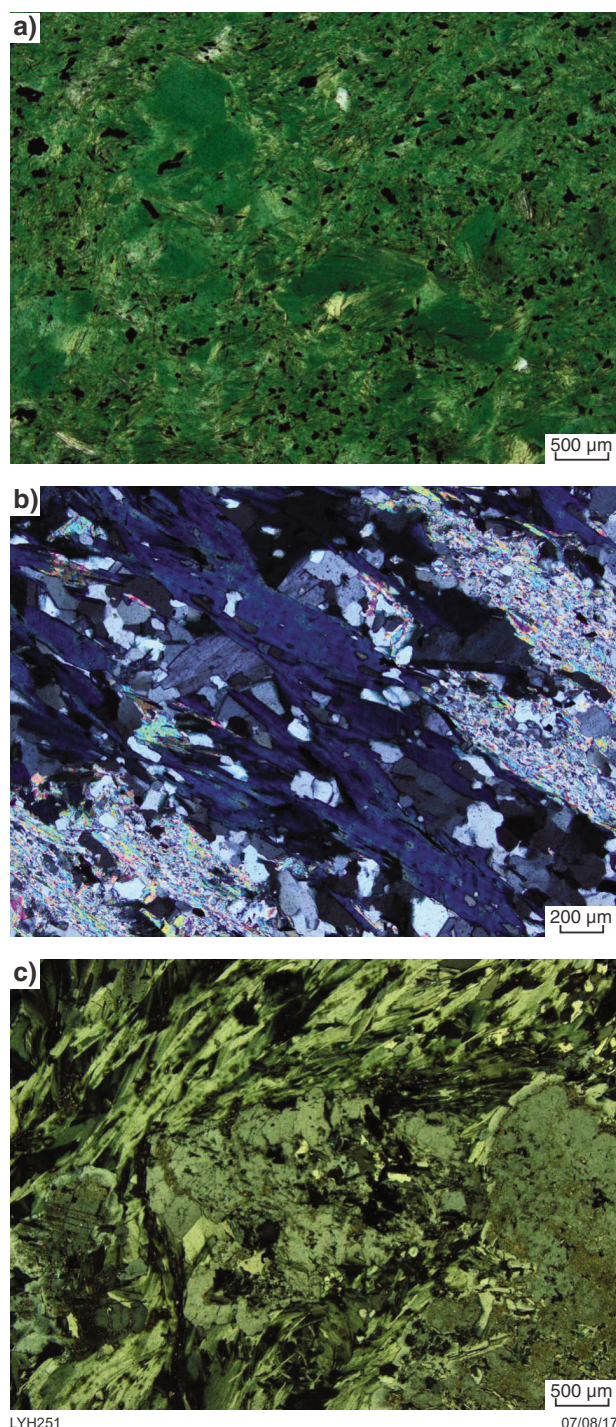


Figure 16. Alteration minerals at Austin: a) talc (Tc) in high-grade zinc ore (GSWA 204905 from 167.9 m in 09ATD019), crossed polars; b) talc replacing chlorite (Cl), anthophyllite (An) and cummingtonite (Cm) (GSWA 204907 from 172.6 m in 09ATD019), crossed polars; c) anthophyllite replacing cummingtonite (GSWA 204753 from 262.3 m in 09ATD015), crossed polars; d) talc replacing chlorite, hornblende (Hb) replacing chlorite and crosscutting chlorite and talc (GSWA 204791 from 112.0 m in 09ATD019), plane-polarized light; e) zoned actinolite (Ac) crosscutting foliation defined by chlorite and anthophyllite, and also the pressure shadow formed around pyrite (Py) (GSWA 204910 from 188.0 m in 09ATD019), plane-polarized light; f) actinolite (Ac) partially replaced by sulfides in low-grade zinc mineralization (GSWA 204791 from 238.2 m in 09ATD015), plane-polarized light

Table 6. SEM analyses of Ca-amphiboles from Austin

Analysis	1	2	3	4	5	6	7	8	9	10	11	12	13	14	15
Spectrum	204791	204791	204791	204791	204792	204792	204792	204792	204792	204792	204792	204792	204792	204910	204910
Drillhole	09ATD19	09ATD19	09ATD19	09ATD19	09ATD19	09ATD19	09ATD19	09ATD19	09ATD19	09ATD19	09ATD19	09ATD19	09ATD19	09ATD19	09ATD19
Depth (m)	112.0	112.0	112.0	112.0	115.1	115.1	115.1	115.1	115.1	115.1	115.1	115.1	115.1	188.0	188
Mineral	Hornblende	Hornblende	Hornblende	Hornblende	Hornblende	Hornblende	Hornblende	Hornblende	Hornblende	Actinolite/ tremolite	Actinolite/ tremolite	Actinolite/ tremolite	Actinolite/ tremolite	Actinolite/ tremolite	Actinolite/ tremolite
SiO ₂	51.42	50.58	51.19	51.22	48.97	49.47	49.51	49.50	49.68	53.66	53.44	53.65	51.23	56.77	54.82
MgO	18.67	17.01	17.22	17.37	15.92	16.63	15.85	16.24	16.29	18.82	19.18	19.21	17.03	17.57	16.87
FeO	11.00	12.28	12.14	12.09	12.79	12.36	12.48	12.37	11.59	11.16	11.24	10.98	12.56	10.10	11.28
Al ₂ O ₃	6.73	7.24	6.91	6.85	9.12	8.14	8.97	8.66	8.67	3.72	3.65	3.80	6.71	3.14	3.88
CaO	10.77	11.31	11.13	11.02	11.52	11.76	11.46	11.45	11.93	11.69	11.70	11.66	11.11	11.53	12.31
TiO ₂	–	–	–	–	–	–	–	–	–	–	–	–	–	–	–
MnO	–	–	–	–	–	–	–	–	–	–	–	–	–	–	–
K ₂ O	–	–	–	–	–	–	–	–	–	–	–	–	–	–	–
Na ₂ O	1.42	1.58	1.40	1.45	1.68	1.65	1.73	1.77	1.84	0.95	0.79	0.71	1.37	0.88	0.84
Mg#	0.80	0.76	0.77	0.77	0.74	0.76	0.75	0.75	0.76	0.79	0.80	0.80	0.76	0.80	0.77

NOTE: – not analysed or below detection



LYH251

07/08/17

Figure 17. Distal alteration at Austin: a) schist composed almost entirely of chlorite with minor disseminated fine-grained oxides (GSWA 204794 from 119.9 m in 09ATD019), plane-polarized light; b) schist composed of iron-rich chlorite with anomalous blue interference colours, white mica and quartz (GSWA 204768 from 137.8 m in 09ATD025), crossed polars; c) plagioclase (Pl) in chlorite schist (GSWA 204743 from 174.7 m in 09ATD015), crossed polars

of Al by Mg and Fe (i.e. a tendency towards phengite or aluminoceladonite) but backscatter from adjacent chlorite may have contributed Fe and Mg in some cases.

Plagioclase

Large crystals of plagioclase were observed in chlorite schist (Fig. 17c). As these are much larger than the remnant phenocrysts observed in the felsic rocks, it is likely that the plagioclase is an alteration mineral. SEM analysis of the example shown in Figure 17c gave 22.3% Al_2O_3 , 64.9% SiO_2 , 8.5% Na_2O and 4.3% CaO indicating that it is oligoclase.

Phosphates

Scattered crystals of apatite were observed in many of the altered rocks in the vicinity of mineralization. Most of the apatite is anhedral (Fig. 18a,b) but some apatite occurs as euhedral crystals (Fig. 11d). SEM analysis indicates that the apatite contains up to 5.59% fluorine (Analyses 1–14, Table 9). In one section, the Mg-phosphate wagnerite was associated with apatite (Fig. 18b) and its identity was confirmed by SEM analysis (Analyses 15–16, Table 8). A small grain of an unknown mineral, which SEM analysis suggests is a Y–Gd phosphate, was also found (Fig. 18c; Analysis 17, Table 9).

Epidote group minerals

Epidote is present as an alteration or metamorphic product in many of the mafic intrusions. It was also observed as an alteration product in a rock interpreted as a mafic tuff from 364.2 m in ATD101 (Fig. 19a). Semiquantitative SEM analyses are given in Table 10 (Analyses 1–3). Crystals of allanite, the rare earth element bearing member of the group, were observed crosscutting hornblende, chlorite and talc in schist within the upper mineralized zone in 09ATD019 and its identity confirmed by semiquantitative SEM analysis (Fig. 19b; Analyses 4–5, Table 10).

Carbonate

Carbonate is rare to absent in the mineralized zone and surrounding rocks except in minor late-stage quartz–carbonate veinlets.

Aluminium silicates

Vearncombe (2011) reported sillimanite in the interval 427.6 – 441.5 m in ATD101 but SEM analyses of numerous fibrous grains from this interval found no grains with high aluminium content. The fibrous mineral was actually anthophyllite (see Table 4). No sillimanite, kyanite or andalusite was identified in any of the thin sections from Austin, but these minerals were found in thin sections from the Franklin Prospect (see below).

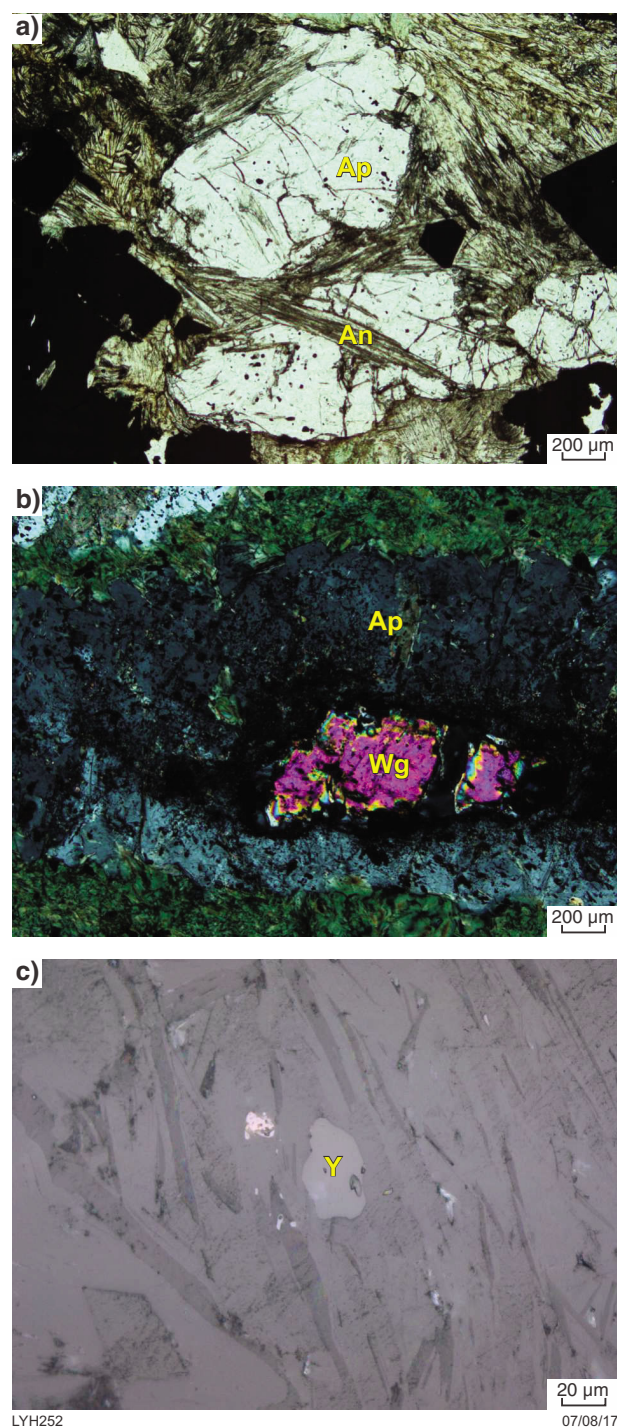


Figure 18. Phosphate minerals at Austin: a) anhedral apatite (Ap) partially replaced by anthophyllite (An) in schist with disseminated pyrite beneath the lowest mineralized horizon (GSWA 204908 from 178.5 m in 09ATD019), plane-polarized light; b) wagnerite (Wg) associated with apatite (GSWA 204794 from 119.9 m in 09ATD019), crossed polars; c) small grain of a Y-Gd phosphate (Y) in talc-chlorite schist (GSWA 204901 from 153.2 m in 09ATD019), reflected light

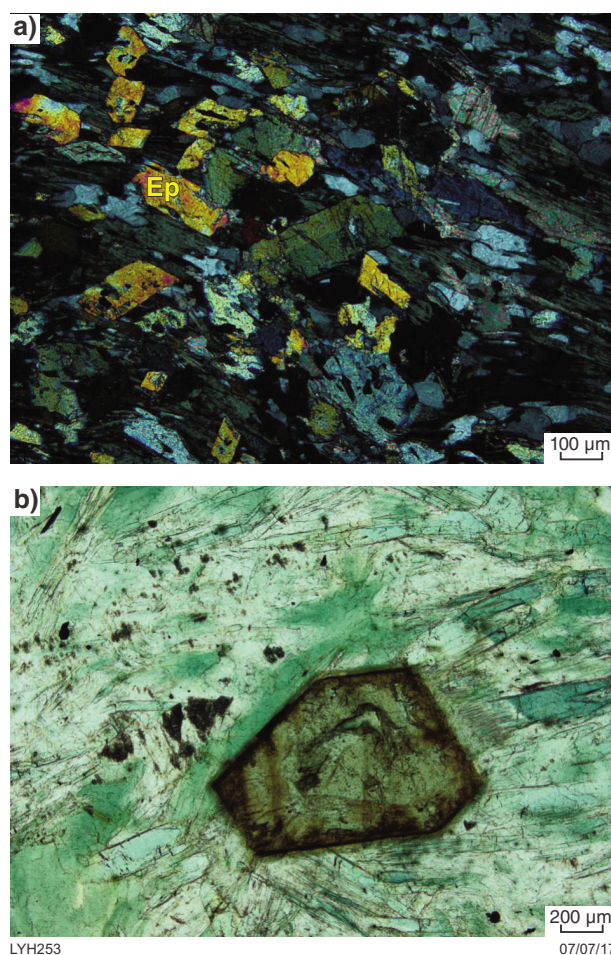


Figure 19. Epidote minerals at Austin: a) epidote (Ep) in ?mafic tuff (GSWA 208139 from 238.2 m in 09ATD015), plane-polarized light; b) allanite crosscutting hornblende, chlorite and talc in schist within the upper mineralized zone (GSWA 204792 from 115.1 m in 09ATD019), plane-polarized light

Table 9. SEM analyses of phosphates from Austin

Analysis	1	2	3	4	5	6	7	8	9	10	11	12	13	14	15	16	17
Sample	204747d	204747d	204753a	204753a	204792e	204792e	204792e	204793	204793	204794e	204794f	204795c	204908b	204908b	204794e	204794e	204901
Drillhole	09ATD15	09ATD15	09ATD015	09ATD015	09ATD19	09ATD19	09ATD19	09ATD19	09ATD19	09ATD019	09ATD015	09ATD015	09-ATD19	09-ATD19	09ATD015	09ATD019	09ATD019
Depth (m)	238.2	238.2	262.3	262.3	115.1	115.1	115.1	116.6	116.6	119.9	119.9	121.3	178.5	178.5	119.9	119.9	153.2
Mineral	Apatite	Apatite	Apatite	Apatite	Apatite	Apatite	Apatite	Apatite	Apatite	Apatite	Apatite	Apatite	Apatite	Apatite	Wagnerite	Wagnerite	Y-Gd phosphate
SiO ₂	1.68	1.28	2.95	3.76	1.33	1.83	4.40	0.94	1.10	–	–	–	1.72	1.77	–	–	18.21
MgO	–	–	0.92	1.23	–	–	2.17	0.51	0.69	0.85	–	–	–	–	41.50	41.92	13.27
FeO	1.14	1.45	1.90	2.46	0.80	0.81	1.57	1.20	0.66	–	–	–	1.00	1.53	6.59	6.78	12.82
Al ₂ O ₃	–	–	–	–	–	–	–	0.27	0.16	–	–	–	–	–	–	–	12.23
CaO	55.13	56.61	55.22	55.29	58.11	57.73	52.43	57.70	56.55	56.86	57.68	58.90	57.30	54.68	2.56	3.48	–
TiO ₂	–	–	–	–	–	–	–	<0.01	<0.01	–	–	–	–	–	–	–	–
MnO	–	–	–	–	–	–	–	0.03	0.01	–	–	–	–	–	–	–	–
K ₂ O	–	–	–	–	–	–	–	–	–	–	–	–	–	–	–	–	–
Na ₂ O	–	–	–	–	–	–	–	–	–	–	–	–	–	–	–	–	–
P ₂ O ₅	37.18	35.90	36.74	37.26	36.51	37.03	36.64	36.97	38.35	39.19	36.73	37.09	37.68	37.95	45.12	43.50	32.56
F	3.24	2.53	2.28	–	3.25	2.60	2.80	2.39	2.35	3.10	5.59	4.02	2.30	2.34	4.22	4.33	–
SO ₃	1.63	2.23	–	–	–	–	–	<0.01	0.12	–	–	–	–	1.73	–	–	–
Y ₂ O ₃	–	–	–	–	–	–	–	–	–	–	–	–	–	–	–	–	77.5
Gd ₂ O ₃	–	–	–	–	–	–	–	–	–	–	–	–	–	–	–	–	3.15

NOTE: – not analysed or below detection

Table 10. SEM analyses of epidote group minerals from Austin

<i>Analysis</i>	<i>1</i>	<i>2</i>	<i>3</i>	<i>4</i>	<i>5</i>
Sample	20813	20813	20813	204792	204792
Drillhole	ATD101	ATD101	ATD101	09ATD19	09ATD19
Depth (m)	364.2	364.2	364.2	115.1	115.1
Mineral	Epidote	Epidote	Epidote	Allanite	Allanite
SiO ₂	40.66	39.63	41.21	30.34	31.21
MgO	–	–	–	1.65	2.61
FeO	9.41	10.87	10.51	17.97	17.75
Al ₂ O ₃	25.37	23.55	22.87	14.37	15.30
CaO	24.56	25.96	25.41	15.35	14.86
TiO ₂	–	–	–	–	–
MnO	–	–	–	–	–
K ₂ O	–	–	–	–	–
Na ₂ O	–	–	–	–	–
P ₂ O ₅	–	–	–	–	–
Ce ₂ O ₃	–	–	–	9.23	8.37
Nd ₂ O ₃	–	–	–	5.62	4.90
La ₂ O ₃	–	–	–	5.47	4.99

NOTE: – not analysed or below detection

Robert Prospect

The Robert Prospect is an interpreted fold closure along strike from the Austin deposit (Fig. 4; Silver Swan Group, 2010b). Drillhole 09RTD001 was drilled to test the prospect. Minor sulfide mineralization was intersected in association with a siliceous horizon interpreted as an exhalite. A log for drillhole 09RTD001 is given in Appendix 1e (on the zip file) and is shown pictorially in Figure 20b.

Lithologies intersected

Felsic rocks

Porphyritic rhyolite, felsic schist with quartz aggregates, felsic schist and recrystallized felsic rocks similar to those intersected at Austin were intersected in 09RTD001. Felsic rocks with fragmental textures interpreted to have originated as lithic tuffs were also intersected. The fragments vary from >2 cm (Fig. 21a) to less than 5 mm (Fig. 21b).

Exhalite

A compositionally layered silica-rich rock with sulfides preferentially concentrated in thin layers (Fig. 22a,b) is interpreted to be an exhalite. Quartz is the dominant mineral. Some quartz-rich layers include wispy chlorite and white mica (Fig. 22b). In other layers, the quartz is crosscut by numerous fibrous crystals of anthophyllite (Fig. 22c) and is very similar to BIF in ATD101 at Austin (Fig. 10c). Fine-grained dusty magnetite is concentrated in some layers and coarser grained magnetite is also sparsely disseminated in places (Fig. 21d).

Mafic rocks

Fine- to medium-grained mafic rocks that could either be dolerite or basalt are present in the central part of 09RTD001. Some of these are foliated indicating that they were emplaced before deformation. There is a possible xenolith of felsic rock within the mafic rock between 250.9 and 251.2 m (Fig. 23) suggesting it is intrusive rather than extrusive. For this reason, all of the mafic rocks are shown as dolerite on the simplified log (Fig. 20b). However, the possibility that some of them are basalt cannot be ruled out.

Mineralization

The mineralization intersected in 09RTD001 at the Robert Prospect is subeconomic with the best intersection being 1 m at 0.2% Zn and 0.1% Cu between 120 and 121m. Pyrrhotite is the dominant sulfide and occurs as elongate grains parallel to the layering; minor chalcocopyrite is intergrown with the pyrrhotite in places, and some pyrite also occurs parallel to layering (Fig. 22a). Pyrite also occurs as euhedral to subhedral crystals and as crosscutting veinlets within the exhalite.

Alteration

A summary plot of SWIR data for drillhole 09RTD001 is given in Figure 20a where it can be compared with simplified lithology (Fig. 20b), Zn values (Fig. 20c), Cu values (Fig. 20d) weighted talc values (Fig. 20e), calcium-poor amphiboles as measured by the depth of the 980 nanometre wavelength feature (Fig. 20f), chlorite wavelength (Fig. 20g), and white mica wavelength (Fig. 20h).



LYH284

07/08/17

Figure 20. HyLogger, lithology and assay data for drillhole 09RTD001 from the Robert Prospect: a) SWIR summary plot; b) simplified lithology; c) Zn assays; d) Cu assays; e) weighted talc values; f) distribution of Ca-poor amphiboles on basis of the 980 absorption feature; g) chlorite wavelength; h) white mica wavelength

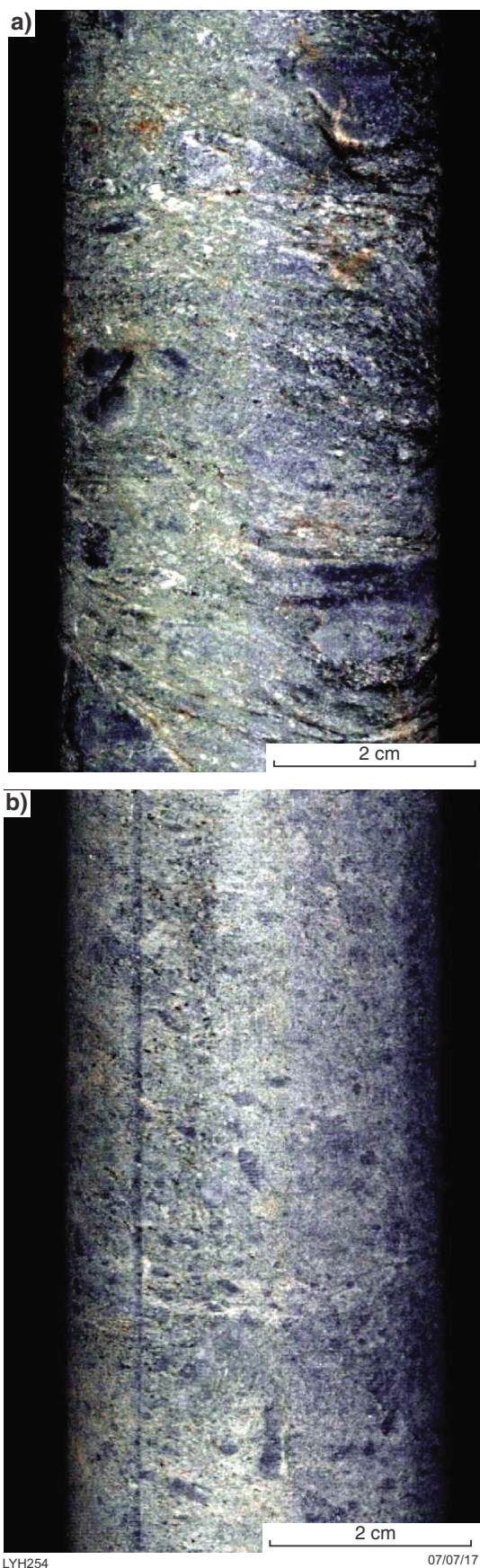


Figure 21. Lithic tuff at Robert Prospect: a) core with large fragments, some >2 cm (262.2 m in 09RTD001); b) core with fragments <5 mm (301.4 m in 09RTD001)

Talc was a very minor alteration product at the Robert Prospect compared with Austin. It was in too low a concentration to be recorded on the summary plot (Fig. 20b) and only 11 points are recorded on the weighted talc plot (Fig. 20e).

Anthophyllite is a significant alteration mineral in the exhalite as indicated by the amphibole 980 nm absorption feature (Fig. 20f) and was confirmed petrographically (Fig. 22c). Ca-amphiboles were not observed in the vicinity of the exhalite. All of the hornblende and actinolite detected by the HyLogger is in dolerite.

Chlorite is present throughout the length of the drillcore and is particularly abundant in the chlorite schists above and below the exhalite. According to HyLogger data (Fig. 20g), the chlorite in the chlorite schist on either side of the exhalite is moderately Mg rich but in the felsic schists structurally above, chlorite is even more Mg rich. The recrystallized felsic rock above the dolerite appears to have Fe-rich chlorite, and the chlorite in the felsic schist with quartz aggregates in the lower part of the drillhole is also moderately Fe rich. The less deformed, more recognizable rhyolite has chlorite that is moderately Mg rich on the basis of the 2250 nm wavelength feature.

White mica is absent in the exhalite, chlorite schist and felsic rocks within 15 m of the exhalite. The white mica in the felsic schist in the upper part of the drillhole is paragonitic, whereas in the felsic rocks in the lower part of the drillhole, the white mica is muscovite on the basis of the 2200 nm wavelength feature.

Epidote alteration is widespread in the matrix of the mafic rocks. Prehnite and carbonate occur in narrow veins within the mafic rocks.

Herbert Prospect

Diamond drillhole 09HBRCD001 was drilled to test a magnetic anomaly at the Herbert Prospect, 1.6 km north of Austin (Fig. 2). Only weakly anomalous base metal values were intersected in association with BIF. A log for drillhole 09RTD001 is given in Appendix 1f (on the zip file) and is shown pictorially in Figure 24b.

Lithologies intersected

Felsic rocks

Porphyritic rhyolite or rhyodacite with phenocrysts of plagioclase and quartz was the most common rock type intersected in drillhole 09HBRCD at the Herbert Prospect. Where least altered, the rhyolite contains moderately abundant biotite in the groundmass (Fig. 25a,b). Felsic schist with remnant quartz in a fine-grained matrix of quartz, feldspar and biotite or chlorite is probably a deformed version of the porphyritic rhyolite. Felsic schist without obvious remnant quartz phenocrysts is interpreted to be more strongly deformed rhyolite/rhyodacite or felsic tuff. The felsic schists are composed dominantly of fine-grained quartz and albite, and in places also contain chlorite and carbonate (Fig. 25c) or epidote and rare garnet (Fig. 25d).

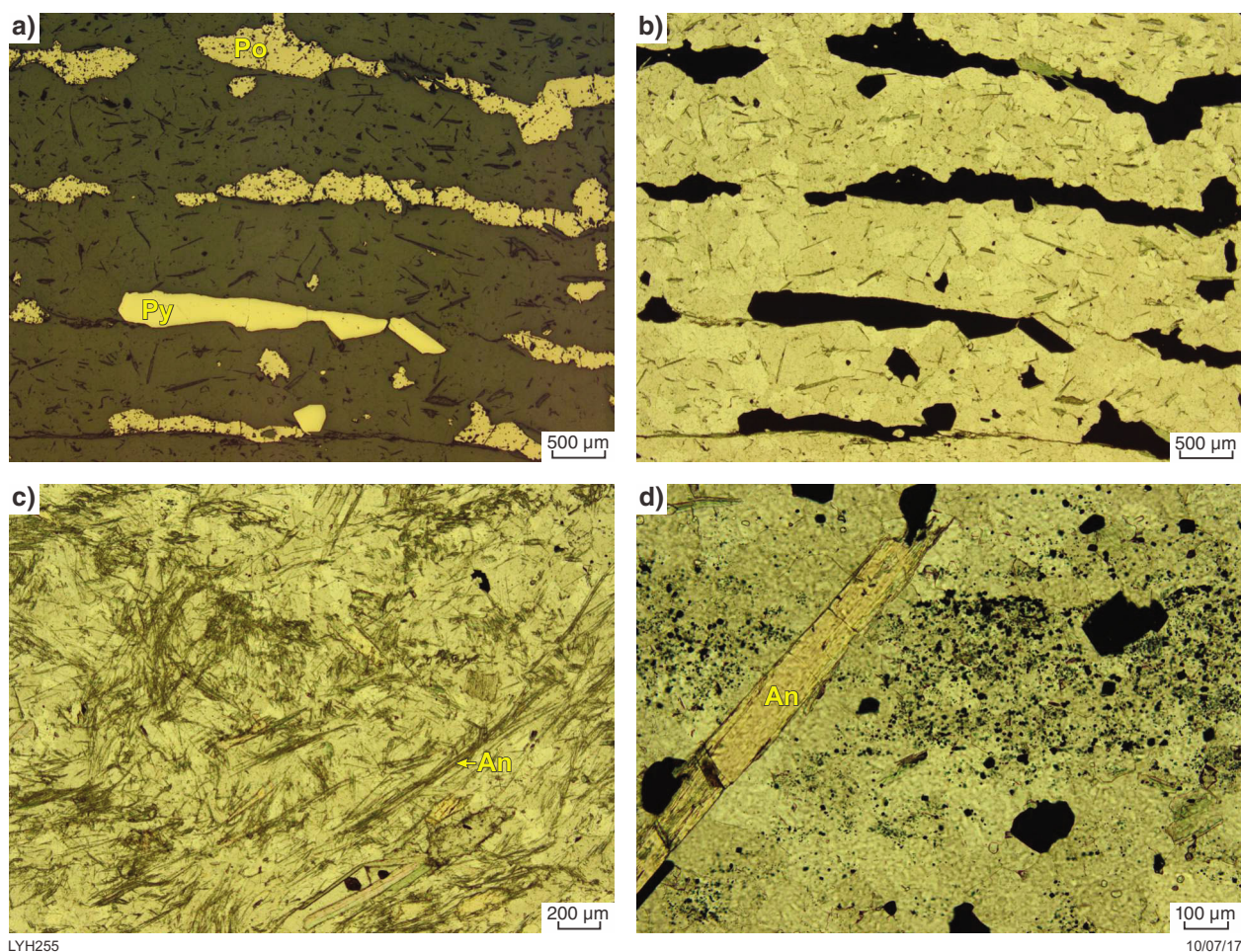


Figure 22. Exhalite at Robert Prospect: a) compositionally layered silica-rich rock with pyrrhotite (Po) and pyrite (Py) preferentially concentrated in thin layers (GSWA 204918 from 118.7 m in 09RTD001), reflected light; b) same view as a), plane-polarized light; c) silica-rich layer with numerous fibrous crystals of anthophyllite (An); d) silica-rich exhalite with layer of fine-grained dusty magnetite cut by crystal of An (GSWA 204919 from 122.1 m in 09RTD001)

Mafic rocks

Fine-grained mafic rocks intercalated with rhyolite and BIF at the Herbert Prospect in 09HBRCD001 are interpreted to be basalt as in places they have small oval-shaped areas filled with epidote that are probably amygdalae (Fig. 26a) and elsewhere are strongly foliated, indicating that they pre-date deformation (Fig. 26b). More massive, fine- to medium-grained mafic rocks were logged as dolerite but could also be basalt as no definite intrusive contacts were observed.

BIF

Three main horizons within 09HBRCD001 were logged as BIF. Included among the rocks logged as BIF are oxide-facies BIF with finely laminated magnetite alternating with silica-rich layers, and in places hornblende-rich laminae (Fig. 27a). There are also many thicker layers composed dominantly of hornblende that may be after silicate-facies BIF or mafic tuff. In places, the hornblende contains trails of fine-grained magnetite (Fig. 27b) indicating that it has crystallized later and perhaps replaced an earlier iron-

rich silicate or carbonate. Interbedded with the oxide and silicate-facies BIF are breccia zones up to 10 cm thick that contain fragments of BIF and chert in a matrix of quartz, chlorite, hornblende and magnetite (Fig. 27c); these are possibly pyroclastic or debris flow deposits.

Mineralization

Weakly disseminated sulfides are present in the BIF horizons. The best base metal intersection was 1 m at 903 ppm Zn and 376 ppm Cu at 293–294 m. Minor chalcopyrite and sphalerite were observed (Fig. 28).

Alteration

Neither talc nor Ca-poor amphiboles were observed at the Herbert Prospect. Hornblende is abundant in some of the BIF layers and may have formed as a result of metamorphism of earlier iron-rich silicates or replacement of early silicates or carbonate by hot fluids. Hornblende is also associated with epidote in quartz veinlets in



Figure 23. Xenolith of felsic rock in dolerite at the Robert Prospect (251 m in 09RTD001)

rhyolite (Fig. 25e); a few mm from the veinlet shown in Figure 25e, the textures of the rhyolite are well preserved although there is some replacement of biotite by Hb, and minor carbonate is present.

Chlorite is an abundant alteration product in the mafic rocks where the HyLogger shows it to be fairly Mg rich (Fig. 24d) but is much less abundant in the felsic rocks than at Austin. Where present in the felsic rocks, it is moderately to strongly Fe rich as indicated by the HyLogger (Fig. 24d) and petrographically by its dark-green colour (Fig. 25c).

White mica is also less abundant than at Austin. Where present, the HyLogger suggests that it is paragonitic in the mafic rocks and muscovite tending to phengite in the felsic rocks (Fig. 24e). Biotite is abundant in the felsic rocks (Figs 24f, 25b) and may be a primary mineral.

As at Austin, epidote is a significant alteration mineral in the mafic rocks but it is even more abundant in some of the felsic schists (Figs 24g, 25d). Garnet is a minor phase in felsic schist (Fig. 25d).

Franklin

Drillhole 09FKRCD001 at the Franklin Prospect 5.7 km northeast of the Austin deposit (Fig. 2) was drilled to test an aeromagnetic anomaly. It failed to intersect significant base metal mineralization or BIF but provided information on the rock types and mineralogy at this location distal from known mineralization. A log for drillhole 09FKRCD001 is given in Appendix 1g (on zip file) and is shown pictorially in Figure 29c. A summary TIR plot of mineral groups is given in Figure 29a and a summary SWIR plot of minerals is given in Figure 29b.

Lithologies intersected

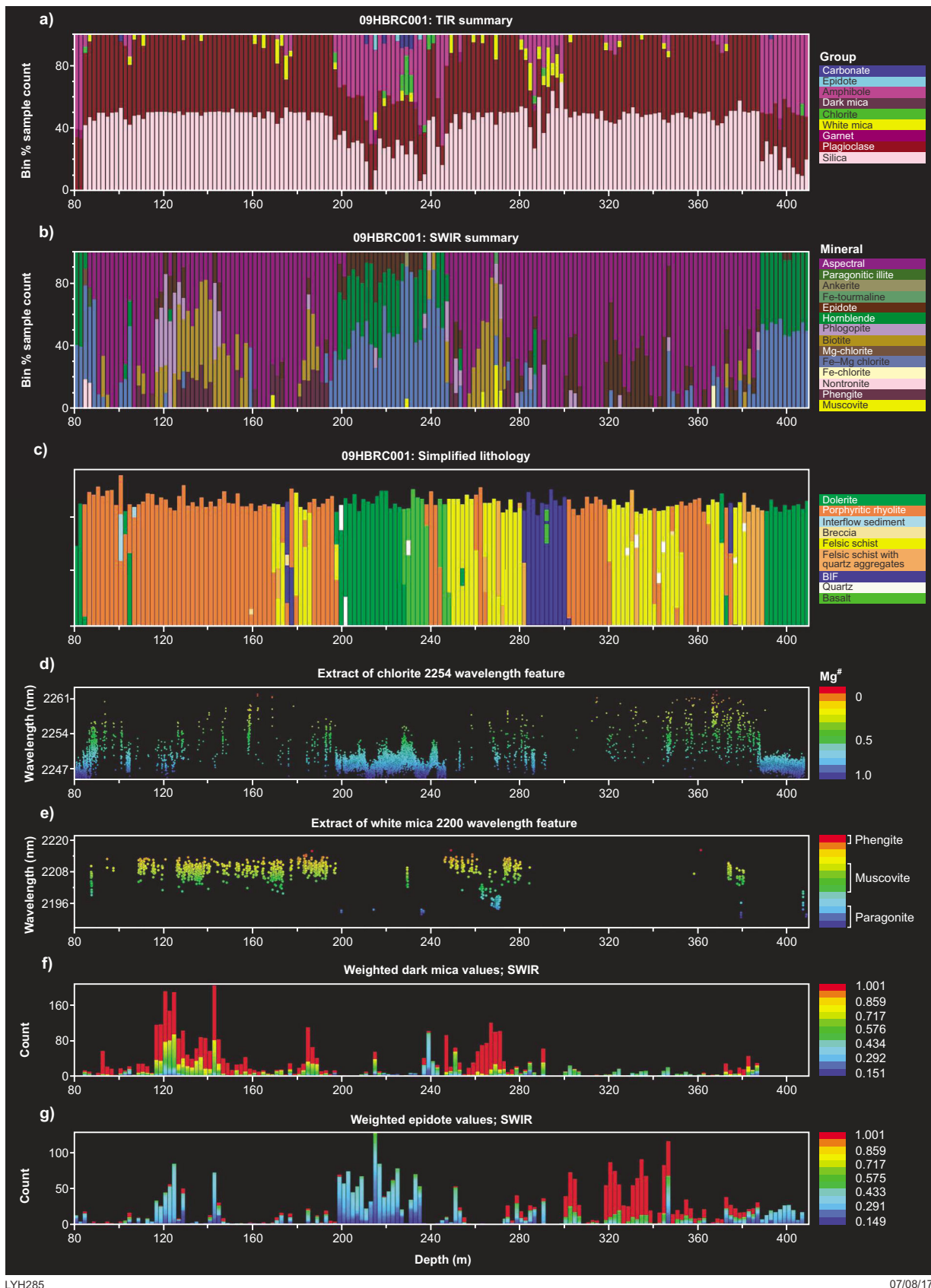
Schist

Variably foliated quartz–chlorite–white mica-rich rocks were intersected throughout drillhole 09FKRCD001 except where displaced by mafic intrusions. In addition to quartz, chlorite and white mica, all three aluminium silicate polymorphs are present in this drillhole. Andalusite mostly occurs as irregular patches up to 6 mm across all in optical continuity with and enclosing quartz grains (Fig. 30a). It appears to have selectively replaced very fine-grained chlorite and white mica interstitial to the quartz close to fracture zones, with the chlorite and white mica preserved farther from the fracture zones. Andalusite also occurs as coarser anhedral crystals (Fig. 30b). In one section, sillimanite was observed in contact with andalusite and appears to be growing at the expense of it (Fig. 30b). Kyanite is present as radiating aggregates of crystals in fracture zones (Fig. 30c) and as irregular anhedral grains, some of which display characteristic simple twinning in association with andalusite (Fig. 30d).

In places, gedrite is present as fibrous aggregates generally aligned parallel to schistosity (Fig. 30e). The gedrite appears to replace or have been replaced by a brown to dark bluish grey mineral or mineral aggregate (referred to in this Record as Phase x and described in more detail in the section on Alteration and metamorphic minerals). In places, Phase x is quite abundant and contributes to the apparent compositional layering of the rocks (Fig. 30f).

Foliation is generally weak and defined by chlorite, gedrite and Phase x. In more highly deformed rocks, quartz grains are also elongated (Fig. 30e) but in most of the schists, the quartz grains are equant (Fig. 30d).

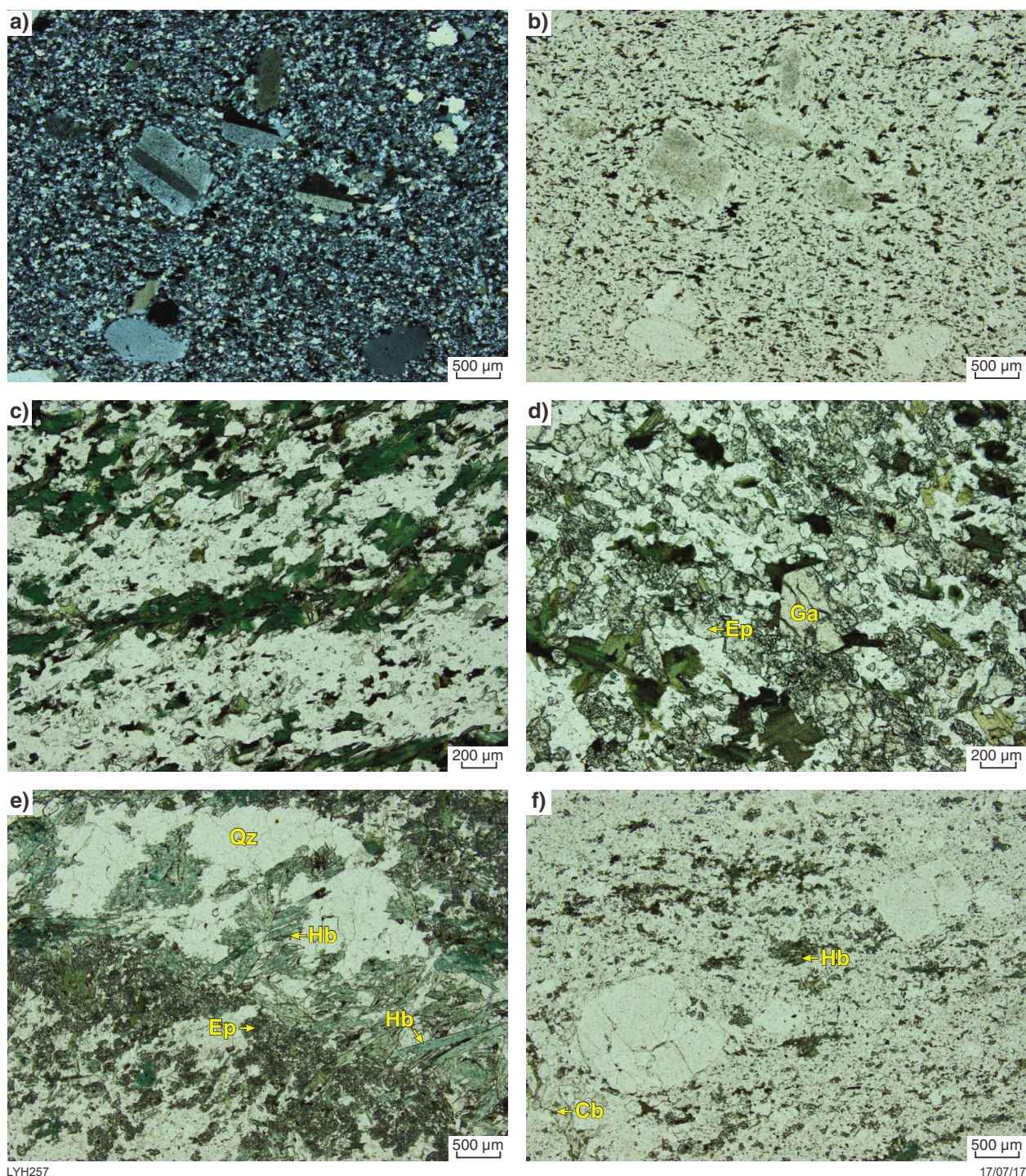
These rocks were interpreted as rhyolite by Wellman (2010) but differ significantly in texture and mineralogy from the porphyritic rhyolite and felsic schist with quartz aggregates intersected at the Austin and Herbert Prospects. It is possible that they were derived from felsic tuffs or nonporphyritic rhyolite if the fine-grained chlorite and white mica in the matrix between the quartz was originally feldspar. However, it is equally possible that they are metamorphosed argillic siltstones. Because of the uncertainty of the protolith, these rocks are simply shown as schist on Fig. 29c.



LYH285

07/08/17

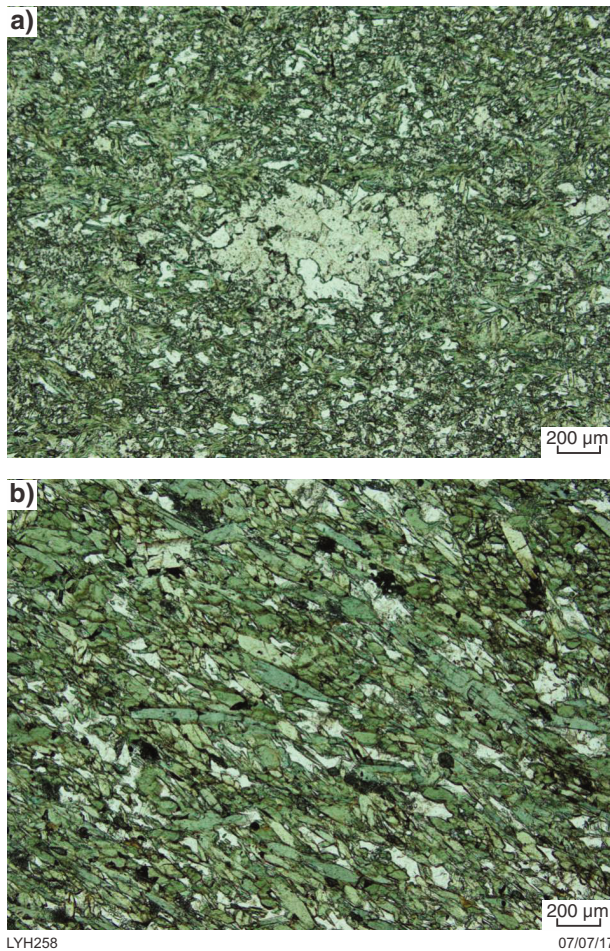
Figure 24. HyLogger, lithology and assay data for drillhole 09HBRC001 from the Herbert Prospect: a) TIR summary plot; b) SWIR summary plot; c) simplified lithology; d) chlorite wavelength; e) white mica wavelength; f) weighted dark mica values; g) weighted epidote values



LYH257

17/07/17

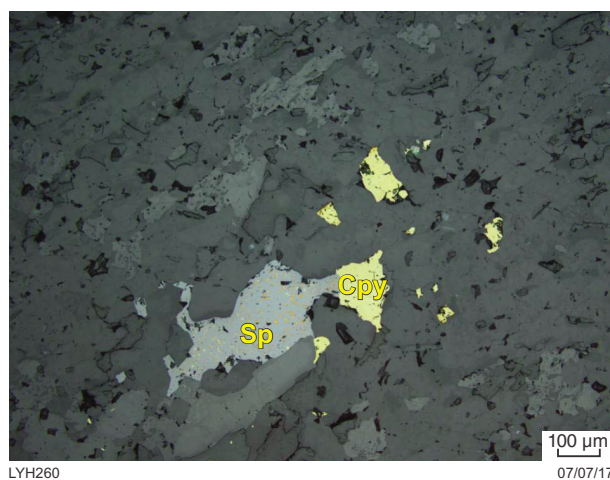
Figure 25. Felsic rocks from the Herbert Prospect: a) porphyritic rhyolite or rhyodacite with phenocrysts of plagioclase and quartz in a fine-grained matrix of quartz, feldspar and biotite (GSWA 208160 from 107.5 m in 09RTD001), crossed polars; b) same view as a), plane-polarized light; c) felsic schist composed of fine-grained quartz, albite, chlorite and minor carbonate (GSWA 206301 from 366.8 m in 09HBRD001), plane-polarized light; d) schist with abundant epidote (Ep) and minor garnet (Ga) (GSWA 208197 from 322.8 m in 09HBRD001), plane-polarized light; e) hornblende (Hb) and epidote (Ep) associated with thin quartz veinlet (GSWA 208160 from 124.8 m in 09HBRD001), plane-polarized light; f) porphyritic rhyolite a few millimetres from veinlet in e) with textures well preserved apart from replacement of biotite by hornblende and some carbonate (Cb) alteration



LYH258

07/07/17

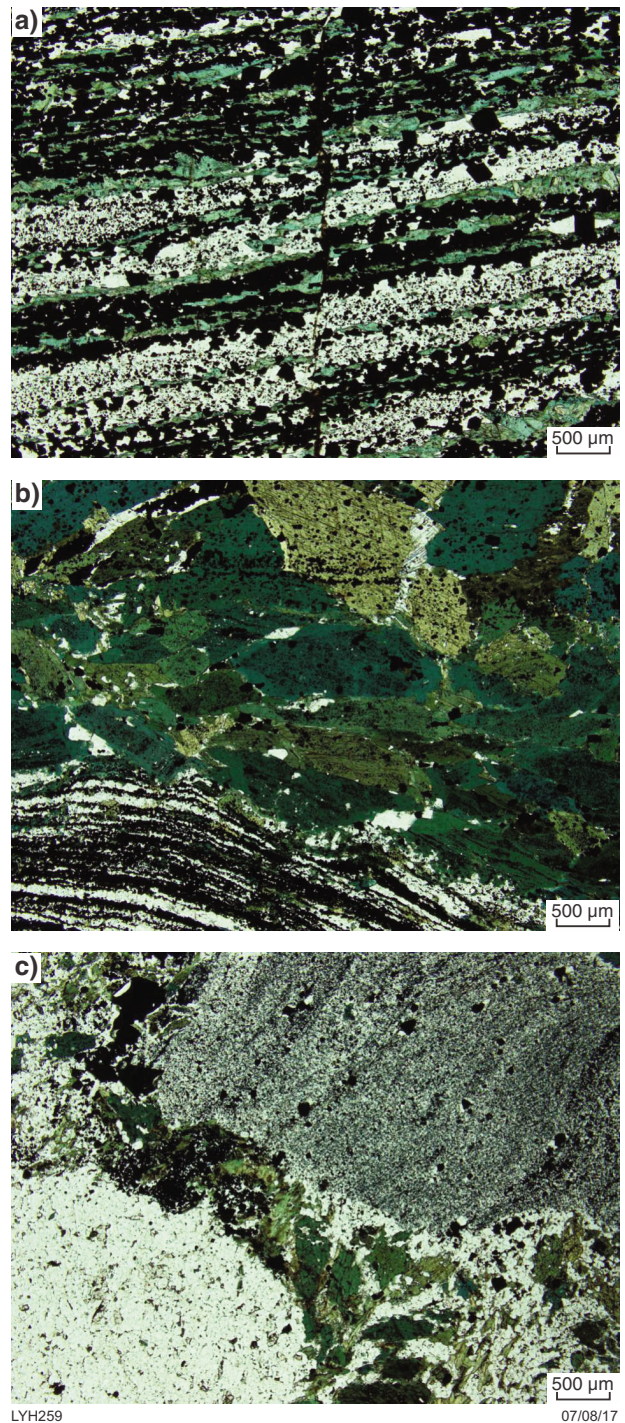
Figure 26. Basalt from the Herbert Prospect: a) basalt with epidote and quartz-filled amygdale (GSWA 208181 from 234.2 m in 09HBRD001), plane-polarized light; b) strongly foliated basalt with abundant hornblende (GSWA 208182 from 337.2 m in 09HBRD001), plane-polarized light



LYH260

07/07/17

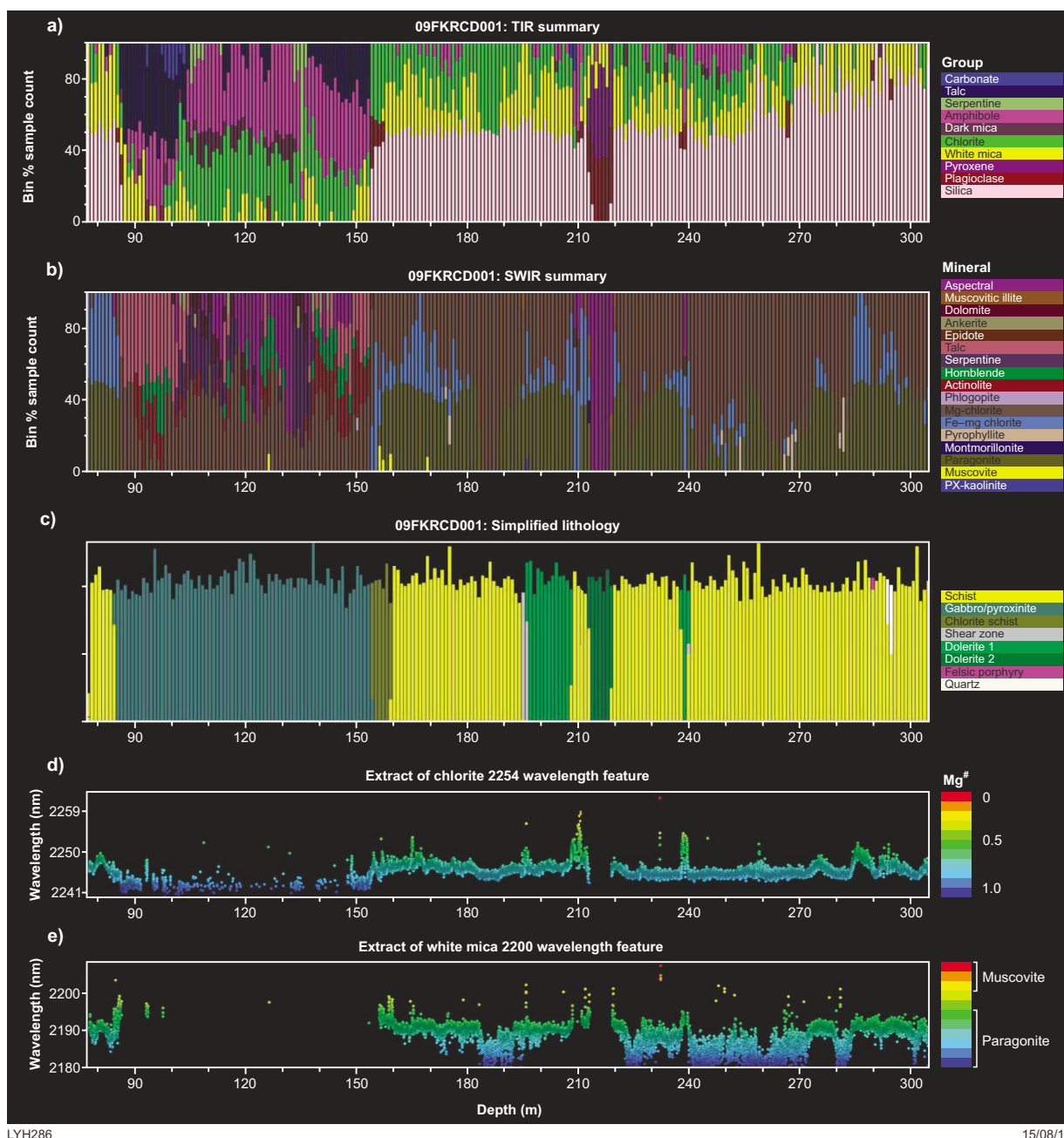
Figure 28. Sphalerite (Sp) and chalcopyrite (Cpy) in BIF from the Herbert Prospect (GSWA 208193 from 300.1 m in 09HBRD001), reflected light



LYH259

07/08/17

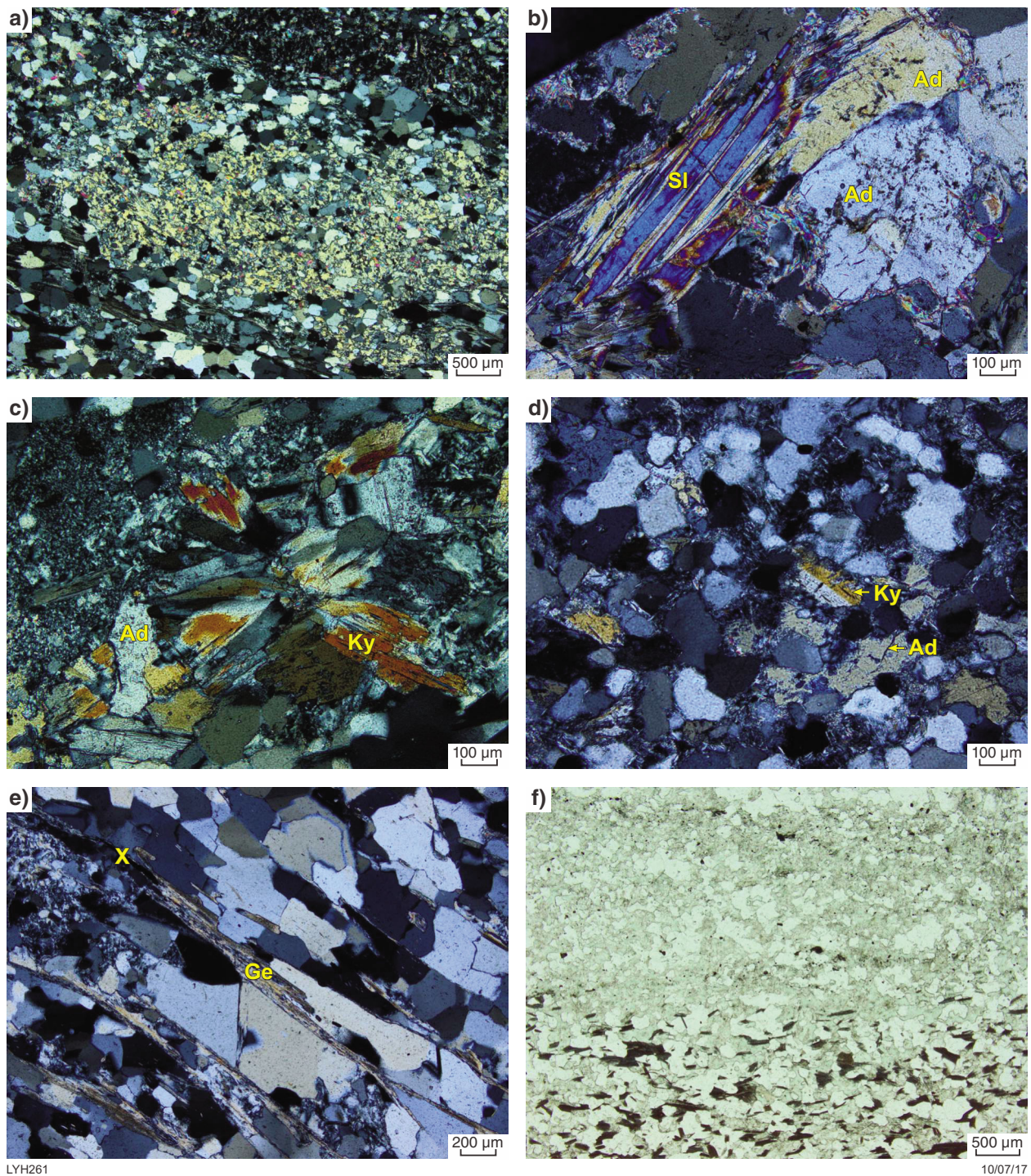
Figure 27. BIF from the Herbert Prospect: a) finely laminated BIF composed of quartz, hornblende and magnetite, cut by microfault (GSWA 208191 from 287.0 m in 09HBRD001), plane-polarized light; b) finely laminated BIF in contact with layer of coarse-grained hornblende containing trails of fine-grained magnetite (GSWA 208173 from 174.6 m in 09HBRD001), plane-polarized light; c) breccia composed of fragments of BIF and chert in a matrix of quartz, chlorite, hornblende and magnetite (GSWA 208188 from 281.4 m in 09HBRD001), plane-polarized light



LYH286

15/08/17

Figure 29. HyLogger, lithology and assay data for drillhole 09FKRCD001 from the Franklin Prospect: a) TIR summary plot; b) SWIR summary plot; c) simplified lithology; d) chlorite wavelength; e) white mica wavelength



LYH261

10/07/17

Figure 30. Alteration minerals at the Franklin Prospect: a) patch of andalusite (pale yellow) all in optical continuity and minor muscovite (bright colours) replacing fine-grained chlorite and white mica in matrix between quartz grains (GSWA 206311 from 169.1 m in 09FKRCD001), crossed polars; b) sillimanite (Si) replacing andalusite (Ad) (GSWA 206314 from 182.2 m in 09FKRCD001), crossed polars; c) radiating aggregate of kyanite crystals at edge of fracture, same sample as a), crossed polars; d) kyanite (Ky) associated with andalusite (Ad) (GSWA 206319 from 265.5 m in 09FKRCD001), crossed polars; e) fibrous gedrite (Ge) and Phase x (X) aligned parallel to schistosity (GSWA 206317 from 226.4 m in 09FKRCD001), crossed polars; f) compositionally layered rock; upper layer composed of quartz, white mica and pale-green chlorite; lower layer composed of quartz, pale-green chlorite and dark-brown Phase x (GSWA 206321 from 295.3 m in 09FKRCD001); plane-polarized light

Chlorite schist

Schist with chlorite dominating over quartz and containing abundant fine-grained ilmenite (Fig. 31) was logged as chlorite schist. It may have been derived from a mafic tuff given the abundance of ilmenite.

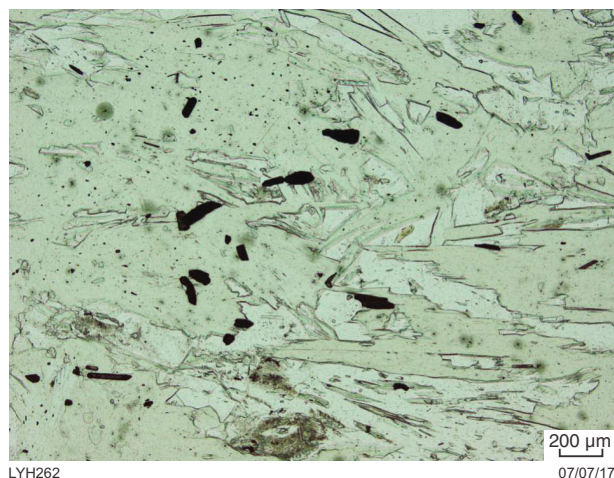


Figure 31. Chlorite schist with fine-grained ilmenite from the Franklin Prospect (GSWA 206308 from 155.6 m in 09FKRCD001), plane-polarized light

Gabbro–pyroxenite

A very altered rock consisting dominantly of talc, chlorite, amphiboles and serpentine with disseminated magnetite was intersected between 84.6 and 153.9 m. This was interpreted by Wellman (2010) as talc and magnetite-altered rhyolite but the presence of remnant pyroxenes partially replaced by talc, chlorite, and amphiboles (Fig. 32) indicates that it is an altered gabbro or pyroxenite.

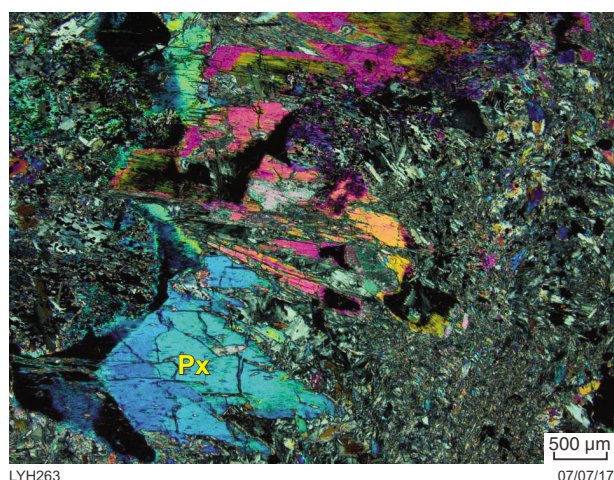


Figure 32. Remnant pyroxene (Px) in altered gabbro from the Franklin Prospect (GSWA 206307 from 140.8 m in 09FKRCD001), crossed polars

Dolerite

Two generations of dolerite were intersected by 09FKRCD001. The earliest is a fine-grained weakly foliated dolerite cut by numerous thin carbonate veinlets and clearly pre-dated deformation. The second is nonfoliated and is composed of randomly orientated plagioclase crystals with interstitial pyroxenes and ?devitrified glass (Fig. 33), and post-dates deformation.

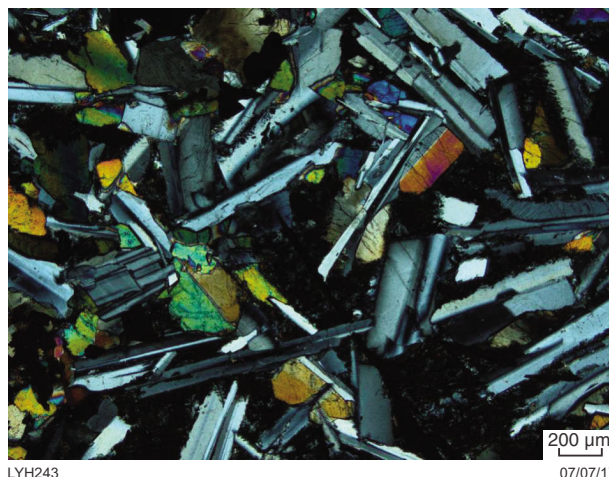


Figure 33. Dolerite composed of randomly orientated plagioclase crystals with interstitial pyroxenes and ?devitrified glass from the Franklin Prospect (GSWA 206316 from 215.5 m in 09FKRCD001), crossed polars

Alteration and metamorphic minerals

Chlorite

Chlorite is ubiquitous in the schists within 09FKRCD001 including the schists containing andalusite (Fig. 30a,b,d), kyanite (Fig. 30c,d) and sillimanite (Fig. 30b). It occurs as fine-grained aggregates, commonly intergrown with or replacing white mica in the matrix between the quartz grains and as elongate crystals along foliation. All of the chlorite observed in thin section is very pale green (Figs 30f, 31) suggesting that it is Mg rich. This is supported by HyLogger data which shows Mg-rich chlorite throughout except for some Fe enrichment in the schist adjacent to dolerite (Fig. 29d). Semiquantitative SEM analyses also indicate a high Mg content with Mg# ranging from 0.81 to 0.85 (Table 11).

White micas

Most of the white mica observed in thin section is very fine-grained and is partially replaced by chlorite or andalusite in the matrix surrounding quartz grains (Fig. 30a, d). Larger flakes of white mica and white mica with a sheaf-like form (Fig. 34a,b) are relatively rare. In the example shown in Figure 34a and b, the coarse flakes of white mica appear to replace Phase x and are in turn replaced by a sheath of white mica and chlorite.

Table 11. SEM analyses of chlorite from the Franklin Prospect

Sample	206314	206314	206314	206311	206311
SiO ₂	36.44524195	35.65338892	33.40885585	36.76814775	37.74825572
MgO	26.35981945	26.09427972	25.26588376	24.41368838	23.53381475
FeO	10.52958498	11.03694244	11.62709137	12.28005197	12.3141092
Al ₂ O ₃	26.66535362	27.21538891	29.69816902	26.53811189	26.40382034
K ₂ O	—	—	—	—	—
TiO ₂	—	—	—	—	—
Na ₂ O	—	—	—	—	—
CaO	—	—	—	—	—
MnO	—	—	—	—	—
Mg/Mg+Fe	0.851881359	0.844519803	0.833119474	0.820383745	0.814493172

NOTE: — not analysed or below detection

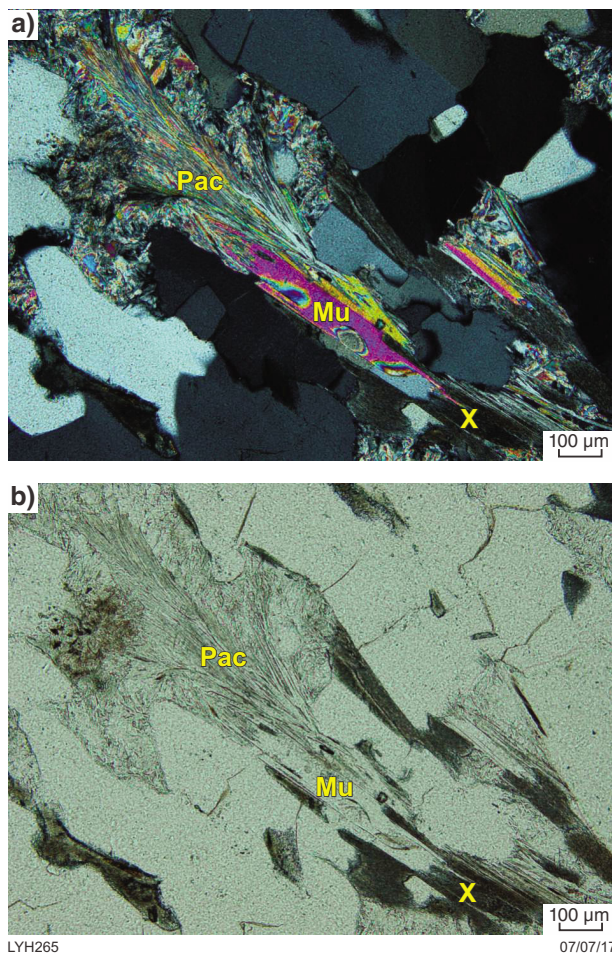


Figure 34. Flakes of muscovite (Mu) replacing Phase x (X) and in turn replaced by sheath of paragonitic aluminoceladonite (Pac) at the Franklin Prospect (GSWA 206309 from 163.1 m in 09FKRCD001): a) crossed polars; b) plane-polarized light

The plot of the wavelength of the white mica 2200 absorption feature vs depth (Fig. 29e) suggests that most of the white mica is paragonite with rare occurrences of muscovite. Semiquantitative SEM analysis (Table 12) indicates that the mica chemistry is more complex, and there are large variations in mica chemistry even within the same section. Analyses 1 and 2 of the largest flake of white mica in Figure 34 are typical of muscovite with K₂O significantly greater than Na₂O. Analysis 3 from the other large flake of mica in Figure 34 contains more K₂O, more SiO₂ and less Al₂O₃ than typical muscovite and is best described as phengite. The white mica with a sheath-like form in Figure 34 (Analyses 4 and 5) and white mica with a sheath-like form in GSWA 206314 (Analyses 13–15) contain a significant amount of MgO and FeO and have Na₂O greater than K₂O. It is best described as paragonitic aluminoceladonite. Some of the small flakes of white mica with high Na₂O content also contain a significant amount of MgO and FeO (Analyses 6 and 7) and could be described as paragonitic aluminoceladonite. Other small flakes have compositions intermediate between paragonite and muscovite (Analyses 8–12).

Amphiboles

Apart from the presence of hornblende in the mafic intrusions, the only amphibole observed was gedrite which occurs as wispy aggregates in the schist (Fig. 30e). Semiquantitative SEM analyses are given in Table 13.

Phase x

Phase x is a mineral or mineral aggregate that appears to be pleochroic from brown when aligned north–south (Fig. 35a) to dark bluish grey to black when aligned east–west (Fig. 35b). Phase x is common in the schists throughout drillhole FKRC0001 and is abundant in places (Fig. 30f). Phase x is partially replaced by chlorite (Fig. 35a,b) and less commonly by white mica (Figs 34a,b, 35c,d) and possibly by gedrite, although it is also possible that it replaces gedrite (Figs 30e, 35c,d).

Table 12. SEM analyses of white mica from the Franklin Prospect

Analysis	1	2	3	4	5	6	7	8	9	10	11	12	13	14	15
Sample	206309	206309	206309	206309	206309	206309	206309	206309	206309	206309	206311	206311	206314	206314	206314
Depth (m)	163.1	163.1	163.1	163.1	163.1	163.1	163.1	163.1	163.1	163.1	169.1	169.1	182.2	182.2	182.2
Form	Large flake	Large flake	Large flake	Sheath	Sheath	Small flake	Small flake	Small flake	Small flake	Small flake	Small flake	Small flake	Sheath	Sheath	Sheath
SiO ₂	51.01	51.39	62.29	45.25	44.50	46.85	46.07	49.40	51.50	51.38	51.26	54.18	46.05	47.38	47.13
MgO	1.19	1.28	1.73	9.39	12.13	6.55	8.25	2.14	1.42	1.31	1.40	<0.01	11.05	9.97	11.08
FeO	1.91	1.93	3.49	6.43	8.15	5.06	5.77	2.39	1.24	1.99	2.12	<0.01	4.54	4.22	4.64
Al ₂ O ₃	35.73	35.55	19.07	33.64	31.27	34.98	34.00	36.49	36.43	35.68	37.25	37.37	33.16	33.08	32.09
CaO	–	–	–	–	–	–	–	–	–	–	–	–	–	–	–
TiO ₂	–	–	–	–	–	–	–	–	–	–	–	–	–	–	–
MnO	–	–	–	–	–	–	–	–	–	–	–	–	–	–	–
K ₂ O	8.19	7.78	12.63	1.19	0.92	1.96	1.57	7.58	7.84	7.44	4.75	5.21	1.38	1.64	1.54
Na ₂ O	1.97	2.06	0.78	4.10	3.04	4.60	4.36	2.00	1.57	2.20	3.22	3.23	3.81	3.72	3.53
Total	100.00	100.00	100.00	100.00	100.00	100.00	100.00	100.00	100.00	100.00	100.00	100.00	100.00	100.00	100.00

NOTE: – not analysed or below detection

Table 13. SEM analyses of gedrite from the Franklin Prospect

Sample	206317	206317	206317	206317
Drillhole	09FKRCD001	09FKRCD001	09FKRCD001	09FKRCD001
Depth (m)	226.4	226.4	226.4	226.4
SiO ₂	46.16	48.11	49.65	45.73
MgO	23.44	20.01	21.55	25.37
FeO	6.15	7.14	5.99	6.17
Al ₂ O ₃	24.25	24.74	22.81	22.73
CaO	–	–	–	–
TiO ₂	–	–	–	–
MnO	–	–	–	–
K ₂ O	–	–	–	–
Na ₂ O	–	–	–	–
Mg#	0.9	0.87	0.89	0.9

NOTE: – not analysed or below detection

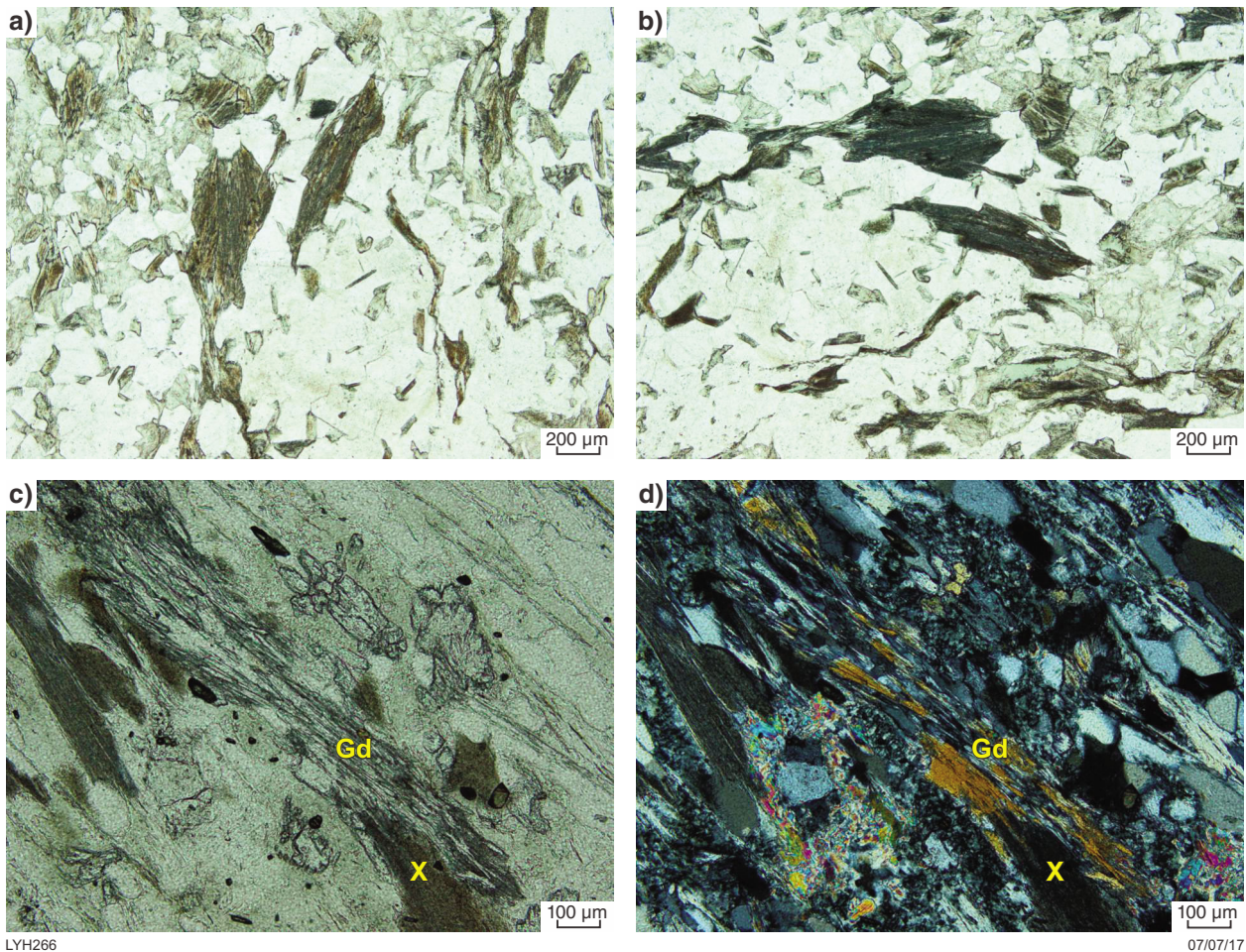


Figure 35. Phase x at the Franklin Prospect: a) grains orientated north–south in light brown (GSWA 206321 from 295.3 m in 09FKRCD001), plane-polarized light; b) as for a) but aligned east–west shown in dark bluish grey to black; c) gedrite (Gd) replaced by or replacing Phase x (X) (GSWA 206305 from 83.4 m in 09FKRCD001), plane-polarized light; d) as for c), crossed polars

Semiquantitative SEM analysis (Table 14) gave results similar to that of gedrite (cf. Table 13). Electron microprobe analysis (Table 15) gave very low totals suggesting that the phases were hydrous. Analyses 1 and 2 (Table 15) with relatively high silica are interpreted to be hydrous gedrite and Analyses 3–7 (Table 15) have analyses consistent with chlorite. The cause of the dark colouration is unknown. If Phase x was originally gedrite, the dark colour could possibly be related to submicroscopic ilmenite given the presence of small amounts of titanium in the analyses. Alternatively, if the rock was originally a tuff, Phase x could originally have been pumice fragments with the glass altered to gedrite and chlorite plus submicroscopic oxides.

Aluminium silicates

As noted above, all three aluminium silicate polymorphs are present in the schist (Fig. 30a–d). They were identified on the basis of their chemistry and their optical properties (andalusite has a maximum of first-order yellow interference colours; kyanite has up to first-order red interference colours, inclined extinction and sometimes shows twinning; and sillimanite has up to second-order blue interference colours and straight extinction). Semi-

quantitative SEM analyses (Table 16) confirm that these minerals are aluminium silicates with only very minor Fe as an impurity.

Talc

Talc was only present as an alteration mineral in the gabbro–pyroxenite.

Xenotime

Xenotime is a minor alteration mineral along fractures in zircon within schist (Fig. 36). An SEM analysis (with some backscatter from surrounding zircon and chlorite) gave 13.9% Y_2O_3 , 3.0% Gd_2O_3 , 4.8% Dy_2O_3 , 23.9% P_2O_5 , 11.0% Al_2O_3 , 29.2% SiO_2 and 1.0% Co.

?Magnesiocarpholite

A mineral with low relief and up to second-order blue interference colours replaces fine-grained chlorite and white mica interstitial to quartz (Fig. 37). This mineral is interpreted to be sodium-bearing magnesiocarpholite [$MgAl_2Si_2O_6(OH)_4$] on the basis of SEM analyses (Table 17).

Table 14. SEM analyses of Phase x from the Franklin Prospect

Sample	206321	206321	206321	206314	206314	206314
Drillhole	09FKRCD001	09FKRCD001	09FKRCD001	09FKRCD001	09FKRCD001	09FKRCD001
Depth (m)	295.3	295.3	295.3	182.2	182.2	182.2
MgO	18.83	20.61	18.30	23.01	24.86	23.25
Al_2O_3	20.76	23.07	19.71	21.24	23.57	22.48
SiO_2	46.60	41.90	49.64	46.15	40.90	43.64
FeO	13.02	12.78	12.35	8.40	9.34	8.84
K_2O	0.79	0.74	–	–	–	–
TiO_2	–	0.90	–	1.19	1.33	1.79
Mg/Mg+Fe	0.77	0.79	0.77	0.86	0.86	0.86

NOTE: – not analysed or below detection

Table 15. Electron microprobe analyses of Phase x from the Franklin Prospect

Analysis	1	2	3	4	5	6	7
Sample	206321	206321	206321	206321	206321	206321	206321
SiO_2	41.66	39.89	30.05	27.38	27.14	28.72	26.47
TiO_2	1.77	0.88	0.17	0.24	0.60	0.61	2.15
Al_2O_3	17.17	18.83	21.11	22.87	22.66	22.48	21.89
FeO	10.21	11.20	13.67	13.83	13.85	13.37	13.80
MnO	0.01	0.05	0.03	0.06	<0.01	0.03	0.01
MgO	16.41	17.02	20.26	21.11	20.69	20.39	21.32
CaO	<0.01	<0.01	<0.01	<0.01	<0.01	<0.01	<0.01
Na_2O	0.04	0.03	0.01	0.05	0.03	0.03	0.02
K_2O	0.36	0.43	0.30	0.50	0.32	0.59	0.27
Total	87.64	88.32	85.61	86.05	85.30	86.23	85.93

Table 16. SEM analyses of aluminium silicates from the Franklin Prospect

Spectrum	206314	206314	206314	206314	206314	206314	206314	206314	206314	206311	206309	206309
Drillhole	09FKRCD001	09FKRCD001	09FKRCD001	09FKRCD001	09FKRCD001	09FKRCD001	09FKRCD001	09FKRCD001	09FKRCD001	09FKRCD001	09FKRCD001	09FKRCD001
Depth (m)	182.2	182.2	182.2	182.2	182.2	182.2	182.2	182.2	182.2	169.1	163.1	163.1
Mineral	Andalusite	Andalusite	Andalusite	Andalusite	Andalusite	Sillimanite	Sillimanite	Sillimanite	Andalusite	Kyanite	Kyanite	Kyanite
SiO ₂	38.79	42.46	38.71	38.02	39.88	40.62	37.88	39.40	39.67	37.71	38.47	43.88
MgO	—	—	—	—	—	—	—	—	—	—	—	—
FeO	—	0.71	0.70	0.83	0.67	0.93	—	0.70	—	—	—	—
Al ₂ O ₃	61.21	56.84	60.59	61.15	59.44	58.45	62.12	59.90	60.33	62.29	61.53	56.12
CaO	—	—	—	—	—	—	—	—	—	—	—	—
TiO ₂	—	—	—	—	—	—	—	—	—	—	—	—
MnO	—	—	—	—	—	—	—	—	—	—	—	—
K ₂ O	—	—	—	—	—	—	—	—	—	—	—	—
Na ₂ O	—	—	—	—	—	—	—	—	—	—	—	—

NOTE: — not analysed or below detection



Figure 36. Xenotime (Xn) replacing zircon (Zr) along fractures at the Franklin Prospect (GSWA 206314 from 182.2 m in 09FKRCD001), crossed polars

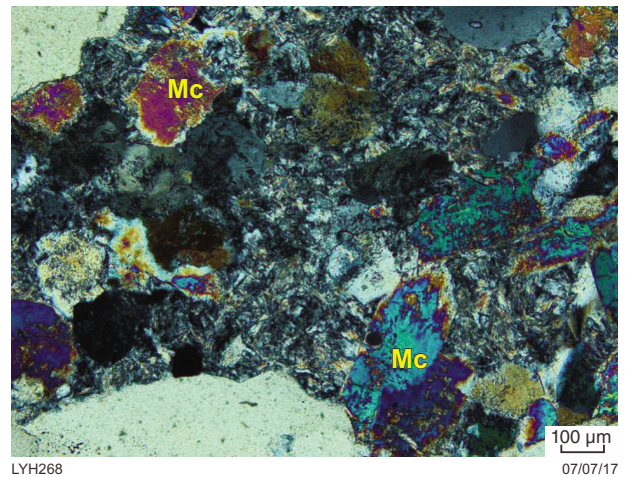


Figure 37. Magnesiochlorite (Mc) replacing fine-grained chlorite and white mica interstitial to quartz at the Franklin Prospect (GSWA 206317 from 226.4 m in 09FKRCD001), crossed polars

Table 17. SEM analyses of ?magnesiocarpholite from the Franklin Prospect

Sample	206317	206317	206317	206317	206317
Drillhole	09FKRCD001	09FKRCD001	09FKRCD001	09FKRCD001	09FKRCD001
Depth	226.4	226.4	226.4	226.4	226.4
SiO ₂	48.78	50.52	48.56	51.32	47.63
MgO	9.65	9.73	10.13	9.30	10.16
FeO	1.71	1.25	1.39	2.01	1.78
Al ₂ O ₃	37.19	36.93	37.96	35.80	38.56
CaO	0.89	—	—	—	—
TiO ₂	—	—	—	—	—
MnO	—	—	—	—	—
K ₂ O	—	—	—	—	—
Na ₂ O	1.78	1.56	1.97	1.57	1.87

NOTE: — not analysed or below detection

Dicksons (Silver Swan) Prospect

Diamond drillhole DKRCD001A was drilled to test felsic volcanics of the Yaloginda Formation. Although Wellman (2010) refers to the location as the Dicksons Prospect, the site is actually 2.7 km southwest of the Dicksons base metal prospect of Newmont and CRA Exploration Pty Ltd and 6.8 km northeast of the Austin deposit (Fig. 2). The drillhole intersected some gold mineralization but no base metal mineralization. A log for drillhole DKRCD0001A is given in Appendix 1h (on zip file) and is shown pictorially in Figure 38c.

Lithologies intersected

Rhyolite

Rhyolite with phenocrysts of quartz, cloudy alkali feldspar and white mica in a fine-grained crystalline matrix of quartz, cloudy alkali feldspar, albite and biotite (Fig. 39) was intersected at several places in DKRCD001A.

Felsic breccia

Felsic breccia with light-coloured fragments ranging from less than 1 cm up to 3 cm across in a darker grey matrix (Fig. 40a) was intersected in DKRCD001A between the start of the diamond core at 80.8 m and 100 m. The fragments become less obvious with depth. The fragments contain scattered phenocrysts of quartz and alkali feldspar in a groundmass of fine-grained quartz and minor very fine-grained mafic minerals (Fig. 40b,c). The matrix consists of abundant quartz and feldspar crystals with interstitial fine-grained white mica and chlorite (Fig. 40d,e). The matrix also contains a brown to dark bluish grey or black mineral (Fig. 40d,e) similar to Phase x at the Franklin Prospect as described above. It is not certain if this breccia is a felsic autobreccia or a lithic tuff.

Between 129 and 132.8 m in DKRCD001A, massive rhyolite with visible phenocrysts alternates with biotite schist with remnant quartz grains (Fig. 40f) and is interpreted as coarser grained volcanic breccia (fragments 5–30 cm) with sheared matrix.

Felsic schist with quartz aggregates

Schist with irregular to oval-shaped aggregates of quartz in a schistose matrix of quartz, chlorite and mica similar to that observed in the Austin drillcore is interpreted to be sheared porphyritic rhyolite or volcanic breccia.

Schist

Schists of less certain protolith are intercalated with the rhyolite and volcanic breccia. They generally show strong compositional layering with individual layers composed of variable amounts of quartz, hornblende or actinolite, biotite, epidote and feldspar (Fig. 41). These schists are possibly after interflow sediments or tuffs that have sheared more readily than the surrounding more competent rhyolite.

Basalt

Fine-grained weakly sheared mafic rocks composed of amphibole, chlorite, quartz, feldspar, carbonate and ilmenite (Fig. 42) are interpreted to be altered basalt.

Dolerite

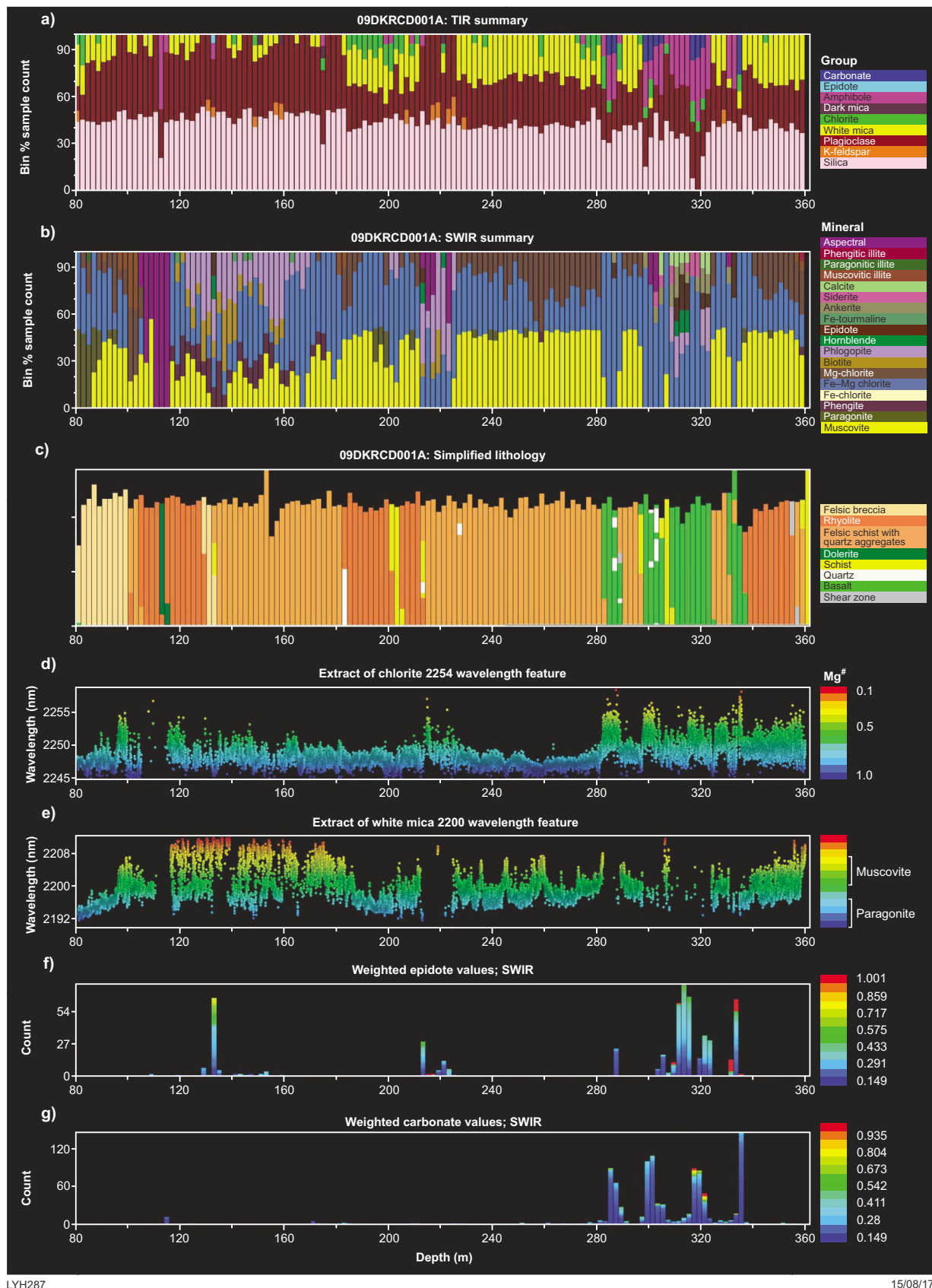
Dark fine-grained dolerite intrudes the rhyolite between 112.2 and 114.4 m in DKRCD001A.

Mineralization

Weak gold mineralization was intersected in DKRCD001A with best intersections of 2 m at 3.05 ppm between 282–284 m and 1 m at 0.59 ppm Au between 289–290 m. The gold mineralization is in altered basalt with disseminated pyrite along fractures and foliation planes. No base metal mineralization was intersected.

Alteration

Alteration in this drillhole could reflect distal alteration related to base metal mineralization as well as alteration related to gold mineralization.



LYH287

15/08/17

Figure 38. HyLogger, lithology and assay data for drillhole 09DKRCD001 from Silver Swan Group's Dicksons Prospect: a) TIR summary plot; b) SWIR summary plot; c) simplified lithology; d) chlorite wavelength; e) white mica wavelength; f) weighted epidote values; d) weighted carbonate values

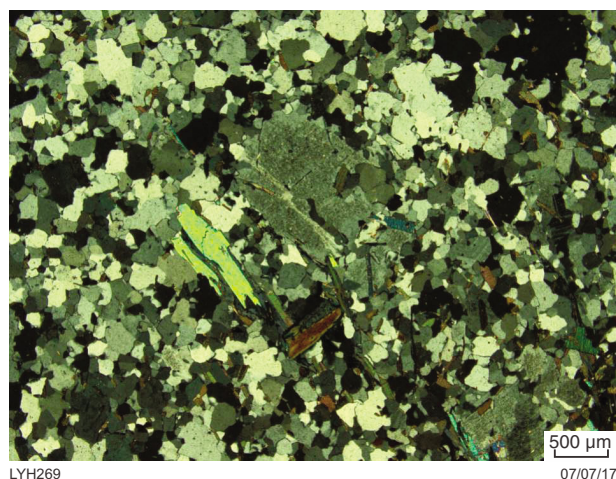


Figure 39. Rhyolite from Silver Swan Group's Dicksons Prospect (GSWA 204933 from 108.6 m in DKRCD001), crossed polars

Chlorite

Chlorite is present throughout the core in DKRCD001A (Fig. 38a,b) in felsic rocks (Fig. 40d,e) and basalt (Fig. 42). The wavelength of the chlorite 2250 absorption feature suggests that the chlorite in the felsic rocks tends to be relatively Mg rich compared with chlorite in the basalts which is relatively iron rich (Fig. 38d).

White mica

White mica is a common alteration mineral of feldspar in felsic rocks (Fig. 40c, e) but is also a probable primary mineral in the rhyolite (Fig. 39). Based on the wavelength of the white mica 2200 absorption feature, white mica in the felsic breccia in the upper part of DKRCD001A is paragonitic, but elsewhere most of the white mica is close to normal muscovite in composition with a tendency towards paragonite in places (Fig. 38e).

Amphiboles

In addition to the expected occurrence of amphiboles in the basalt and dolerite, hornblende and actinolite are also present in some of the compositionally layered schists (Fig. 41a,b). In addition, SWIR HyLogger data have identified hornblende occurring in rhyolite within the alteration halo surrounding a quartz vein (Fig. 43a,b). The characteristic secondary MgOH absorption feature is at 2395 nm, within the typical range for hornblende (2390–2400 nm according to Pontual, 2008) and much higher than the typical value for actinolite (c. 2384 nm). Actinolite also has an absorption feature at about 2117 nm which is lacking in hornblende and the amphibole in the alteration halo of the quartz vein. The presence of hornblende in the alteration zone adjacent to the quartz vein is strong evidence that the hornblende was introduced hydrothermally.

Phase x

A brown to dark bluish grey or black mineral similar to Phase x at the Franklin Prospect was observed in the matrix of the felsic breccia (Figs 40d,e, 44). The original nature of Phase x is uncertain; possibly it replaces pumice as it is similar in appearance to interpreted pumice replaced by chlorite at Austin (Fig. 9d); alternatively, it may have replaced a ferromagnesian mineral such as biotite. In places, Phase x is replaced by white mica (Fig. 44).

Plagioclase

Albite replaces alkali feldspar in the rhyolite and in the volcanic breccia (Fig. 40d,e). In one section of compositionally layered schist, albite is present as large irregular masses that appear to replace alkali feldspar and are in turn replaced by clinozoisite, epidote and sericite (Fig. 41c); it is likely that this feldspar is a product of hydrothermal alteration.

Epidote group minerals

The SWIR weighted plot for epidote (Fig. 38f) indicates that epidote is abundant in the basalt and is locally abundant in the schist. In the schist, it is disseminated along foliation planes (Fig. 41a,b) or replaces coarse-grained feldspar (Fig. 41c). Epidote is also abundant at the contact between rhyolite and compositionally layered schist (Fig. 41d). Clinozoisite is much less common but was observed replacing feldspar (Fig. 41c). Allanite is also a rare accessory mineral in the schist.

Carbonate

Carbonate is an abundant alteration mineral in the basalt (Fig. 38a,b,g) and varies from calcite to siderite in composition. Carbonate was also observed at the contact between rhyolite and compositionally layered schist in association with epidote (Fig. 41d).

Tasman Prospect

Drillhole 10TJD001 was drilled to test the gossan at the T&J (also known as T and J) Prospect where Newmont had previously intersected minor base metal mineralization. Partially oxidized sulfide mineralization was intersected between 60 and 82 m. A log for drillhole 10TJD001 is given in Appendix 1i (on zip file) and is shown pictorially in Figure 45c. A summary TIR plot of mineral groups is given in Figure 45a and a summary SWIR plot of minerals is given in Figure 45b. It should be noted that stratigraphy is interpreted to young downwards in this drillcore.

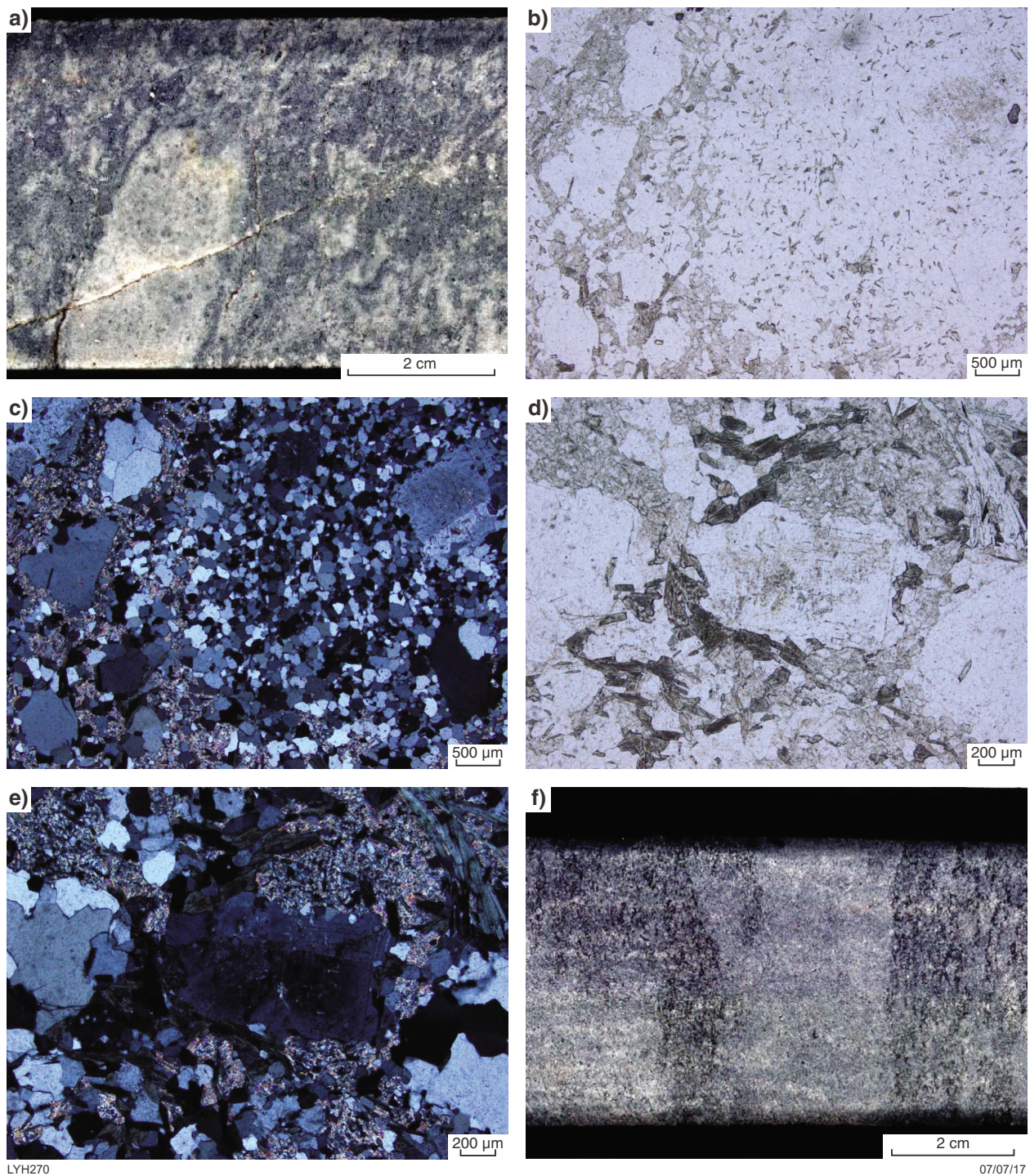


Figure 40. Felsic breccia from Silver Swan Group's Dicksons Prospect: a) core with light-coloured felsic fragment in grey matrix (85.0 m in 09DKRCD001); b) fragment containing scattered phenocrysts of quartz and alkali feldspar in a groundmass of fine-grained quartz and minor very fine-grained mafic minerals (GSWA 204932 from 90.0 m in 09DKRCD001), plane-polarized light; c) as for a), crossed polars; d) matrix to breccia composed of quartz, feldspar crystals and Phase x with interstitial fine-grained white mica and chlorite, same sample as a) and b), plane-polarized light; e) same view as c), crossed polars; f) coarse-grained volcanic breccia with sheared matrix (core from 130.1 m, 09DKRCD001)

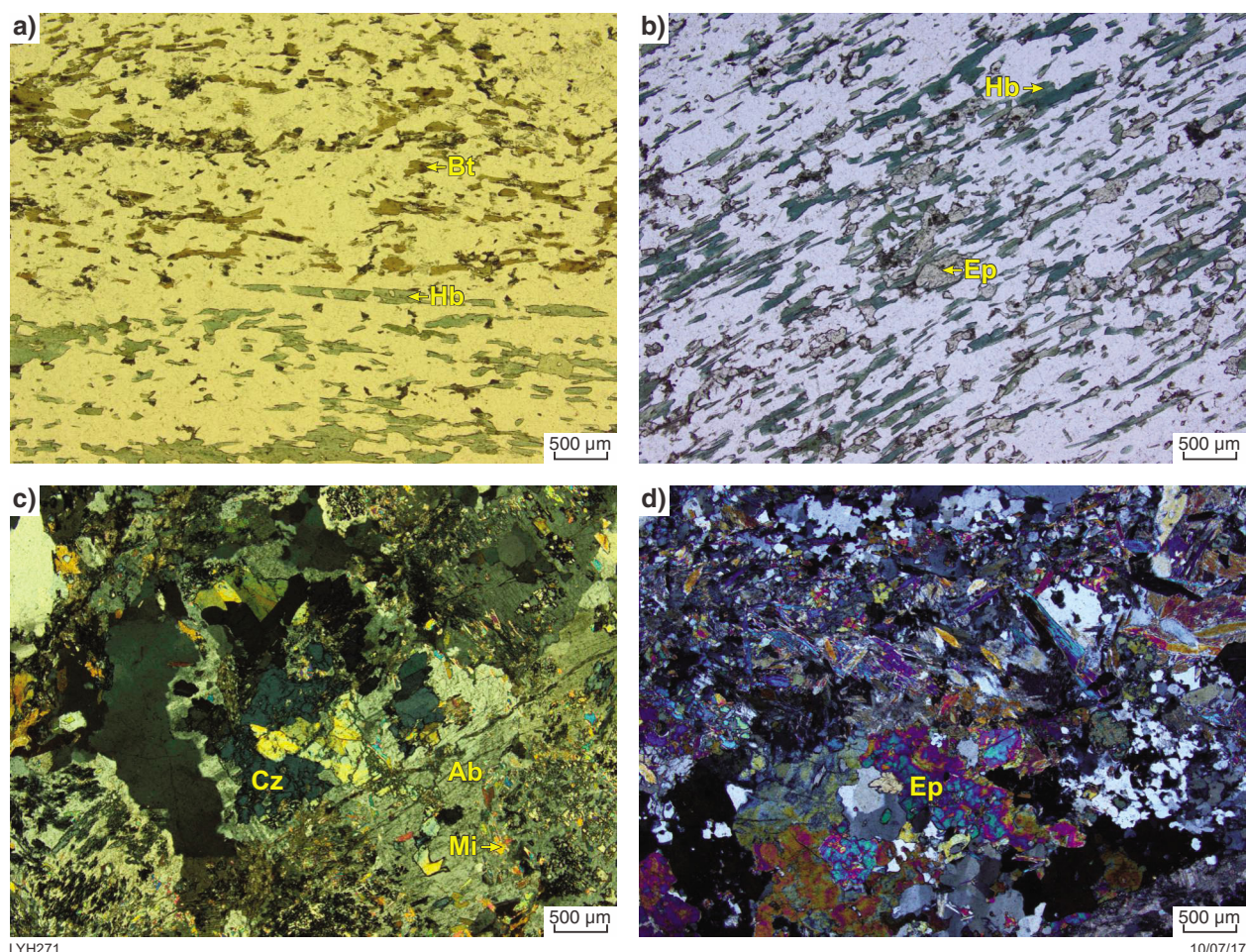


Figure 41. Schist intercalated with rhyolite and volcanic breccia from Silver Swan Group's Dicksons Prospect: a) compositionally layered schist with upper layer composed of quartz, feldspar and biotite (Bt), and lower layer composed of quartz, feldspar and hornblende (Hb) (GSWA 204937 from 133.3 m in 09DKRCD001), plane-polarized light; b) strongly sheared rock composed of quartz, hornblende and epidote (Ep) (GSWA 204939 from 213.0 m in 09DKRCD001), plane-polarized light; c) large irregular masses of albite (Ab) that appear to replace alkali feldspar and are in turn replaced by clinozoisite (Cz) and white mica (Mi) (GSWA 204936 from 132.7 m in 09DKRCD001), crossed polars; d) coarse-grained epidote replacing feldspar in schist same sample as c), crossed polars

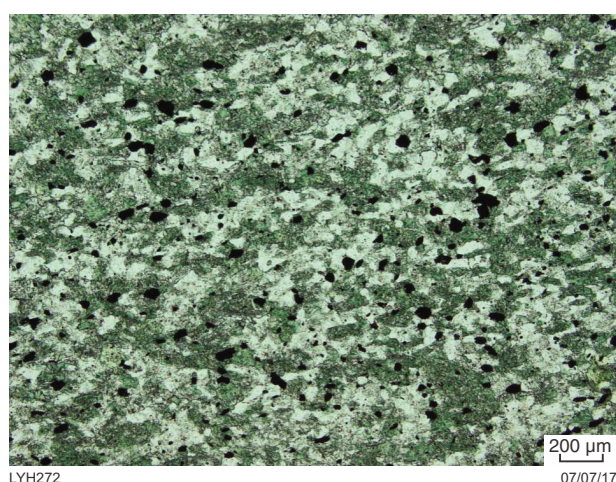


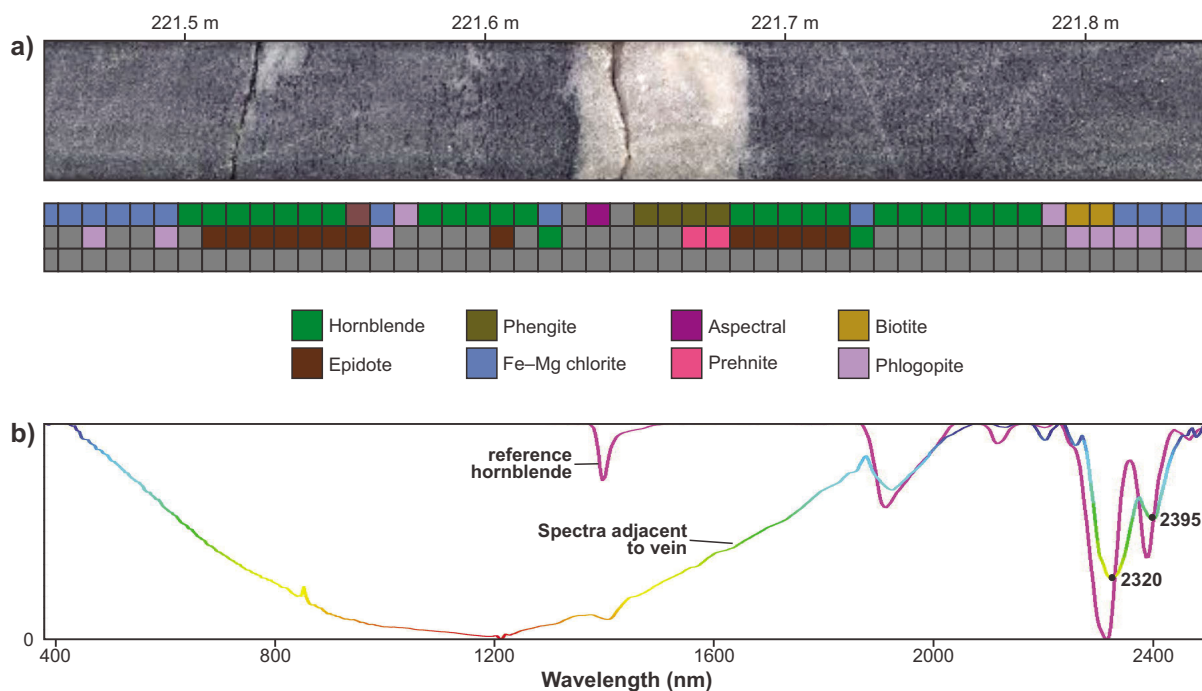
Figure 42. Basalt from Silver Swan Group's Dicksons Prospect (GSWA 204940 from 336.5 m in 09DKRCD001), plane-polarized light

Lithologies intersected

Tuff or metasedimentary rocks and schist of uncertain protolith

Weathered compositionally layered rocks (Fig. 46a) were intersected proximal to mineralization between 60.5 and 61.3 m in 10TJD001. Layering in these rocks appears to be sedimentary in origin as there are some thin iron-rich laminae. These rocks are interpreted as waterlain tuffs or metasedimentary rocks. Possible tuff or metasedimentary rock was also intersected farther downhole from 81.6 – 87.7 m and 88.35 – 93.1 m on either side of BIF. Some of this rock is compositionally layered as above but some is more massive and composed of a crystalline mozaic of quartz and chlorite (Fig. 46b).

Weakly to strongly foliated rocks composed mainly of quartz with chlorite or white mica defining foliation (Fig. 46c) were logged as felsic schist. These rocks contain



LYH279

07/08/17

Figure 43. Quartz vein with alteration halo of amphibole and epidote in rhyolite from Silver Swan Group's Dicksons Prospect (221.6 m in 09DKRCD001): a) core and TSG interpretation of minerals; b) spectra compared with reference hornblende in TSG

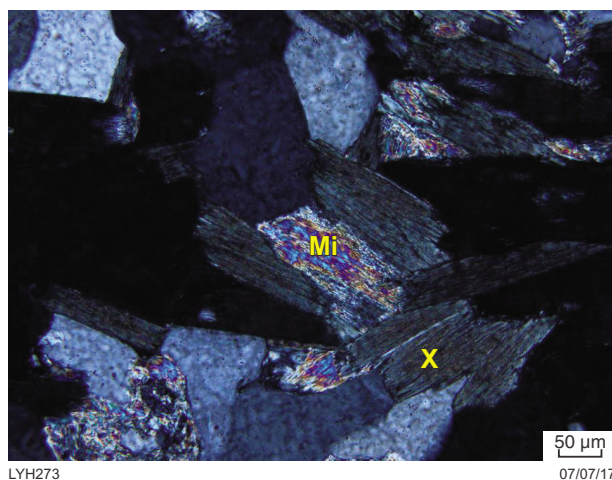


Figure 44. White mica (Mi) replacing Phase x (X) (GSWA 204932 from 90.0 m in 09DKRCD001), crossed polars

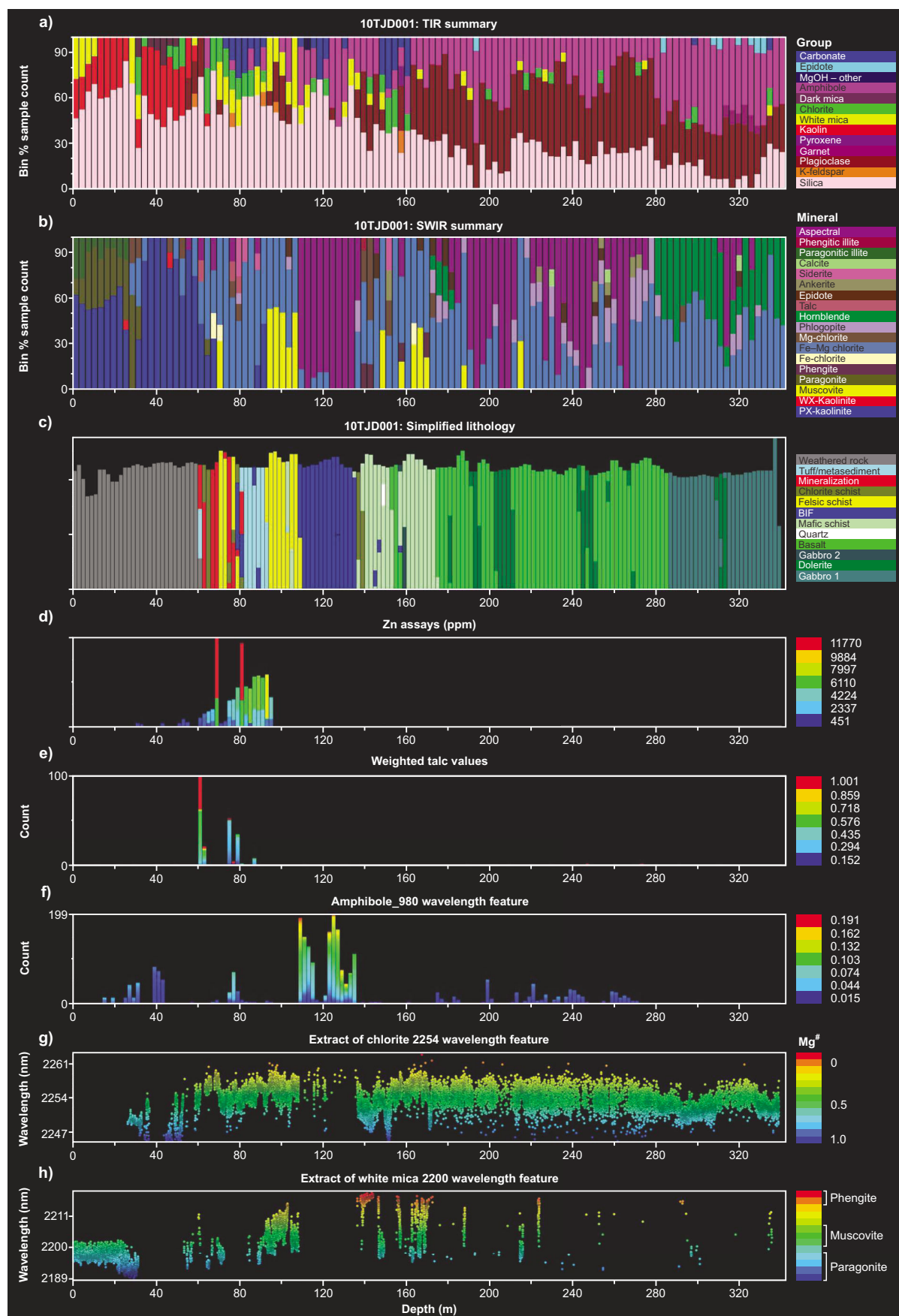
little or no feldspar and show no evidence of quartz phenocrysts. The protolith of these rocks is uncertain; they may be after felsic volcanic rocks as interpreted by Wellman (2010) but could also have a sedimentary protolith.

Schist composed mainly of iron-rich chlorite with minor quartz (Fig. 46d) was logged as chlorite schist. The protolith of the chlorite schist is uncertain; it could be after mafic tuff, silicate-facies BIF or altered felsic volcanic rock.

BIF

Several horizons of BIF were intersected by 10TJD001. The main horizon extends between 108.8 and 135.9 m and marks the boundary between mafic rocks and felsic schist. Within the main BIF horizon, finely laminated oxide-facies BIF alternates with finely to coarsely laminated silicate-facies BIF. In places, there is evidence of slump folding (Fig. 47a). An unusual feature of the main BIF horizon is the presence of cauliflower-like structures made up of stacks of green globular-shaped bodies that are elongated roughly perpendicular to the laminations (Fig. 47b). The green globular bodies consist predominantly of very fine-grained chlorite with scattered fine-grained grunerite crystals and magnetite. Grunerite crystals wrap around these globular chloritic bodies (Fig. 47c,d). These structures are interpreted to have formed as a result of escaping gases or fluids during diagenesis and replacement of the bubbles by chlorite. Between these structures and elsewhere in the main BIF horizon, the laminae consist of varying amounts of grunerite, magnetite and quartz, and in places also include chlorite, talc, white or brown mica, and carbonate.

Narrow horizons of BIF are present proximal to mineralization in the upper part of the drillhole. These consist of layers with abundant, fine-grained, euhedral to anhedral magnetite alternating with layers of pure quartz or mixtures of quartz, carbonate, chlorite and talc (Fig. 47e). Minor BIF horizons were also intercalated with tuff or metasedimentary rocks, and with mafic schist.



LYH288

14/08/17

Figure 45. HyLogger, lithology and assay data for drillhole 10TJD001 from the Tasman prospect: a) TIR summary plot; b) SWIR summary plot; c) simplified lithology; d) Zn values; e) weighted talc values; f) distribution of Ca-poor amphiboles on basis of the 980 absorption feature; g) chlorite wavelength; h) white mica wavelength

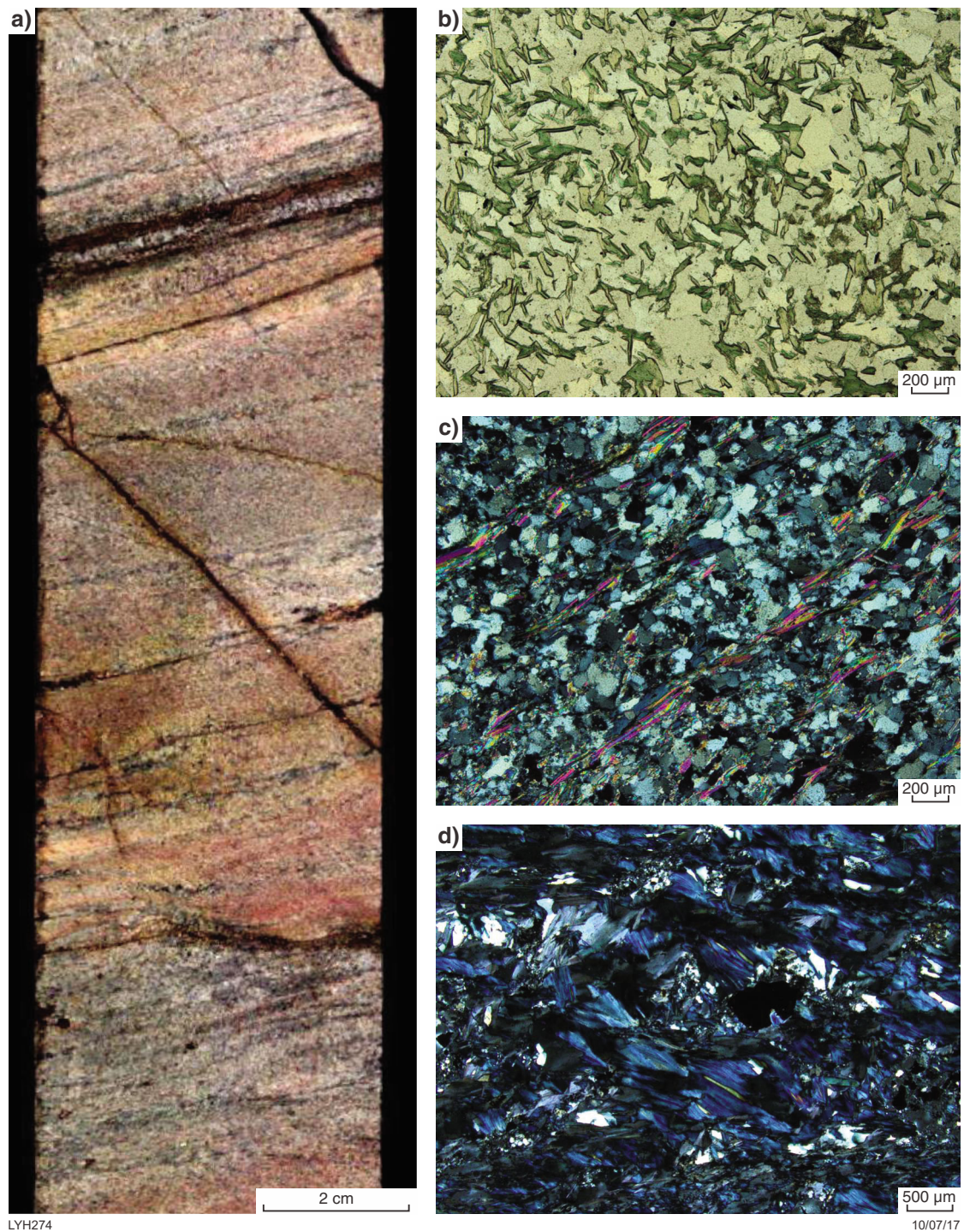


Figure 46. Tuff, metasedimentary rocks and schist of uncertain protolith from the Tasman Prospect: a) core sample of waterlain tuff or metasedimentary rock with ferruginous laminae (60.8 m in 10TJD001); b) rock composed of crystalline mosaic of quartz and chlorite (GSWA 206330 from 84.2 m in 10TJD001), plane-polarized light; c) schist with white mica defining foliation (GSWA 206335 from 105.1 m in 10TJD001), crossed polars; d) schist composed mainly of iron-rich chlorite with minor quartz (GSWA 206322 from 63.7 m in 10TJD001), crossed polars

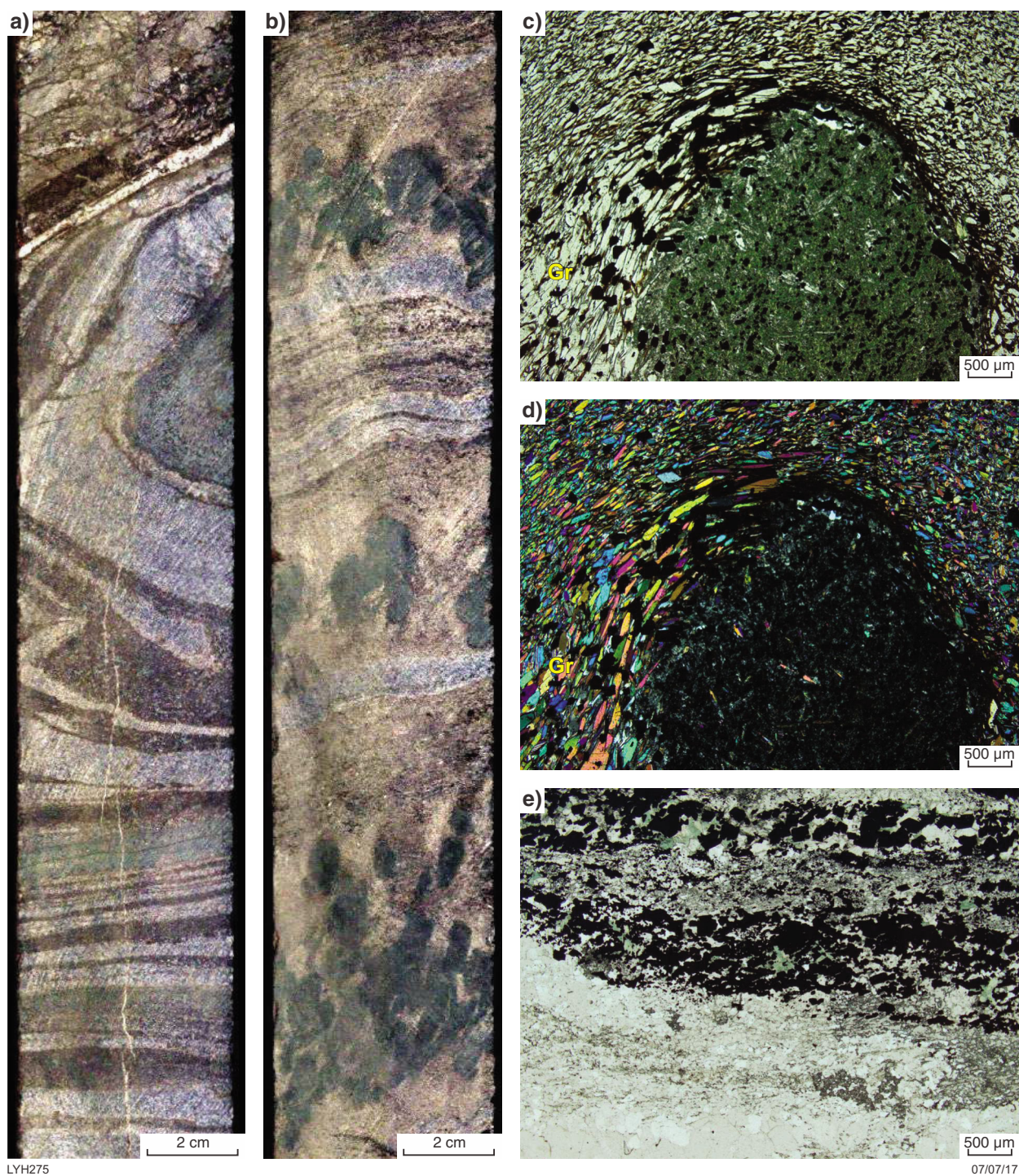


Figure 47. BIF from the Tasman Prospect: a) soft sediment slump within laminated BIF (core from 123.9 m in 10TJD001); b) globular green chloritic structures within BIF distal to mineralization (core from 124.7 m in 10TJD001); c) grunerite crystals (Gr) wrapping around globular green chloritic body with scattered fine-grained grunerite crystals and magnetite (GSWA 206330 from 84.2 m in 10TJD001), plane-polarized light; d) same view as c), crossed polars; e) BIF proximal to mineralization, composed of fine-grained euhedral to anhedral magnetite alternating with layers of quartz, carbonate and chlorite (GSWA 206331 from 87.9 m in 10TJD001), plane-polarized light

Mafic rocks

Basalt

Amygdaloidal basalt was intersected in the lower half of 10TJD001 at the Tasman Prospect. The amygdalites are filled with variable amounts of hornblende and quartz (Fig. 48a) or chlorite where the basalt is more deformed and altered (Fig. 48b). The basalt was mapped as part of the Meekatharra Formation of the Polelle Group by Van Kranendonk (2011).

Mafic schist

Rocks logged as mafic schist range from those composed of chlorite, saussuritized feldspar, epidote and fine-grained oxides (Fig. 48c) to those that could be classified as amphibolite and are composed mainly of blue–green hornblende with minor saussuritized feldspar, epidote and fine-grained oxides (Fig. 48d). These mafic schists are interpreted to be sheared basalt or mafic tuff.

Intrusive mafic rocks

Two generations of gabbro were intersected in 10TJD001: a late non-foliated gabbro with fresh augite and plagioclase, and a more-altered gabbro composed of randomly orientated plagioclase, blue–green hornblende and minor oxides with carbonate, epidote, chlorite and sericite as alteration minerals. Fine-grained dolerite composed mainly of blue–green hornblende with interstitial plagioclase and scattered fine-grained oxides was also intersected.

Mineralization

Low-grade zinc mineralization was intersected in 10TJD001 (Fig. 45d). Best intersections were 1 m at 1.16% Zn at 69–70 m, and 1 m at 1.18% Zn at 81–82 m (Wellman, 2010). The sulfides in the interval 69–70 m have mostly been oxidized but remnant chlorite schist in this interval contains abundant, fine-grained, euhedral to subhedral pyrite that has been partially replaced by iron oxides (Fig. 49a). No sphalerite was observed in the section from this interval but at 66 m, there is chlorite schist containing disseminated pyrite with minor sphalerite and chalcopyrite in fractures and bordering pyrite (Fig. 49b). In the interval 81–82 m, subhedral to anhedral coarse-grained pyrite is abundant. The pyrite contains inclusions of chalcopyrite, pyrrhotite and sphalerite as well as silicates and carbonate. Sphalerite and chalcopyrite also border pyrite (Fig. 49c). The matrix is composed mainly of chlorite, carbonate and quartz with minor white mica and talc in places. In the BIF adjacent to mineralization, there is disseminated pyrite with incorporated euhedral magnetite crystals partially replaced by maghemite (Fig. 49d). Minor sphalerite and chalcopyrite are also present in the main BIF horizon (Fig. 49e) but no assays are available from this horizon.

Alteration

Summary plots of TIR and SWIR data for drillhole 10TJD001 are given in Figure 45a and b, respectively,

where they can be compared with simplified lithology (Fig. 45c), Zn values (Fig. 45d), weighted talc values (Fig. 45e), calcium-poor amphiboles as measured by the depth of the 980 nanometre wavelength feature (Fig. 45f), chlorite wavelength (Fig. 45g), and white mica wavelength (Fig. 45h).

Unfortunately, the drillhole intersected mineralization close to the weathered zone and because the hole was drilled to the north and thus up stratigraphy, the alteration zone that could be expected beneath mineralization was in the upper weathered part of the drillhole. Kaolinite formed by weathering is thus the main mineral shown in the alteration zone in both TIR (Fig. 45a) and SWIR (Fig. 45b). However, there is sufficient fresh rock in the vicinity of mineralization to give an indication of the alteration minerals (or their metamorphosed equivalents). The mineral assemblage in the main BIF horizon is also of interest.

Talc is much less abundant than at the Austin deposit but the HyLogger plot shows some talc alteration in proximity to mineralization (Fig. 45e). Minor talc was observed in the BIF close to mineralization.

The 980 nanometre wavelength feature shows strong evidence for the presence of Ca-poor amphiboles in the main BIF horizon (Fig. 45f) as expected from the observed occurrence of abundant grunerite (Fig. 47c,d). There is also weak evidence for the presence of Ca-poor amphiboles in the vicinity of mineralization (Fig. 45f) but no amphiboles were observed in thin section.

Chlorite in the mineralized zone and intervening chlorite schists is iron rich as indicated by the HyLogger data (Fig. 45g) and the anomalous blue interference colour of the chlorite in thin section (Fig. 46d). In contrast, chlorite stratigraphically below mineralization (in the upper part of the drillhole) is Mg rich. Chlorite throughout the rest of the drillhole is generally moderately Fe rich except for some horizons with more Mg-rich chlorite in the mafic schist beneath the main BIF horizon and the gabbro.

On the basis of HyLogger data (Fig. 45h), white mica in the mineralized zone is mostly muscovite, mica in the felsic schist is muscovite trending to phengite, and mica in the chlorite schist is phengite. Mica in the top 30 m of the drillhole is paragonite (or paragonitic illite) but the composition is likely to have been affected by weathering, and may not reflect alteration related to mineralization.

Carbonate is abundant in the mineralized zone and the adjacent BIF (Fig. 47e). The carbonate is iron rich (siderite or ferrodolomite). The HyLogger summary plots also show that the main BIF horizon contains carbonate in places and carbonate is an alteration mineral in the mafic rocks.

Minor garnet is present in felsic schist between the mineralized zones. The garnet has been partially replaced by chlorite along fractures (Fig. 50). Four analyses of the garnet shown in Figure 50 were made by SEM analysis. The results are shown in Table 18 together with the end-member composition as calculated using the garnet end-member calculator of Andy Tindle (www.open.ac.uk/earth-research/tindle/AGTWebData/Garnet.xls).

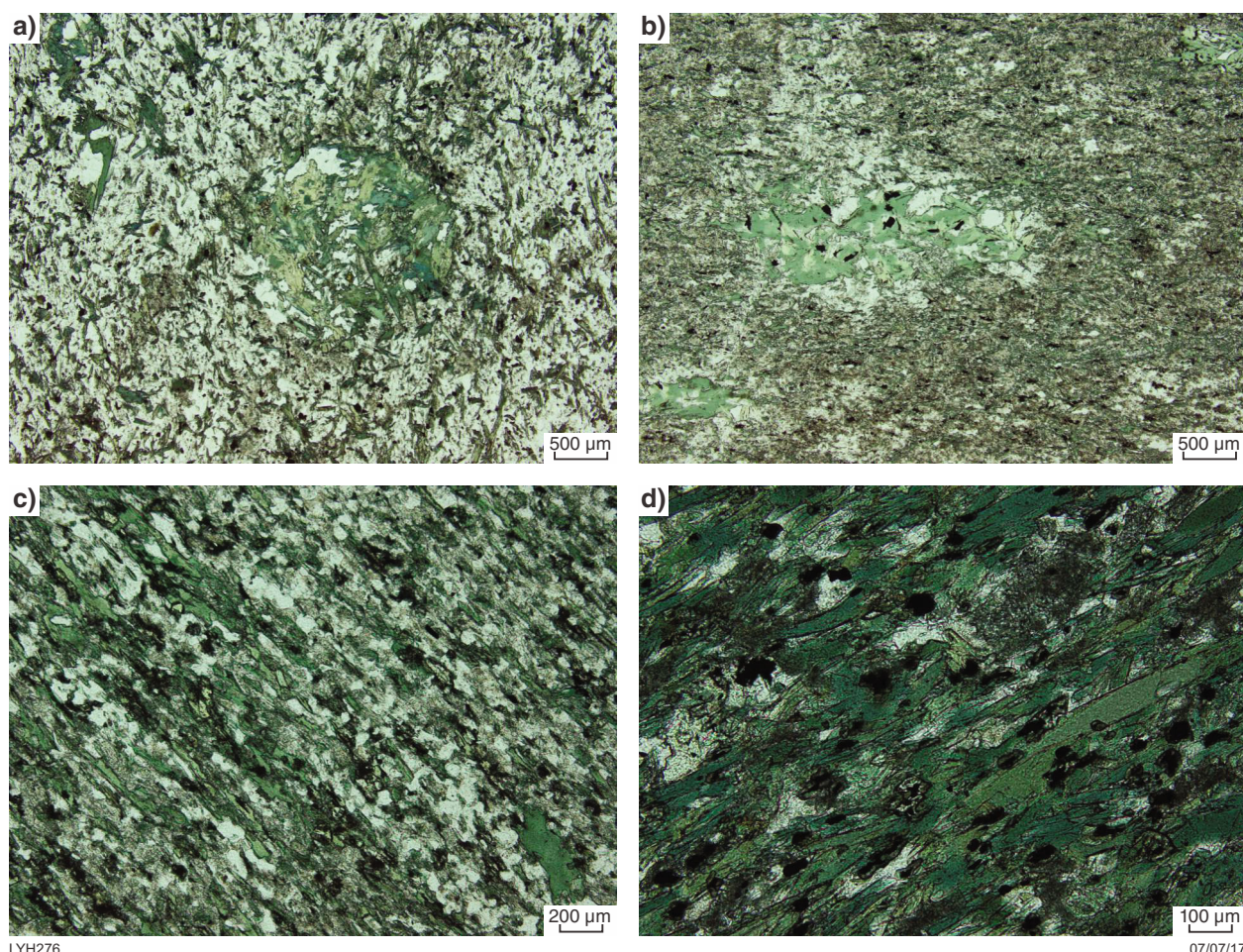


Figure 48. Mafic rocks at the Tasman Prospect: a) basalt with amygdale filled with hornblende and quartz (GSWA 206346 from 219.5 m in 10TJD001), plane-polarized light; b) deformed basalt with amygdale filled with chlorite and quartz (GSWA 206347 from 236.7 m in 10TJD001), plane-polarized light; c) mafic schist composed of chlorite, saussuritized feldspar, epidote and fine-grained oxides (GSWA 206343 from 168.1 m in 10TJD001), plane-polarized light; d) mafic schist composed mainly of blue-green hornblende, with minor epidote and fine-grained oxides (GSWA 206334 from 103.3 m in 10TJD001), plane-polarized light

The low percentage of cations may be due to backscatter of electrons from the adjacent chlorite, but the analyses are sufficient to show that almandine is the dominant component making up about 50% of the garnet. There is a significant spessartine component (about 30%) and some pyrope.

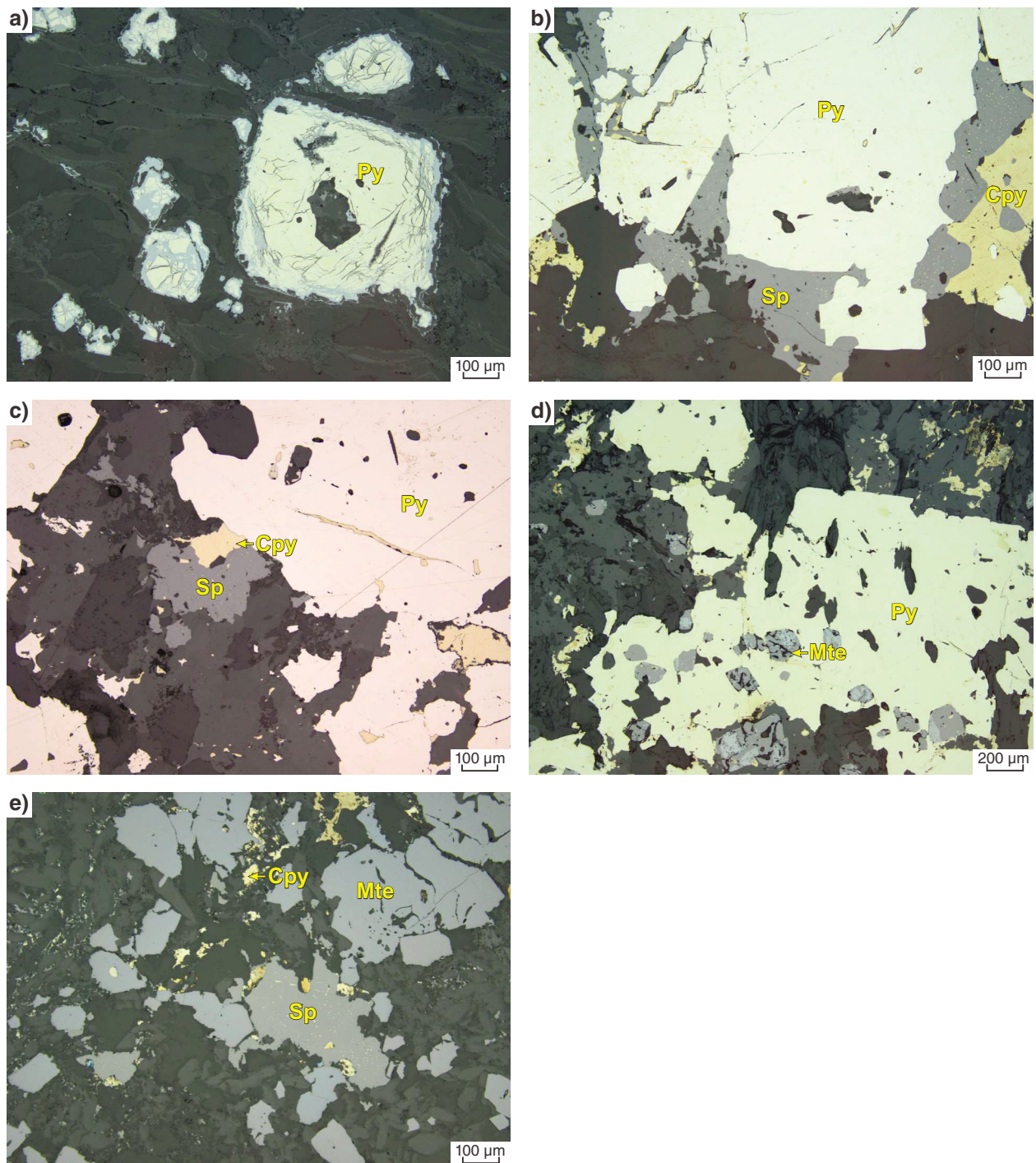
Discussion

Genesis of the alteration assemblages

Footwall alteration is a characteristic feature of all VMS deposits. In deposits that are undeformed and unmetamorphosed, it occurs either as an alteration pipe, which typically has an inner zone of chlorite and an outer zone of sericite, or as a broad, diffuse, semiconformable chloritic and sericitic alteration zone (Sangster, 1972; Gibson and Kerr, 1993; Gibson and Galley, 2007). Some

deposits also have zones of argillic or advanced argillic alteration or carbonate alteration (Galley et al., 2007). Extensive phengite and chloritic alteration may also be present in the hangingwall (Galley et al., 2007).

During metamorphism, the characteristic chloritic alteration beneath a VMS deposit can be changed to an assemblage consisting of hornblende, biotite, cordierite and anthophyllite or, if sufficient calcite is present in the original alteration zone, tremolite–actinolite, garnet and Ca-pyroxenes may also form (Sangster, 1972). Advanced argillic alteration can also be metamorphosed to garnet and andalusite or kyanite (Galley et al., 2007). In the Austin–Quinns area, there are some minerals, including anthophyllite, cummingtonite, grunerite, hornblende and rare sillimanite, that would normally be considered indicative of amphibolite-grade metamorphism but these are only locally present and chlorite is widespread, suggesting that the regional metamorphic grade is greenschist. According to Spear (1993), during the transition from greenschist facies to amphibolite facies, the amount of chlorite in the rock decreases at temperatures



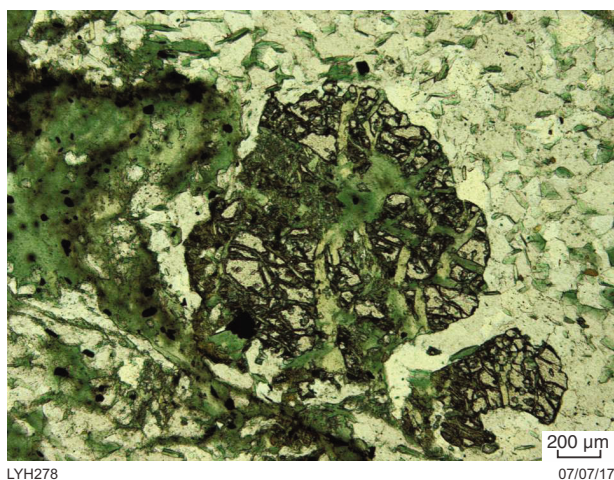
LYH277

07/07/17

Figure 49. Reflected light photomicrographs of mineralization from the Tasman Prospect: a) chlorite schist with disseminated pyrite (Py) partially replaced by iron oxides (GSWA 206324 from 69.7 m in 10TJD001); b) disseminated pyrite with minor sphalerite (Sp) and chalcopyrite (Cpy) in fractures and moulded around the edges of the pyrite (GSWA 206323 from 63.7 m in 10TJD001); c) irregular grains of pyrite with inclusions of chalcopyrite. Sphalerite and chalcopyrite also border pyrite (GSWA 206329 from 81.3 m in 10TJD001); d) pyrite with incorporated euhedral magnetite crystals partially replaced by maghemite in BIF horizon adjacent to mineralization (GSWA 206328 from 80.7 m in 10TJD001); e) sphalerite and chalcopyrite in main BIF horizon (GSWA 206338 from 124.7 m in 10TJD001)

Table 18. SEM analyses of garnet from the Tasman Prospect

Sample	206327	206327	206327	206327
SiO ₂	38.63	38.23	40.69	40.60
TiO ₂	<0.01	<0.01	<0.01	<0.01
Al ₂ O ₃	19.13	18.29	17.52	17.85
FeO	25.07	26.05	24.31	24.22
MnO	11.41	11.67	12.53	11.75
MgO	3.48	3.31	2.57	2.48
CaO	2.29	2.44	2.38	3.10
Na ₂ O	<0.01	<0.01	<0.01	<0.01
K ₂ O	<0.01	<0.01	<0.01	<0.01
Cr ₂ O	<0.01	<0.01	<0.01	<0.01
Total	100.00	100.00	100.00	100.00
Almandine	51.12	50.12	47.73	48.33
Andradite	4.46	7.49	4.73	3.89
Grossular	2.46	0.00	3.10	6.21
Pyrope	14.64	14.12	11.80	11.25
Spessartine	27.31	28.27	32.64	30.31
Uvarovite	<0.01	<0.01	<0.01	<0.01
% cations	94.93	94.15	87.88	88.57

**Figure 50. Garnet partially replaced by chlorite (GSWA 206327 from 77.0 m in 10TJD001), plane-polarized light**

above about 400°C and the amount of Ca-amphibole increases. The upper limit of the greenschist facies as defined by the stability of chlorite is approximately 550°C but this value is dependent on the bulk composition of the rock and fO_2 (Spear, 1993).

Anthophyllite is abundant in BIF and schist physically beneath the high-grade zinc zone at Austin and less commonly, cummingtonite partially replaced by anthophyllite is also present in the schist (Fig. 16b,c). Grunerite is also abundant in the main BIF horizon at

the Tasman Prospect (Fig. 47c,d). The calcium-poor amphiboles could be interpreted to have formed under amphibolite-facies metamorphism of early talc and chlorite alteration, and their subsequent regression back to chlorite and talc. However, this would not explain the presence of abundant talc without remnant amphiboles in the mineralized horizon, the widespread occurrence of Fe–Mg chlorite distal to mineralization at Austin, the association of iron-rich chlorite with mineralization at the Tasman Prospect, or the presence of iron-rich chloritic bodies associated with grunerite in the main BIF at the Tasman Prospect (Fig. 47c,d).

An alternative interpretation is that the calcium-poor amphiboles are related to the hot hydrothermal fluids that formed the mineralization. Actinolite and calcium-poor amphiboles, including cummingtonite and Mn-rich amphiboles, are associated with talc in the upper part of the Mattagami Lake Mine. Costa et al. (1983) interpreted them as possibly deposited from sea-floor brine together with the talc and sulfides. Evans and Ghiorso (1995) reported that cummingtonite forms over a wide range of conditions (400–800°C and <1–15 kbar) provided that whole-rock compositions are within the FeO-rich corner of projected phase diagrams such as the (Al₂O₃ + Fe₂O₃)–CaO–(FeO + MgO + MnO) (ACF) ternary diagram.

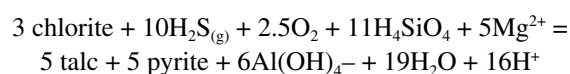
Maximum vent temperatures for modern-day mid-ocean ridge, back-arc basin, and back-arc spreading centres range from 220 to 380°C although temperatures up to 420°C have been recorded in higher salinity fluids, such as the Atlantis II Deep in the Red Sea where salinities are about 15–20 wt% NaCl (Barrie, 1999). Monecke et al. (2014) found that modern-day arc-related copper

deposits are currently forming at water depths exceeding 1000 m whereas zinc and lead deposits can occur at any water depth. Massive sulfides forming in arc-related rifts are generally restricted to water depths of 700 to 2000 m; deposits forming in back-arc spreading centres occur at water depths of 1500 to 2000 m and the deepest hydrothermal systems occur along mature back-arc spreading centres where water depths range from about 2000 to 3700 m (Fig. 51). The high ambient pressures in the mature back-arc spreading centres prevent the fluids from boiling. Increase in salinity from 3.2 wt % NaCl to 6 wt % NaCl moves the critical point from 408 to 430°C and adding CO₂ to the fluid shifts the two-phase boundary to deeper depths (Monecke et al., 2014). Hassan (2014) suggested that if the venting solutions were highly saline, it is possible that temperatures were just high enough to form cummingtonite and anthophyllite in BIF on the seafloor at the Just Desserts deposit, 160 km south-southeast of Austin. Similarly, the anthophyllite in BIF at Austin and grunerite in the main BIF at the Tasman Prospect could also have been formed from hot brines on the ocean floor. The iron-rich chloritic structures surrounded by grunerite in BIF at the Tasman Prospect (Fig. 47b–d) are interpreted to have formed as a result of escaping gases or fluids during diagenesis and replacement of the bubbles by chlorite as fluids cooled down. In places at the Just Desserts and nearby C Zone prospect at Yuinmery, anthophyllite, cordierite, and more rarely, cummingtonite and hypersthene are localized adjacent to irregular veins and appear metasomatic in origin. These minerals were interpreted to have formed on pathways along which very hot hydrothermal fluids flowed (Hassan, 2014; Hassan and Roberts, 2017) whereas talc and chlorite were formed by cooler fluids. The cummingtonite physically beneath the lower mineralized horizon at Austin (and probably also stratigraphically beneath it by analogy with the alteration pattern at Just Desserts), is also interpreted to have been formed as a result of alteration by very hot fluids rather than by metamorphism as the cummingtonite is localized and found close to sulfide-rich breccia zones that may have been pathways for hydrothermal fluids (Fig. 52).

The upper mineralized horizon at Austin differs from the lower horizon in the absence of calcium-poor amphiboles but does contain hornblende. In places, the hornblende replaces chlorite and cuts across foliation (Fig. 16d) and could be interpreted to be related to regional metamorphism but if so, the conversion of chlorite to hornblende was incomplete. Given that the hornblende is localized within the upper mineralized zone, it is probable that the hornblende was formed as a result of fluid flow through the altered zone of mineralization. The replacement of chlorite by epidote may have occurred during a later episode of synvolcanic hydrothermal activity related to rifting with resultant release of more hot fluids, or later due to hydrothermal alteration related to gold mineralization. Coarse-grained hornblende in BIF at the Herbert Prospect (Fig. 27b) may also have been formed as a result of metamorphism, although metasomatic replacement of carbonate by hot fluids is another possibility. The presence of hornblende in the 10 cm wide alteration zone around a late quartz–prehnite vein (Fig. 43) in rhyolite at the Dicksons (Silver Swan) Prospect and within a quartz veinlet at the Herbert Prospect (Fig. 25e) is

evidence that hornblende can be formed by hydrothermal fluids and, if the vein is related to post-peak metamorphic gold mineralization, hot fluids were active in the area for a prolonged period of time.

Talc is the most abundant alteration mineral proximal to mineralization in both the upper and lower mineralized horizons at Austin. Talc is also the most abundant proximal alteration mineral at Just Desserts (Hassan, 2014). Talc has also been reported in association with VMS mineralization at the Archean Mattagami Lake Mine in Canada (Roberts and Reardon, 1978; Costa et al., 1983); the Paleozoic Woodlawn, Breadalbane, Mount Bulga, and Googong lead–zinc deposits in New South Wales (McLeod and Stanton, 1984), and the Devonian–Triassic Chu Chua deposit in British Columbia, Canada (Aggarwal and Nesbitt, 1984). The talc at the Mattagami Lake Mine was interpreted by Roberts and Reardon (1978) to have formed by the transformation of chlorite to talc according to the reaction:



This reaction occurred as a consequence of the discharge of large fluxes of thermal waters through the volcanic pile over a period sufficient to remove almost all the aluminium from the rocks. However, Costa et al. (1983) found no evidence that talc replaced chlorite at the Mattagami Lake Mine and concluded that the talc at the Mattagami Lake Mine was precipitated from a dynamic sea-floor brine pool. Aggarwal and Nesbitt (1984) and McLeod and Stanton (1984) also considered the talc at the Chu Chua deposit was chemically precipitated from hydrothermal vents on the seafloor. McLeod and Stanton (1984) proposed a similar origin for the talc in the Paleozoic deposits of New South Wales. Hassan (2014) concluded that the talc in the iron formation at the Just Desserts deposit is consistent with its forming on the seafloor by hydrothermal vent activity, but there was also evidence that talc replaces chlorite in the hyaloclastites between the mineralized horizons that may have formed by sub-seafloor replacement of the underlying rocks by a reaction similar to that given by Roberts and Reardon (1978). Similarly at Austin, talc in BIF and high-grade zinc mineralization (Fig. 16a) is interpreted to have formed on the seafloor but sub-seafloor replacement is likely in the altered rock physically beneath the high-grade zinc zone where talc clearly replaces chlorite and, in places, calcium-poor amphiboles (Fig. 16b) indicative of prolonged hydrothermal activity.

Distal to mineralization at Austin, chlorite is the most abundant alteration mineral. Its composition ranges from magnesium rich to iron rich and probably reflects the composition of the host rocks as found for the chlorite at Golden Grove (Guilliamse, 2014) and Yuinmery (Hassan, 2014), although it could also reflect varying amounts of magnesium and iron metasomatism. At Tasman, iron-rich chlorite is the most abundant alteration mineral associated with mineralization. The HyLogger showed minor talc to also be present at the Tasman Prospect, and Duuring et al. (2016) reported talc in addition to chlorite in other deposits in the Quinns area.

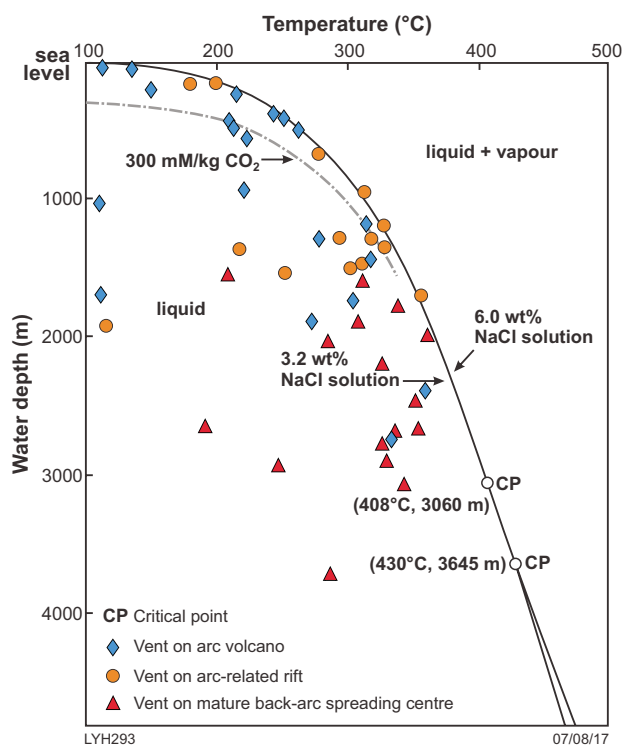


Figure 51. Maximum vent temperatures of modern seafloor hydrothermal systems in different volcanic and tectonic settings (after Monecke et al., 2014)

Coarse andalusite is a characteristic feature of the Quinns Mining Centre. Feldtmann (1921) interpreted the andalusite to be the product of contact metamorphism of sedimentary rocks. Vearncombe (2011) reported that the andalusite-bearing schist is aluminium rich and trace element geochemistry suggests a mafic to felsic volcanic precursor. Vearncombe (2011) indicated that the origin of this rock was uncertain but that it was not a Barrovian metamorphism of sediments and proposed instead that it was either metamorphosed Archean bauxite, or more likely, that it was a zone of intense hydrothermal fluxing in which mobile elements had been depleted. Duuring et al. (2016) mapped a 2 x 1 km zone of coarse-grained andalusite \pm kyanite \pm garnet schist in the area south of the Tasman Prospect which transgressed lithological boundaries including metasedimentary rocks, mafic rocks and felsic rocks (Fig. 53). Aluminium silicates have been reported in proximity to many VMS deposits and interpreted to be the result of metamorphism of advanced argillic alteration (Pan and Fleet, 1999; Galley et al., 2007). The andalusite \pm kyanite \pm garnet schist at Quinns envelops proximal chlorite \pm talc alteration with areas more distal to mineralization having a quartz – white mica assemblage. In order to form kyanite by regional metamorphism, the quartz–albite–epidote–almandine subfacies of greenschist facies would need to be reached.

Vearncombe (2011) logged sillimanite in the deep drillhole ATD101 at Austin and interpreted it to be volcanogenic in origin. This mineral was found to be anthophyllite in this study. However, all three polymorphs of aluminium



Figure 52. Core sample showing sulfide-rich breccia zone that may have been pathway for hydrothermal fluids

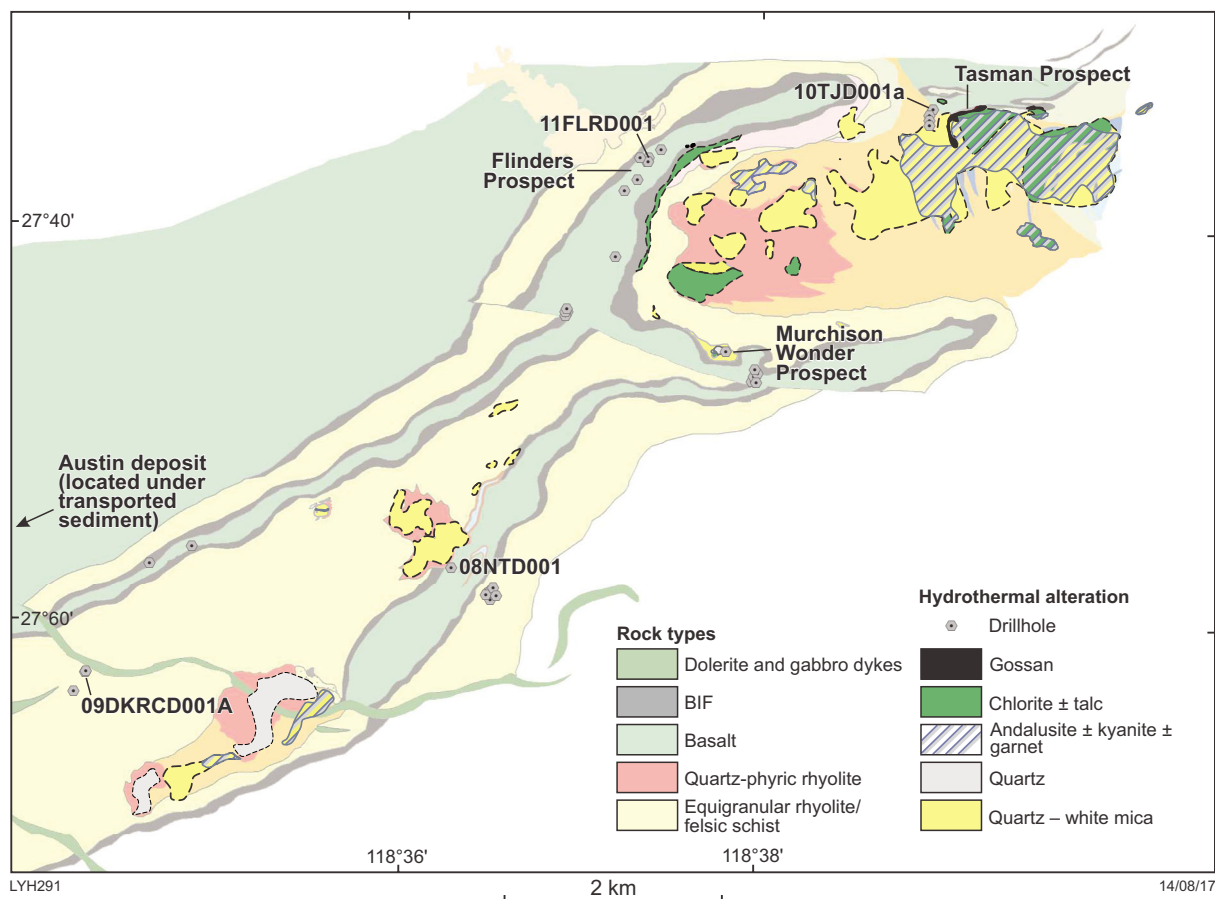


Figure 53. Zonation of hydrothermal alteration minerals in the Quinns area (after Duuring et al., 2016)

silicate occur in drillhole 09FKRCD001 from the Franklin Prospect about halfway between Austin and Quinns (Fig. 30a–d). All three polymorphs of aluminium silicate are also present at the Savant Lake and Marshall Lake in Canada (Pan and Fleet, 1999) and at Wheatley in the southwest of Western Australia (Hassan, 2017). Although it is possible for all three aluminium silicate polymorphs to coexist at the metamorphic triple point (the position of which is very uncertain but generally accepted as being at about 504°C and 3.75 kbar; Holdaway and Mukhopadhyay, 1993), it is unlikely that the three polymorphs at Austin are in equilibrium. The spotty nature of the andalusite could indicate that it formed by contact metamorphism by underlying intrusions. However, most of the andalusite in 09FKRCD001 appears to partially replace fine-grained white mica and chlorite interstitial to quartz, and is only locally developed in the vicinity of fractures (Fig. 30a). More coarsely grained andalusite also occurs locally in the vicinity of fractures. Kyanite appears to partially replace the andalusite interstitial to quartz (Fig. 30d) and also occurs as radiating crystal aggregates at the edge of veinlets (Fig. 30c). Sillimanite is quite rare and, where present, appears to replace andalusite and coexists with chlorite (Fig. 30b) in the vicinity of a fracture. Given that all three aluminium silicates in

09FKRCD001 are localized near fractures, it is probable that they were formed as a result of fluid flow through the rocks. In order to replace andalusite by sillimanite, the fluids would have had to be extremely hot or very locally under high pressure. Regardless of whether the aluminium silicates formed as a result of regional metamorphism or metasomatism by hot fluids, their presence in a wide variety of rocks at Quinns including felsic volcanic rocks is indicative of argillic or advanced argillic alteration.

The presence of a high concentration of spessartine as well as almandine in garnet from the Tasman Prospect is indicative of Mn metasomatism as well as the introduction of iron and aluminium. Spessartine is associated with some VMS deposits and can form from Mn-rich carbonate and clay or Mn-oxyhydroxides in exhalites (Slack, 2012).

A summary of the alteration minerals in the different prospects and their relative timing is given in Table 19. This highlights several phases of alteration district wide: alteration associated with deposition and diagenesis on the seafloor; synvolcanic alteration in the sub-seafloor by circulation of hot fluids; and alteration associated with fluid flow during synvolcanic rifting or during greenschist facies metamorphism.

Table 19. Summary of alteration minerals and relative timing at the different prospects in the Austin–Quinns area

<i>Austin</i>	<i>Robert</i>	<i>Herbert</i>	<i>Franklin</i>	<i>Dicksons (Silver Swan)</i>	<i>Quinns area (including Tasman)</i>
Deposition of sulfides around black smokers contemporaneously with talc, iron oxides, silica and phosphates in hot, deep brine pool on seafloor during period of volcanic quiescence. Anthophyllite formed in BIF during diagenesis	Deposition of exhalite and very minor sulfides in hot brine pool on seafloor during period of volcanic quiescence. Anthophyllite formed in exhalite during diagenesis	Deposition of BIF and minor sulfides on seafloor during periods of volcanic quiescence. Local rifting or explosive volcanism resulted in formation of BIF and chert breccia			Deposition of sulfides around black smokers contemporaneously with iron-rich chlorite, talc, iron oxides, silica and carbonate in hot, deep brine pool on seafloor during period of volcanic quiescence. Grunerite formed in main BIF horizon during diagenesis with gas bubbles later filled by chlorite
Circulation of hydrothermal fluids in sub-seafloor rocks resulted in widespread chloritic alteration; proximal to mineralization, chlorite replaced by talc due to leaching of aluminium. Chlorite and talc alteration distal to mineralization. Cummingtonite formed very locally beneath the lower mineralized horizon as a result of the passage of very hot fluids. With the passage of cooler fluids, the cummingtonite was partially replaced by anthophyllite and talc	Circulation of hot fluids in sub-seafloor rocks resulted in widespread chloritic alteration, most intense proximal to the exhalite. Distal chlorite and white mica alteration	Circulation of hot fluids in sub-seafloor rocks resulted in widespread chloritic alteration of felsic volcanics	Circulation of hot fluids in sub-seafloor rocks resulted in replacement of all feldspar if rock was originally a felsic lava or tuff by clay or white mica and chlorite. If protolith was a felsic lava, then primary biotite replaced by Phase x. If protolith was a tuff, then replacement of pumice by Phase x. Partial replacement of Phase x by chlorite and minor white mica	Circulation of hot fluids resulted in minor chloritic alteration of felsic volcanics	Circulation of hot fluids in sub-seafloor rocks resulted in widespread chloritic alteration; minor replacement of chlorite by talc proximal to mineralization. Farther from mineralization, zone of clay alteration. More distally, chlorite and white mica alteration
Overprinting of talc and chlorite alteration in mineralized horizon by Ca-amphiboles and minor allanite related to deformation caused by synvolcanic rifting or regional metamorphism. Some recrystallization and local remobilization of sulfides during deformation	Regional development of chlorite, albite and, in mafic rocks, epidote. Minor quartz–carbonate–prehnite veining	Replacement of iron-rich silicates or carbonate in BIF by hornblende, development of hornblende and epidote around quartz veinlets and formation of minor garnet during synvolcanic rifting, regional metamorphism or post-peak metamorphic hydrothermal alteration	Replacement of clay, white mica and chlorite by andalusite close to fluid pathways. During pulses of hotter fluid, partial replacement of andalusite by kyanite and growth of kyanite along edges of veins. Very localized replacement of andalusite by sillimanite, possibly due to localized increase in fluid pressure. Localized formation of magnesiochloritoid in cavities. Alteration of zircon to xenotime. Formation of gedrite, possibly by replacement of Phase x during deformation. Replacement of pyroxenes in gabbro by talc, chlorite, serpentine and amphiboles	Biotite, epidote, carbonate, hornblende or actinolite formed along localized shears; hornblende also formed in alteration halo around quartz veins. Minor gold mineralization associated with quartz–carbonate veining	Replacement of clay by andalusite and kyanite. Local development of garnet. Formation of auriferous quartz veins and lodes

Environment of formation

The presence of BIF is indicative of a subaqueous environment of deposition. Chemical sedimentary rocks or exhalites are spatially associated with many VMS deposits and are interpreted to have formed by precipitation of silica, iron, sulfides, and other minerals from hydrothermal vents during periods of volcanic quiescence (Sangster, 1972, 1978; Slack, 2012). The presence of slump folding in BIF is indicative of some tectonic disturbance soon after deposition while BIF was still in a plastic state. Syndepositional rifting would allow for flow of fluids heated by the underlying magma to reach the seafloor. At Austin, rare fragments of massive pyrite in a breccia (Fig. 15a) suggest that some pyrite was deposited as an exhalative layer and then broken up by later pyroclastic activity; or alternatively, that the pyrite was derived mechanically from a black smoker chimney and incorporated in the sediments on the seafloor. As discussed in the above section, in order for temperatures to be high enough for minerals such as anthophyllite and grunerite to form on the seafloor or during diagenesis, venting would need to have taken place in very deep, saline conditions.

Silver, bismuth and lead tellurides are present in the Austin ores and the mineralizing fluids were probably magmatic in origin as the presence of stützite is indicative of very high $f\text{Te}_2$ (Hassan and Roberts, 2017). That the Bi:Te (+Se) ratio of the tetradyte group minerals is <1 is indicative of oxidized assemblages, but the presence of both pyrrhotite and pyrite suggests that conditions either fluctuated between oxidized and reduced, or were close to the pyrrhotite–pyrite join (Hassan and Roberts, 2017).

The dolerite intrusions were interpreted by Vearncombe (2011) to be indicative of a deeper mafic subvolcanic sill or stock that acted as the heat engine to drive the sub-seafloor hydrothermal system from which the VMS mineralization was deposited. The basalt of the Meekatharra Formation overlying the rhyolite is also evidence of a long-lived magma chamber that would act as a heat source.

On the basis of trace element geochemistry carried out by the late Robert Kerrich at Saskatchewan University, Canada for the Silver Swan Group, there are two types of mafic rock present: a low-Ti primitive, tholeiitic arc basalt (intrusive dolerite) and an evolved high-Ti calc-alkaline magma; these constrain the geodynamic environment to a rifted arc, most likely a continental back-arc. The felsic rocks define a calc-alkaline, or medium- to high-K series, and were interpreted to have been generated by shallow melting of basaltic crust in an oceanic rift environment (Vearncombe, 2011). Although Van Kranendonk et al. (2013) interpreted the rocks of the Polelle Group to be plume related, Wyman and Kerrich (2012) identified boninite in a sample from the Polelle Group and concluded that its presence provided clear evidence of subduction tectonics during evolution of the Youanmi Terrane. Basalt and andesite hosting the Just Desserts deposit at Yunnan, which is possibly of similar age, have trace element geochemistry consistent with an arc-rift setting (Hassan, 2014).

Exploration vectors

On a regional scale, rocks indicative of formation in a rifted arc or other setting conducive to the formation of VMS deposits are necessary. On a more local scale, the presence of BIF indicative of a period of volcanic quiescence and evidence of widespread alteration are important. At Austin, talc and anthophyllite alteration are closely associated with mineralization but it is necessary to distinguish talc associated with mineralization from that associated with altered gabbro. In addition to the presence of anomalous base metals, the presence of bismuth and silver tellurides in the mineralization suggests that Bi, Te and Ag in gossans or surface samples would also be good pathfinders. Duuring et al. (2016) found that Cu, Zn, Ag, Au, Bi, Fe_2O_3 , In, Mg, Mo, S, Se and Te were all enriched in rhyolite proximal to mineralization. Positive Eu anomalies also distinguish mineralized BIF in the Quinns area from nonmineralized BIF (Duuring et al., 2016).

Conclusions

Volcanogenic massive sulfide prospects at Quinns (including Tasman, Quinns Gossan, Flinders and Murchison Wonder) are associated with BIF close to the contact between basalt and rhyolite or schist of uncertain protolith; whereas at Austin, the mineralization is within a predominately rhyolitic succession. The lowermost zinc-rich mineralized horizon intersected in 09ATD019 and 09ATD015 and also the mineralized horizon intersected by ATD101 at Austin are clearly associated with BIF and probably formed on the seafloor during a period of volcanic quiescence. A thin basalt horizon is associated with mineralization in ATD101, and trace element geochemistry also suggests that some of the highly altered schist associated with the lower mineralized horizon may be basalt. The upper copper-rich mineralized horizon in 09ATD019 and 09ATD015 has no clear association with BIF although the schist is possibly after silicate-facies BIF.

Talc is the main alteration mineral proximal to mineralization in both the upper and lower mineralized horizons at Austin and is indicative of intense magnesium metasomatism. The talc is interpreted to have formed both directly on the seafloor as a result of hydrothermal venting and in the subsurface as a result of replacement of earlier formed chlorite and removal of aluminium by moderately hot fluids. Local development of anthophyllite and cumingtonite beneath the main zinc-rich horizon is interpreted to be the result of metasomatism by passage of extremely hot fluids along fluid pathways; as the fluids along the pathways cooled, these minerals were partially replaced by talc. Calcium-rich amphiboles (hornblende and actinolite) overprint early alteration minerals in the mineralized horizons at Austin and may be related to fluid flow during later rifting or as a result of greenschist facies metamorphism. Chlorite and white micas are the main alteration minerals distal to mineralization at Austin.

At Quinns, iron-rich chlorite is the main alteration mineral associated with mineralization but some talc is also present indicating both Fe and Mg metasomatism. The presence

of aluminium silicates more distal to mineralization at Quinns is probably indicative of a zone of argillic or advanced argillic alteration. Unlike the talc-rich alteration at Austin where aluminium has been removed, aluminium has been concentrated in this zone. All three aluminium silicate polymorphs are present at the Franklin Prospect but are not considered to be in equilibrium or to be indicative of amphibolite-grade metamorphism as they show replacement textures and are associated with chlorite. Formation of andalusite by contact metamorphism or greenschist facies metamorphism is possible but the localization of the aluminium silicates adjacent to fractures at the Franklin Prospect suggests a metasomatic origin. Beyond the zone of aluminium silicates, chlorite and white mica are the main alteration minerals at Quinns, similar to the distal alteration mineral assemblage at Austin.

The base metal mineralization and associated alteration is interpreted to have formed during periods of volcanic quiescence in a very deep brine pool in a rifted arc environment with hot fluids driven by heat from underlying magma. Rifting and hot fluid flow may have occurred over a long period of time and resulted in overprinting of early alteration assemblages by Ca-amphiboles and development of gold-bearing lodes and quartz veins.

Acknowledgements

The former Silver Swan Group is thanked for loaning core from the Austin and Roberts Prospects for HyLogger scanning, allowing sampling of the core for petrography and providing assay data. Michael Verrall from the Earth Science and Resource Engineering division of CSIRO in Kensington is thanked for assisting with SEM analyses, and Malcolm Roberts from the Centre for Microscopy, Characterisation and Analysis, The University of Western Australia is thanked for assisting with electron microprobe analyses.

References

- Aggarwal, PK and Nesbitt, BE 1984, Geology and geochemistry of the Chu Chua massive sulfide deposit, British Columbia: *Economic Geology*, v. 79, p. 815–825.
- Bishop, SR 1991, Annual report to 30/12/1990 for M51/3435; 87–88, 195–196, P51/1511–1512, Quinns SG50-16, Sandstone, Western Australia; CRA Exploration Pty Ltd: Geological Survey of Western Australia, Statutory mineral exploration report, A33750 (Public), 195p.
- Bishop, SR 1992b, Annual report for period ended 15 September 1991 for Peregrine Well E51/205, P51/1267 and Cullculli E51/297, Sandstone SG-50-16, Cue SG-50-15, Western Australia; CRA Exploration Pty Ltd: Geological Survey of Western Australia, Statutory mineral exploration report, A35535 (Public), 229p.
- Bishop, SR 1992a, Final report for M51/34-35, 87-88, 195-196, P51/1511-1512, Quinns, SG-50-16 Sandstone, Western Australia; CRA Exploration Pty Ltd: Geological Survey of Western Australia, Statutory mineral exploration report, A35407 (Public), 188p.
- Costa, UR, Barnett, RL and Kerrich, R 1983, The Mattami Lake Mine Archean Zn-Cu sulfide deposit, Quebec: hydrothermal coprecipitation of talc and sulfides in a sea-floor brine pool - evidence from geochemistry, $^{18}\text{O}/^{16}\text{O}$, and mineral chemistry: *Economic Geology*, v. 78, p. 1144–1203.
- Duuring, P, Hassan, L, Zelic, M and Gessner, K 2016, Geochemical and spectral footprint of metamorphosed and deformed VMS-style mineralization in the Quinns District, Yilgarn Craton, Western Australia: *Economic Geology*, v. 111, no. 6, p. 1411–1438.
- Feldtmann, FR 1921, The mining centres of Quinn's and Jasper Hill, Murchison Goldfield: Geological Survey of Western Australia, Bulletin 80, 82p.
- Evans, BW and Ghiorso, MS 1995, Thermodynamics and petrology of cummingtonite: *American Mineralogist*, v. 80, p. 649–663.
- Galley, AG, Hannington, MD and Jonasson, IR 2007, Volcanogenic massive sulphide deposits, in *A synthesis of major deposit-types, district metallogeny, the evolution of geological provinces, and exploration methods* edited by WD Goodfellow: Geological Association of Canada, Mineral Deposits Division, Special Publication 5, p. 141–161.
- Geological Survey of Western Australia 2017, Murchison, 2017: Geological Information Series.
- Gibson, HL and Galley, AG 2007, Volcanogenic massive sulphide deposits of the Archean, Noranda district, Quebec, in *Mineral deposits of Canada: a synthesis of major deposit-types, district metallogeny, the evolution of geological provinces, and exploration methods* edited by WD Goodfellow: Geological Association of Canada, Special Publication 5, p. 533–552.
- Gibson, HL and Kerr, DJ 1993, Giant volcanic-associated massive sulfide deposits: with emphasis on Archean examples, in *Giant ore deposits* edited by BH Whiting, CJ Hodgson and R Mason: Society of Economic Geologists, Special publication 2, p. 319–348.
- Guilliamse, J 2014, Assessing the potential for volcanic-associated massive sulfide mineralization at Weld Range, using Golden Grove for comparison: Geological Survey of Western Australia, Report 141, 61p.
- Hancock, EA, Green, AA, Huntington, JF, Schodlok, MC and Whitbourn, LB 2013, HyLogger-3: Implications of adding thermal-infrared sensing: Geological Survey of Western Australia, Record 2013/3, 24p.
- Hancock, EA and Huntington, JF 2010, The GSWA NVCL HyLogger: rapid mineralogical analysis for characterizing mineral and petroleum core: Geological Survey of Western Australia, Record 2010/17, 21p.
- Hassan, LY 2014, The Yuinmery volcanogenic massive sulfide prospects: mineralization, metasomatism and geology: Geological Survey of Western Australia, Report 131, 65p.
- Hassan, LY 2017, Metamorphosed VMS mineralization at Wheatley, southwest Western Australia: Geological Survey of Western Australia, Record 2017/9, 39p.
- Hassan, LY and Roberts, MP 2017, Tellurides associated with volcanogenic massive sulfide (VMS) mineralization at Yuinmery and Austin, Western Australia: *Ore Geology Reviews*, v. 80, p. 352–362.
- Herrmann, W, Blake, M, Doyle, M, Huston, D, Kamprad, J, Merry, N and Pontual, S 2001, Short wavelength infrared (SWIR) spectral analysis of hydrothermal alteration zones associated with base metal sulfide deposits at Rosebery and Western Tharsis, Tasmania, and Highway-Reward, Queensland: *Economic Geology*, v. 96, no. 5, p. 939–955.
- Holdaway, MJ and Mukhopadhyay, B 1993, A reevaluation of the stability relations of andalusite: Thermochemical data and phase diagram for the aluminum silicates: *American Mineralogist*, v. 78, p. 298–315.
- Maniwi, JG and Fitton, A 1987, Annual report for 1987 on ML 51/34-35, 87-88 and E51/51, Quinns, Sandstone SG-50-16, Western Australia; CRA Exploration Pty Ltd: Geological Survey of Western Australia, Statutory mineral exploration report, A23723, 35p.

- McLeod, RL, Gabell, AR, Green, AA and Gardavski, V 1987, Chlorite infrared spectral data as proximity indicators of volcanogenic massive sulphide mineralization, *in* Proceedings: Pacific Rim Congress 87, Gold Coast, Queensland, 26 August 1987, p. 321–324.
- McLeod, RL and Stanton, RL 1984, Phyllosilicates and associated minerals in some Paleozoic stratiform sulfide deposits of Southeastern Australia: *Economic Geology*, v. 79, p. 1–22.
- Monecke, T, Petersen, S and Hannington, MD 2014, Constraints on water depth of massive sulfide formation: evidence from modern seafloor hydrothermal systems in arc-related settings: *Economic Geology*, v. 109, no. 5, p. 2079–2101.
- Morin-Ka, S 2012, Hyperspectral characterization of rare earth minerals: Geological Survey of Western Australia, Record 2012/12, 50p.
- Newmont Pty Ltd 1977, Annual report to Mines Department: Quinns Prospect; Newmont Pty Ltd: Geological Survey of Western Australia, Statutory mineral exploration report, 7167 (Public), 271p.
- Newmont Pty Ltd 1978, Final report on Quinns Prospect, WA; Newmont Pty Ltd: Geological Survey of Western Australia, Statutory mineral exploration report, A7555 (Public), 308p.
- Pontual, S 2008, GMEX spectral analysis guides for mineral exploration (3rd edition): AusSpec International Ltd, 10 vols.
- Roberts, RG and Reardon, EJ 1978, Alteration and ore-forming processes at Mattagami Lake Mine, Quebec: *Canadian Journal of Earth Sciences*, v. 15, p. 1–21.
- Sangster, DF 1972, Precambrian volcanogenic massive sulphide deposits in Canada: a review: Department of Energy and Resources (Ottawa), 44p.
- Sangster, DF 1978, Exhalites associated with Archaean volcanogenic massive sulfide deposits, *in* Archaean cherty metasediments: their sedimentology, micropalaeontology, biogeochemistry and significance to mineralization *edited by* JE Glover and DI Groves: Extension Service, The University of Western Australia, Perth Publication No. 2, p. 70–75.
- Silver Swan Group Limited 2008, New copper–zinc discovery in Western Australia: Report to Australian Securities Exchange, 30 July 2008, 4p.
- Silver Swan Group Limited 2009, June Quarterly Activities Report: Report to Australian Securities Exchange, 31 July 2009, 4p.
- Silver Swan Group Limited 2010a, Austin: maiden resource statement: Report to Australian Securities Exchange, 6 April 2010, 6p.
- Silver Swan Group Limited 2010b, Further sulphides encountered in Austin drilling: Report to Australian Securities Exchange, 30 September 2010, 3p.
- Silver Swan Group Limited 2011, Flinders VMS prospect, Quinns project — drilling update: Report to Australian Securities Exchange, 15 December 2011, 6p.
- Slack, JF 2012, Exhalites, *in* Volcanic massive sulfide occurrence model *edited by* WCP Shanks III and R Thurston: United States Geological Survey, Reston, Virginia, USA, Scientific Investigations Report 2010-5070-C, p. 159–163.
- Spear, FS 1993, Metamorphic phase equilibria and pressure–temperature–time paths: Mineralogical Society of America, Monograph, 799p.
- Tingey, RJ (compiler) 1985, Sandstone, Western Australia: Geological Survey of Western Australia, 1:250 000 Geological Series Explanatory Notes, 37p.
- Van Kranendonk, MJ 2011, Nowthanna, WA Sheet 2643: Geological Survey of Western Australia, 1:100 000 Geological Series.
- Van Kranendonk, MJ, Ivanic, TJ, Wingate, MTD, Kirkland, CL and Wyche, S 2013, Long-lived, autochthonous development of the Archaean Murchison Domain, and implications for Yilgarn Craton tectonics: *Precambrian Research*, v. 229, p. 49–92.
- Vearncombe, JR 2011, Final report on the completion of the Austin Deeps drill hole 10ATD101 in the Quinns Project area; Silver Swan Group: Geological Survey of Western Australia, Statutory mineral exploration report, 90527, 37p.
- Vearncombe, S 2010, Quinns Project — Geodynamic setting and mineralization: Technical presentation to Mining & Exploration Group of WA (MEGWA) April 2010: viewed 18 June 2015, <www.asx.com.au/asxpdf/20100422/pdf/31px7zthwx30yv.pdf>.
- Wyman, DA and Kerrich, R 2012, Geochemical and isotopic characteristics of Youanmi terrane volcanism: the role of mantle plumes and subduction tectonics in the western Yilgarn Craton: *Australian Journal of Earth Sciences*, v. 59, no. 5 (Archean evolution — Yilgarn Craton), p. 671–694, doi:10.1080/08120099.2012.702684.
- Zelic, M, Vearncombe, J, Vearncombe, S and Potma, W 2012, Structural geological mapping of the Quinns area, Murchison Domain: a predictive tool for exploration of folded VMS-mineral deposits, *in* Extended abstracts *edited by* J Vearncombe: Australian Institute of Geoscientists and Geoscientists Symposium; Structural geology and resources – 2012, Kalgoorlie, Western Australia, 26 September 2012; Bulletin 56, p. 187–190.

This Record is published in digital format (PDF) and is available as a free download from the DMIRS website at
<www.dmp.wa.gov.au/GSWApublications>.

Further details of geological products produced by the Geological Survey of Western Australia can be obtained by contacting:

Information Centre
Department of Mines, Industry Regulation and Safety
100 Plain Street
EAST PERTH WESTERN AUSTRALIA 6004
Phone: +61 8 9222 3459 Fax: +61 8 9222 3444
www.dmp.wa.gov.au/GSWApublications

ALTERATION ASSOCIATED WITH THE AUSTIN-QUINNS
VMS PROSPECTS, NORTHERN YILGARN CRATON

